**Title**
Modeling and Design of a Tensegrity-based Morphing Wing



**Author**
Pham, Nguyen Kim

**Publication Date**
2021

Peer reviewed|Thesis/dissertation

UNIVERSITY OF CALIFORNIA,
IRVINE

# Modeling and Design of a Tensegrity-based Morphing Wing

THESIS

submitted in partial satisfaction of the requirements
for the degree of

MASTER OF SCIENCE

in Mechanical and Aerospace Engineering

by

Nguyen Kim Pham

Thesis Committee:
Assistant Professor Edwin A. Peraza Hernandez, Chair
Assistant Professor Jacqueline Thomas
Professor Mark E. Walter

2021

# DEDICATION

To my family, especially my parents Huy Quang Pham and Minh Thi Nguyen for their unconditional love and support throughout my journey.

To my godfather and godmother, my aunt and late uncle for their support since the day I stepped foot onto the U.S.A in pursuit of my dreams and education.

# TABLE OF CONTENTS

# LIST OF FIGURES

Page

# LIST OF TABLES

Page

# ACKNOWLEDGMENTS

"How priceless is your unfailing love, O God! People take refuge in the shadow of your wings." (Psalm 36:7-8 New International Version)

I would like to begin by thanking God for all the blessings and the faith He has given me, for answering my prayers, and for His grace. Throughout my journey in the United States as an immigrant, He has guided and comforted me at every step of the way. All of my achievements thus far would not have been possible without my prayers and faith in Him.

I want to thank my parents, both of whom have made tremendous sacrifices to allow me to pursue my education and ambitions in the United States. Although I left home at a relatively young age, their constant moral and emotional support have strengthened and encouraged me to overcome every challenge. Finally, I thank them for their unconditional love through both my successes and failures. I also owe gratitude to my godparents, my aunt, and uncle, who had given me a home and provided guidance and care when I first arrived in the United States. I dedicate this work to my parents and to them.

I am grateful to Dr. Edwin A Peraza Hernandez, my adviser and committee chair, who have given me the opportunity to join his research group and work on this novel concept of a morphing wing, for the countless hours of discussion and review of my research papers, and for the unrelenting optimism and encouragement. I learned many critical engineering and communicating skills during my time working with Dr. Hernandez and I felt honored to work under his counsel and support. I also want to thank his undergraduate senior design team who had built and provided the tensegrity wing prototype that I used in my work. Lastly, I sincerely appreciate Dr. Navid Nakhjiri from Cal Poly Pomona, my first research adviser during my undergraduate years. He had taught me the techniques of numerical methods and simulations and inspired me to pursue research and attend UCI to obtain a graduate degree.

I would like to extend my gratitude to Dr. Jacqueline Thomas and Dr. Mark E. Walter for agreeing to be my committee members. Although I have not had the chance to attend one of their classes, their active participation, suggestions, and insights during my thesis presentation have allowed me to greatly improve it. Their insightful comments have allowed me to approach problems from a researcher perspective. I also want to thank Dr. Anargyros A. Karakalas, who had provided the shape memory alloy user-material subroutine for Abaqus (`UMAT`), which allowed me to evaluate one of the options to activate the morphing mechanism.

I also want to express my appreciation to the professors, teachers, staff members, classmates and colleagues at my high school in Vietnam, Seattle Central College, California State Polytechnic University of Pomona, and the University of California, Irvine. Furthermore, I want to extend my gratitude to members of the Morphing Structures Group at UCI, specifically, Yudong, Weilin, and Shyam for helping me with the research and allowing me to use some of their work in writing this thesis. It has been my honor to have attended these institutions. Everyone that I have met at these institutions have encouraged and assisted me in my educational and professional journey.

To my extended family members, my incredible girlfriend, my best friends, and roommates, thank you all for the remarkable experiences and supports I have been blessed with. I want to thank everyone with all my heart for being there through the countless hours of hard work and struggles, and for contributing to my personal and professional development.

Finally, I want to thank the American Society of Mechanical Engineers and the American Institute of Aeronautics and Astronautics for giving me permission to incorporate my previously published works into this thesis.

# VITA

## Nguyen Kim Pham

### EDUCATION

**Master of Science in Mechanical and Aerospace Engineering** **2021**
University of California, Irvine *Irvine, California*

**Bachelor of Science in Aerospace Engineering** **2018**
California State Polytechnic University, Pomona *Pomona, California*

**Associate of Science in Engineering** **2014**
Seattle Central College *Seattle, Washington*

### RESEARCH EXPERIENCE

**Graduate Researcher** **2020–2021**
Morphing Structures Group, University of California, Irvine *Irvine, California*

**Undergraduate Researcher** **2017–2018**
California State Polytechnic University, Pomona *Pomona, California*

### PROFESSIONAL EXPERIENCE

**Manufacturing Engineer** **2018–2019**
Precise Aerospace Manufacturing *Corona, California*

## REFEREED JOURNAL PUBLICATIONS

**Modeling and design exploration of a tensegrity-based twisting wing** **2021**

Journal of Mechanisms and Robotics. https://doi.org/10.1115/1.4050149

Nguyen K. Pham and Edwin A. Peraza Hernandez.

## CONFERENCE PUBLICATIONS

**Design exploration of a tensegrity twisting wing enabled by shape memory alloy wire actuation** **Mar 2021**

Proceedings of SPIE Smart Structures/NDE 2021, 11588-220, virtual conference.

Weilin Guan, Nguyen K. Pham, and Edwin A. Peraza Hernandez

**Modeling and design exploration of a morphing wing enabled by a twisting tensegrity mechanism** **Jan 2021**

Proceedings of the 2021 AIAA SciTech Forum and Exposition, AIAA 2021-0099, virtual conference. https://doi.org/10.2514/6.2021-0099

Nguyen K. Pham and Edwin A. Peraza Hernandez

**Design exploration of a tensegrity-based twisting wing** **Aug 2020**

Proceedings of the ASME 2020 International Design Engineering Technical Conference & Computers and Information in Engineering Conference (IDETC/CIE 2020), DETC2020-22656, virtual conference. https://doi.org/10.1115/DETC2020-22656

Nguyen K. Pham and Edwin A. Peraza Hernandez

## AWARDS AND AFFILIATIONS

Sigma Gamma Tau - National Aerospace Engineering Honor Society
American Institute of Aeronautics and Astronautics (AIAA)
American Society of Mechanical Engineers (ASME)
Finalist for SPIE Smart Structures/NDE 2021 Paper Competition

# ABSTRACT OF THE THESIS

Modeling and Design of a Tensegrity-based Morphing Wing

By

Nguyen Kim Pham

Master of Science in Mechanical and Aerospace Engineering

University of California, Irvine, 2021

Assistant Professor Edwin A. Peraza Hernandez, Chair

This thesis presents a modeling and design exploration study of a novel twisting wing whose motion is enabled by a tensegrity mechanism. First, the aerodynamic characteristics of the twisting wing, which does not require control surfaces to modulate its shape, are compared with those of a conventional wing having a control surface. It is shown via computational fluid dynamics analyses that the twisting wing displays higher lift-to-drag ratio than the conventional wing and hence the twisting wing is more aerodynamically efficient. Subsequently, the torsional tensegrity mechanism, composed of multiple tensegrity cylindrical cells forming a column along the wingspan, is described. A finite element model of the wing incorporating this mechanism is developed. Using the model, a full factorial design of experiments study of the influence of the topological parameters of the torsional tensegrity mechanism on the twist angle, mass, and stress in the different components of the wing is performed. A wingspan of 142.24 cm and a chord length of 25.31 cm are assumed, corresponding to those of the Carl Goldberg Falcon 56 Mk II R/C unmanned aerial vehicle. For a wing of such dimensions, the maximum achievable twist angle from root to tip per unit mass without any component exceeding their allowable stress is 5.93°/kg and delivered 13.5° of twisting without violating any of the material failure stresses. This torsional deformation is sufficiently large to allow for effective modulation of the aerodynamic characteristics of the wing. The torsional tensegrity mechanism for this design consists of eight cylindrical cells and four sets

of actuator wires along the circumference of each cell. Subsequently, a design of experiments study performed using the orthogonal array (*a.k.a.* Taguchi) method is conducted to evaluate the effects of varying design parameters such as the thicknesses of the skin and ribs, the wire diameters, number of cells and wire sets, spar diameter, and material types. The most favorable design with a maximum twist angle to mass ratio of 10.85°/kg is presented and delivered up to 19.5° of twisting without violating any of the material failure stresses. Finally, befitting for the actuation of the tensegrity mechanism due to their wire form, shape memory alloy (SMA) wire actuators are explored for the reconfiguration of the wing shape through thermally driven material actuation. The combination of lightweight and compact tensegrity mechanism and SMA wire actuators eliminate the need for bulky components, such as hydraulic and electric actuators, to enhance the flight performance. The torsional morphing capability enabled by SMA actuation is demonstrated experimentally through a tensegrity twisting wing prototype integrated with commercially available SMA wire actuators. An additional orthogonal array design of experiments study is performed on the wing model with incorporated SMA wire actuators, where results analogous to those obtained from artificial strains in the aforementioned studies are obtained. The most favorable design of this DOE delivered a substantial 15.85° total twist angle without any material failure and had a mass of 2.02 kg. The obtained twist angle was comparable to the twist angle observed from the testing of the tensegrity twisting wing prototype with integrated SMA wire actuators.

# Chapter 1

# Introduction

[1]This chapter provides an introduction and literature review of the topics and concepts presented in the subsequent chapters of this thesis. A review of the motivation and on-going research in the field of morphing aircraft structures is presented in Section 1.1. Section 1.2 provides an overview of tensegrity structural designs and their potential in engineering applications. Finally, Section 1.3 details the contributions of this thesis and lays out the structure of the remainder of the paper.

## 1.1 Morphing Wing Motivation and Examples

With the rapidly growing demand for long-haul air vehicles, more efficient aircraft designs are needed. Future aircraft designs need to provide satisfactory fuel economy and payload capacity. Reducing aerodynamic drag is often a major focus in the quest for improving aircraft efficiency. Control surfaces such as ailerons, rudders, and elevators introduce dis-

[1]Portions of this section are reprinted or adapted from [Nguyen K. Pham and Edwin A. Peraza Hernandez, 2021, "Modeling and design exploration of a tensegrity-based twisting wing," Journal of Mechanisms and Robotics. https://doi.org/10.1115/1.4050149]. Figures and texts are reprinted by permission of the American Society of Mechanical Engineers.

continuities in the shape of the wings, which typically lead to an increase in drag and thus are a significant source of inefficiency [66]. Ongoing research has proposed solutions to replace control surfaces while maintaining maneuverability. For example, researchers recently conducted a successful flight test of the MAGMA Unmanned Aerial Vehicle (UAV), which employed supercritical circulation and fluidic thrust vectoring principles to provide efficient flight control [71].

An alternative approach to replacing conventional control surfaces in wings is to morph the wing shape during flight to adapt it to various flight conditions and provide control while maintaining aerodynamic efficiency. An example is the FlexFoil™ system, which is a wing design that uses a compliant structure and actuators to change the local angle of attack of the leading and trailing edge of the wing [32]. A similar system to the FlexFoil, named "twisterons," was designed by Phillips, Alley, and Goodrich and demonstrated the ability to provide roll control, high-lift, and minimum induced drag [49]. In another work, an upper skin morphing design that uses electrical actuators, designed by Gabor, Koreanschi, and Botez, demonstrated up to 26.73% reduction in the drag coefficient of the ATR 42 airfoil [18]. Morphing techniques have also been applied to other smooth bodies beyond wings such as in the case of wind turbine blades. In Ref. [4], it was shown that morphing blades have higher efficiency than rigid blades in applications of wave and wind energy conversion. Furthermore, [69] demonstrated through modeling and simulations that energy production of a wind turbine having morphing blades is 24.5% to 69.7% higher than that of a wind turbine having fixed pitch blades. Robust multi-objective optimization of these morphing blades for wind turbines using a post-optimality sensitivity analysis technique was presented in [70].

Molinari, Arrieta, and Ermanni presented a design framework for three-dimensional wings that simultaneously optimized the wing external shape, internal passive structure, and embedded smart material actuators [38]. Such a framework was applied to a morphing wing with embedded dieletric elastomer actuators. On the supersonic flight regime, Hodson *et al.* [26] and Beilefeldt *et al.* [5] devised design optimization approaches for morphing wings based on bio-inspired evolutionary design principles. The aforementioned efforts highlight that designing a morphing wing is an interdisciplinary challenge since the aerodynamic performance, stability, and structural integrity of the wing are closely interconnected [67].

## 1.2 Introduction to Tensegrity Structures

The mass of wing morphing systems typically outweighs the efficiency advantages they bring to aircraft [58]. Current morphing wing designs that incorporate SMA wires or springs often require complex mechanisms to enable wing morphing. The implementation of tensegrity-based mechanism presents an alternative approach to designing lightweight wing morphing systems. The term tensegrity was first coined by Buckminister Fuller by integrating the words *tension* and *integrity* [62]. Tensegrity is a term given to a pre-stressable structure having a set of bodies (rigid bodies, struts, etc.) that are structurally stabilized in space by a network of tensile members. The pre-stress or rest length of the tensile members in tensegrity structures can be controlled to manipulate their shape and stiffness. This feature has allowed tensegrity structures to be applied in various general-use manipulators [6, 17]. Tensegrity structures have also demonstrated attractive engineering characteristics such as having load-bearing properties [20, 21, 61], tailorable thermal expansion [3, 60], and energy absorption capabilities [19, 44, 53] using minimum mass. Moreover, tensegrity systems do not compromise the structural integrity of the wing and other aircraft structures [67]. Another attractive property of tensegrity structure lies in the fact that they are highly scalable since it is the geometric arrangement that dictates the macroscale properties rather than material limitations [13]. Rieffel *et al.* developed an evolutionary algorithm that can create larger-scale tensegrity structures [52]. In Ref. [39], Moored and Bart-Smith introduced "clustered actuation," an highly scalable actuation strategy that can be applied to facilitate complex shape changes in large scale structures while reducing the number of needed actuators. Due to all the stated properties, tensegrity structures are considered as potential candidates for morphing wing designs [43].

There are different approaches in designing tensegrity-based morphing wings documented in the literature. In 2007, Moored and Bart-Smith presented a morphing wing design for submarine vehicles that demonstrated the feasibility and potential for development of tensegrity-based morphing structures that travel through liquid media [40]. As for aeronautical applications, an algorithm based on an output regulator controller that transforms a two-dimensional airfoil from its initial configuration to another desired final shape by properly actuating the tensile members of an inner tensegrity structure was presented in [25]. The algorithm was able to approximate several National Advisory Committee for Aeronautics (NACA) airfoils–with both symmetric and asymmetric profiles–using controlled tensegrity structures. Another representative example was presented by Mills and colleagues who published a paper where they demonstrated that a tensegrity-based wing with similar strength characteristics to those of a conventional wing had a significantly lower structural weight [37].

## 1.3 Tensegrity-based Morphing Wing Concept

This paper presents a modeling and design exploration study of a novel control surface-free twisting wing enabled by an internal tensegrity mechanism. The torsional tensegrity mechanism is inspired by the twisting column presented in [62], which was applied to a cylindrical tower. Such a tower worked by sending electrical current through a network of shape memory alloy wires, which were contracted due to the increase in their temperature and rotated the top of the tower by 40° relative to the bottom without changing the tower height. This twisting column concept provides the basis of a torsional tensegrity mechanism that is devised in this work to create a twisting wing. This design concept works in a similar fashion to that of a flaperon in the sense that twisting wing can provide a singular solution to replace both flaps and ailerons. The twisting motion of the wing provides high lift and pitch control when they are both twisted in the same direction, thus, eliminating the need for a discreet flap system. Alternatively, when only one side of the wing is twisted, this mechanism can provide roll control in place of ailerons. Undergraduate students from the Mechanical and Aerospace Engineering Department of the University of California, Irvine recently built an early prototype of this concept which is depicted in Fig. 1.1 [65].

The advantages of using torsional deformation in wings to enable high aerodynamic efficiency, among other favorable properties, are discussed in Chapter 2. Different attractive approaches to enable torsional deformation in wings have been investigated including using shape memory alloy torque tubes [57] and cellular structures [28]. Both approaches allow for low structural mass; however, shape memory alloy torque tubes have very high costs and may have a slow actuation response since they are thermally activated while cellular structures have a high level of structural complexity and require a large number of components. The proposed torsional tensegrity mechanism based on a cylindrical column provides the advantages of being formed by low-cost materials, can be controlled via mechanical motors, and does not introduce large complexity on the wing design. The tensegrity column is chosen over other tensegrity topologies that enable torsion such as tensegrity prisms [11] because the column can provide high bending stiffness since it can be attached to a central solid bar as shown in Fig. 1.1 and it can undergo torsional deformation without changing its axial or radial dimensions.

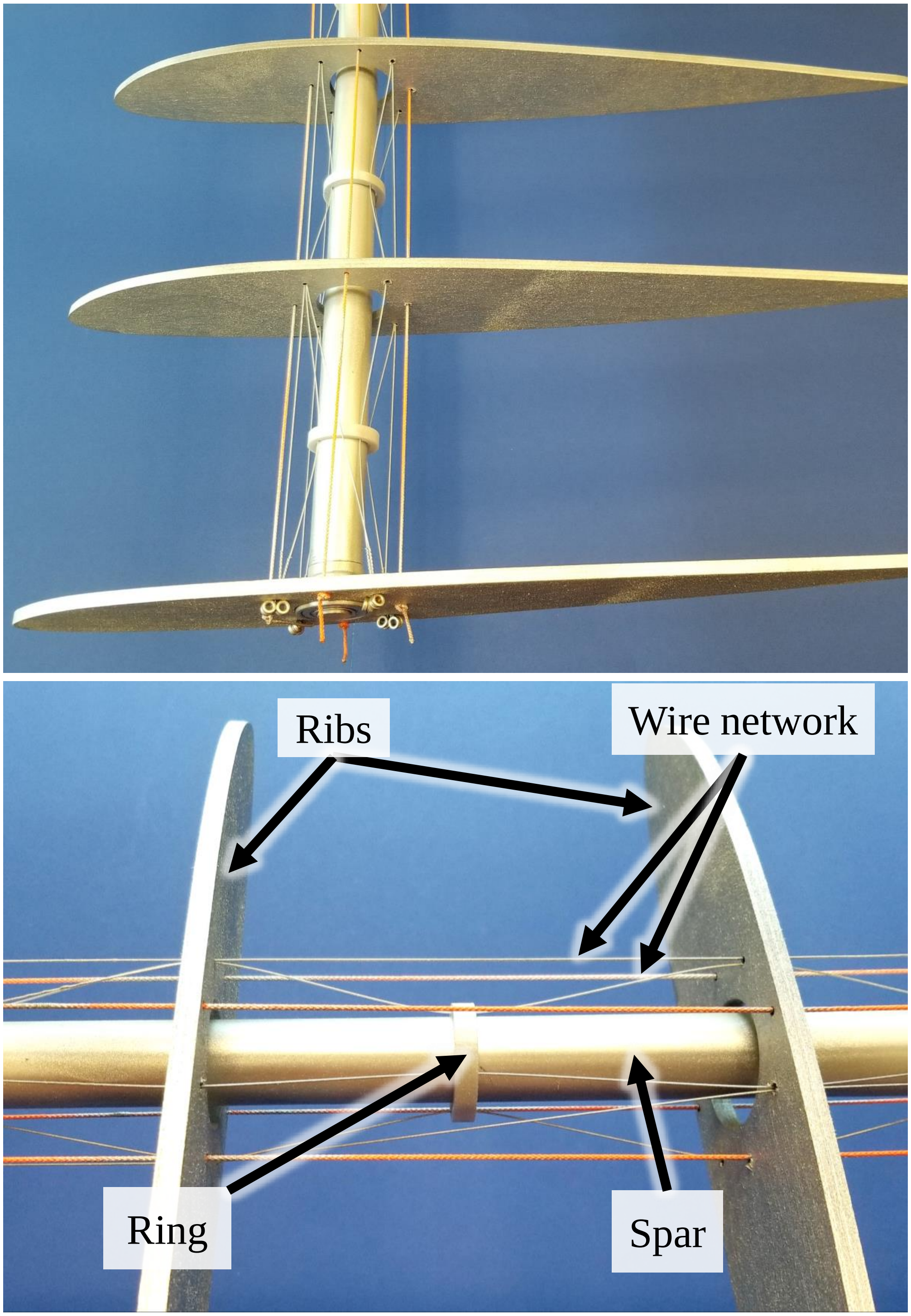


Figure 1.1: Tensegrity wing early prototype fabricated by a senior design team from the Department of Mechanical and Aerospace Engineering at the University of California, Irvine [65]. Adapted from [46].

## 1.4 Incorporation of Shape Memory Alloys Into Tensegrity Wing Morphing

[2]Due to the constrained space within the wing, bulky electric and hydraulic powered actuation systems are unattractive because they require complicated engineering effort to be accommodated into the wing structure and to ensure that they function properly [14, 33]. Smart materials such as *shape memory alloys (SMAs)* have shown increased footprint in their implementation toward morphing wing design in recent years. SMAs are metals that perform actuation tasks driven by temperature modulation with high energy density. The thermal actuation of SMAs originates from shape deformations caused by a solid-to-solid material phase transition, also known as the shape memory effect. Typical SMAs exhibit strain of up to 5% at their low-temperature martensite phase, and the strain is recoverable upon returning to their high-temperature austenite phase through heating. The shape memory effect enables SMA-based components to behave as both thermal sensors, actuators, and structural elements. The advantages of SMAs include being lightweight, compact, and actuation that are silent and free of debris [9, 23]. Altogether, the high actuation energy density enables SMAs to be excellent candidates for wing morphing applications. Leal *et al.* presented a morphing wing design with SMA actuator components embedded in the skin of the airfoil [33]. Saunders *et al.* fabricated a twisting wing that implements a SMA torque tube to provide spanwise twisting [58]. Nevertheless, designs that incorporate compliant SMA-based components (*e.g.,* SMA skins and rods) require customized SMA designs that are expensive and require comprehensive material testing. Although shape memory alloy torque tubes present a simple design solution for wing morphing systems, their drawbacks include high production cost and slow actuation—making them inferior to SMA wire actuators. Among various designs reported in literature, two concepts were fabricated by Kang *et al.* [30] and Emiliavaca *et al.* [16] which featured camber morphing wings with config-

[2]Portions of this section are reprinted or adapted from Ref. [22]

urable internal support structures enabled by SMA wires and springs. The aforementioned attractive properties of tensegrity structures, coupled with the actuation ability of SMAs, enable them to be applicable for morphing wing designs. Further details of how the SMAs are incorporated into the tensegrity wing is laid out in Chapter 6.

## 1.5 Summary of Contributions and Outline of the Thesis

In summary, the main research contributions of this work are:

i Modeling of the aerodynamic characteristics of the torsional wing using computational fluid dynamics (CFD) simulations. This enables the comparison of the aerodynamic efficiency of the torsional wing against an equivalent conventional wing that possesses a control surface

ii Parameterization of the novel wing design by integrating the topology of the tensegrity mechanism with essential wing components (ribs, skin, spar)

iii Creation of a finite element model of the wing that integrates external aerodynamic loads with the internal loads exerted by the torsional mechanism for detailed analysis of the wing structural response

iv Performance of a design exploration study to evaluate the effects of varying the topological parameters of the wing on its twisting deformation, mass, and stress levels

v Performance of a design exploration study to evaluate the effects of other critical design variables such as spar diameter, rib and skin thicknesses, wire diameters, component materials vi Evaluation of utilizing shape memory alloys (SMAs) to facilitate torsional mechanism

The remainder of this thesis is organized as follows: Chapter 2 presents the analysis of the aerodynamic characteristics of the twisting wing and their comparison against those of a conventional wing; Chapter 3 describes the internal tensegrity mechanism that enables the twisting motion; Chapter 4 presents the finite element model used for the structural analysis of the wing; Chapter 5 describes the DOE studies conducted and their associated results; Chapter 6 presents an evaluation of using SMAs as a means to actuation; and Section 7 provides the conclusions and future works. A comprehensive list of symbols is provided in Appendix A.

# Chapter 2

# Aerodynamic Analysis of Twisting Wing

[1] [2] This chapter provides a brief review of the literature on the benefits of twisting wing designs and presents the computational fluids dynamics (CFD) analysis conducted to confirm the superior performance of a twisting wing against a conventional counterpart. In Section 2.1, multiple researches on twisting wings and their advantages are presented. Section 2.2 provides descriptions of the CFD models of the twisting wing and conventional wing that were built based on an existing vehicle. Lastly, a comparative study between such designs is presented in Section 2.3.

[1] Portions of this section are reprinted or adapted from [Nguyen K. Pham and Edwin A. Peraza Hernandez, 2021, "Modeling and design exploration of a tensegrity-based twisting wing," Journal of Mechanisms and Robotics. https://doi.org/10.1115/1.4050149]. Figures and texts are reprinted by permission of the American Society of Mechanical Engineers.

[2] Portions of this section are reprinted or adapted from [Nguyen K. Pham and Edwin A. Peraza Hernandez, 2021, "Modeling and design exploration of a morphing wing enabled by a twisting tensegrity mechanism," Proceedings of the 2021 AIAA SciTech Forum and Exposition, AIAA 2021-0099, virtual conference. https://doi.org/10.2514/6.2021-0099]. Figures are reprinted by permission of the American Institute of Aeronautics and Astronautics, Inc.

## 2.1 Advantages of Twisting Wing

Twisting wing concepts have previously demonstrated their potential in improving aerodynamic efficiency. For example, Rodrigue and coworkers built a twisting wing prototype meant to be used in a UAV which delivered an approximate 13% improvement in the lift-to-drag ratio, a parameter often employed to quantify aerodynamic efficiency [54]. Furthermore, a work by Phillips *et al.* showed that wing twist is beneficial in minimizing induced drag by providing a way to optimize the spanwise load distribution [50]. The effectiveness of wing twisting in providing roll control has previously been studied and confirmed by Pecora *et al.* where they showed that the roll rates produced by wing twisting is approximately 1.6 times greater than that of ailerons [45]. Similarly, Cesnik and Brown confirmed that, during the cruising flight segment, wing morphing can provide 60% more roll control than an aileron [10].

## 2.2 Computational Fluid Dynamics (CFD) Model

To explore the twisting wing concept herein, the rectangular wing of the Carl Goldberg Falcon 56 Mk II R/C UAV with a chord length ($c$) of 25.31 cm and a wingspan ($s$) of 142.24 cm is adopted. Figure 2.1 is a photograph of the vehicle for reference. This vehicle is chosen for the high stall angle of attack of its airfoil which potentially allows for larger twist angles to be achieved without stalling any portion of the wing. Furthermore, using a functional vehicle as the base design presents the feasible prospect of testing the final morphing wing.

Three-dimensional CFD analyses are conducted in `Ansys`™ engineering simulation software to explore the aerodynamic performance of the twisting wing design and the original wing of the UAV with a trailing flap. The coordinates of the points defining the outline of the Falcon airfoil, as shown in Fig. 2.3, are imported from [1] into `Ansys` and connected and


Figure 2.1: Carl Goldberg Falcon 56 Mk II R/C UAV reference vehicle.

extruded to form the three-dimensional models of the wings. Computational models of the twisting wing adaptation and its original form that includes a single control surface are shown in Figs. 2.2(a) and 2.2(b), respectively. In Fig. 2.2(a), the reference *angle of attack* ($\alpha$) is defined as that between the chord line at the wing root and the airflow direction while the *twist angle* ($\Phi$) is defined as the difference between the local angle of attack at the wing tip and $\alpha$. In Fig. 2.2(b), the *flap deflection angle* ($\delta$) is defined as the difference in the flap orientation and the angle of attack of the wing.

For both models, practical values of $\alpha$ from -2° to 10° are considered in the CFD analyses. For the case of the twisting wing, the twist angle $\Phi$ is varied from 0° to 12°. In the case of the conventional wing, the flap deflection angle $\delta$ is varied from 0° to 35°. After each simulation is completed, the obtained response variables of interest are the wing lift and drag coefficients ($C_L$ and $C_D$, respectively), which are non-dimensional and respectively scale the lift and drag forces experienced by the wing during flight. An incoming airflow speed of 20 m/s is assumed in all simulations, which is a typical airspeed of the Carl Goldberg Falcon 56 Mk

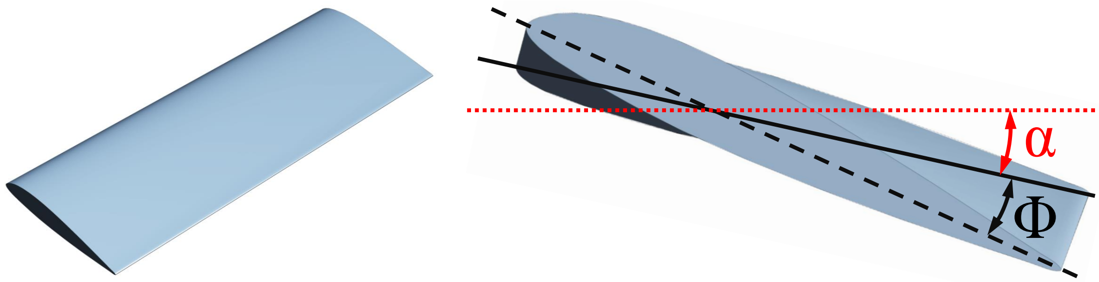


(a) Twisting wing.

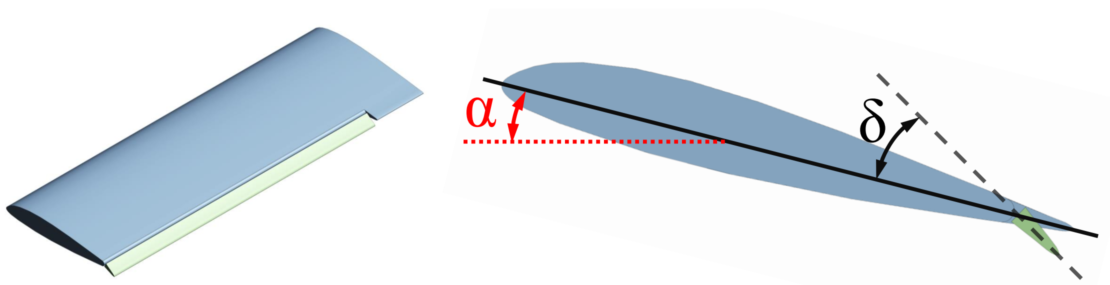


(b) Conventional wing.

Figure 2.2: Schematics of (a) twisting wing showing angle of attack $\alpha$ and total twist angle $\Phi$ and (b) conventional wing showing angle of attack $\alpha$ and flap deflection angle $\delta$. The solid lines represent the chord line and the dotted lines represent the airflow direction. Reprinted from [46].

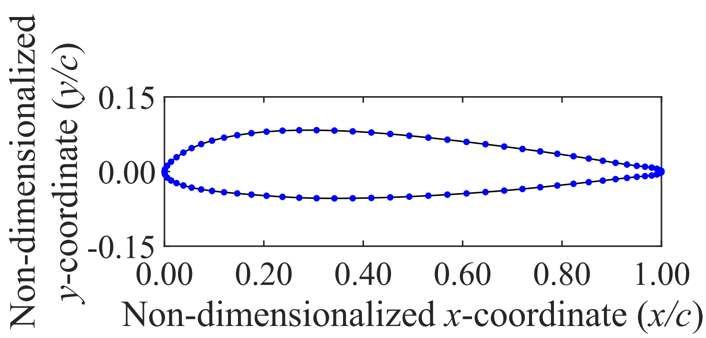


Figure 2.3: Coordinate points of the outline of the Falcon airfoil used to define the wing cross section [1]. Reprinted from [48].

II R/C UAV. As suggested by the `Ansys` manual, the Spalart-Allmaras turbulence model is used. This turbulence model allows for low demand in computing power while still provides reasonable accuracy in the calculated drag force. The mesh structure of the CFD analysis is shown in Fig. 2.4. The surfaces of the wing has higher mesh density to improve accuracy while the rest of the domain has coarser mesh to reduce computational time.

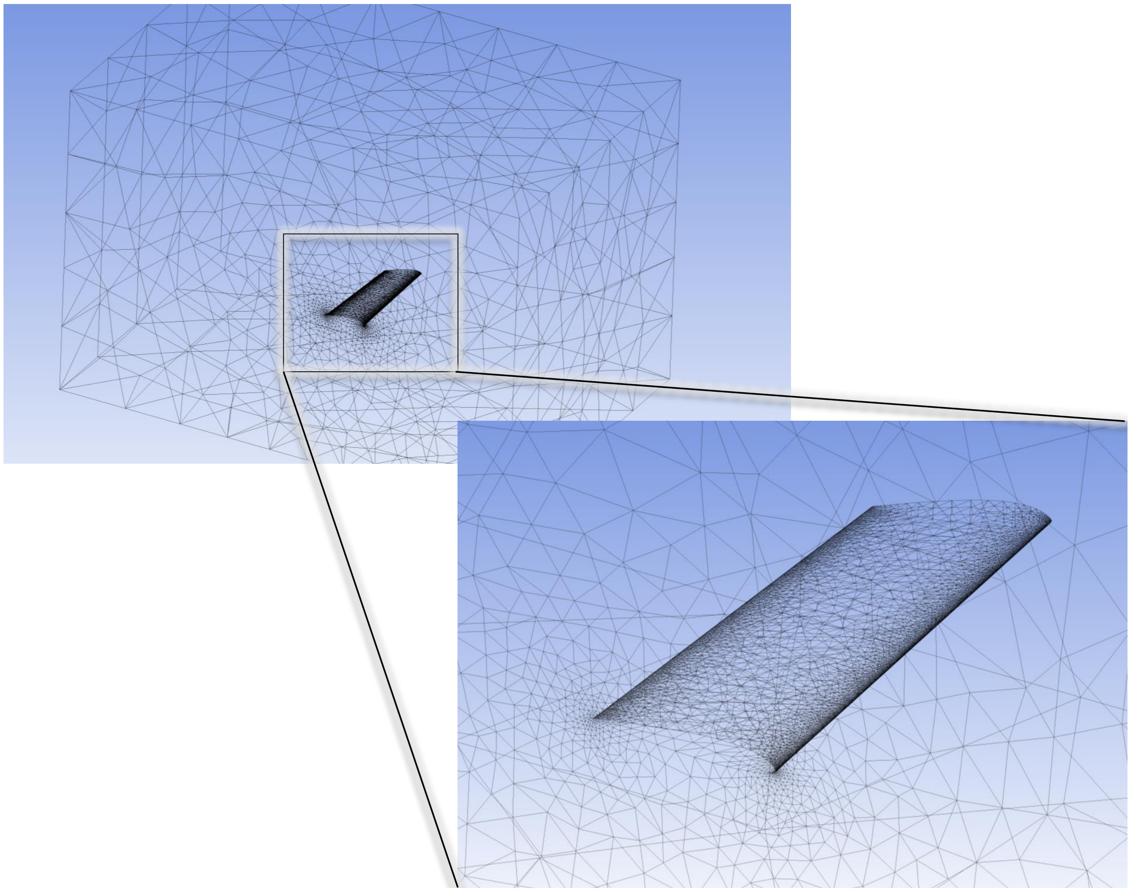

Figure 2.4: Illustration of mesh structure used in computation fluid dynamic analysis.

To confirm the validity of the CFD model, simulations are conducted for the smooth Falcon airfoil shape with angles of attack ($\alpha$) between -5°and 12°. The sectional lift coefficient ($c_l$) obtained from the CFD computations is then compared against wind tunnel data published in [59]. The CFD approach employed in this work was demonstrated by the authors to be in good agreement with experimental wind tunnel data in [47].

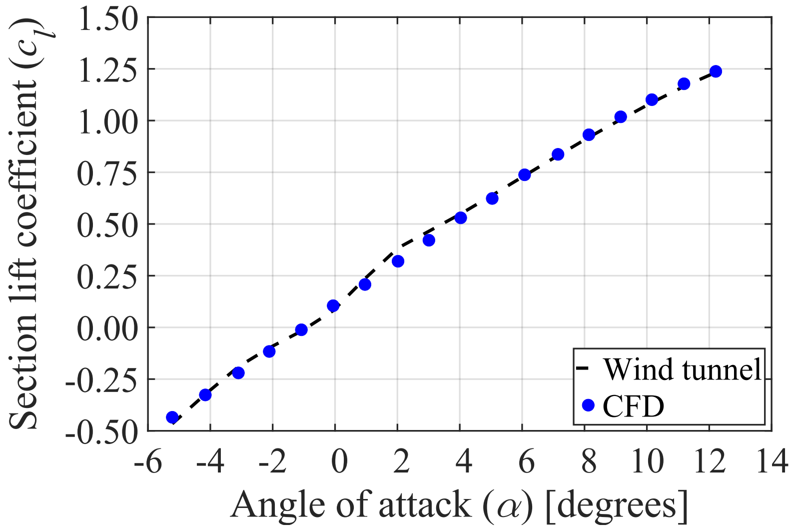


Figure 2.5: Sectional lift coefficient ($c_l$) vs. angle of attack ($\alpha$) of the Falcon airfoil. Wind tunnel data obtained from Ref. [59] is compared against CFD data generated using `Ansys`. Reprinted from [46].

## 2.3 Comparative Study Between Twisting Wing and Conventional Wing

The determined results of the lift and drag characteristics of the twisting wing and the conventional wing are provided in Figs. 2.6 - 2.8. Figure 2.6(a) shows the lift coefficient ($C_L$) as a function of twist angle ($\Phi$) and angle of attack ($\alpha$), while Fig. 2.6(b) shows $C_L$ as a function of the flap deflection angle ($\delta$) and $\alpha$. It is observed from these contour plots that the twisting wing provides a higher maximum $C_L$ when compared against a conventional wing. Additionally, given the same value of $\alpha$, $C_L$ increases much more rapidly when the wing twists than when the flap is deflected. Although this phenomenon can be partially attributed to the fact that the flap area is relatively small, the data suggests that, for the two studied wings, varying $\Phi$ has a much higher impact on $C_L$ than varying $\delta$. From these observations, it can be concluded that wing twisting can provide sufficient lift variation needed for roll and pitch control.

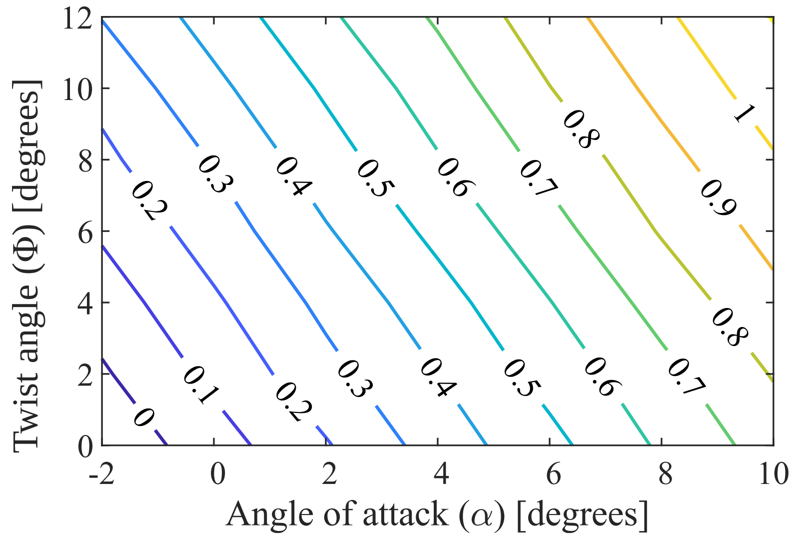


(a) Lift coefficient ($C_L$) of the twisting wing.

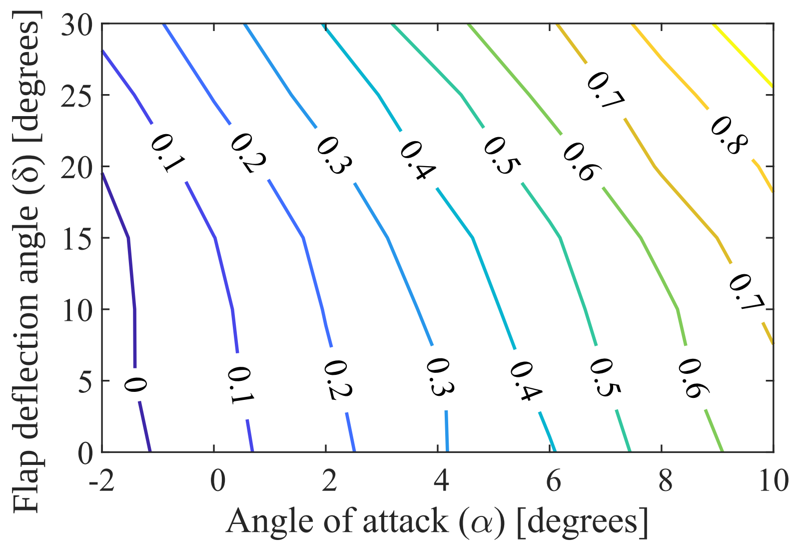


(b) Lift coefficient ($C_L$) of the conventional wing.

Figure 2.6: Contour plots of lift coefficient ($C_L$): (a) For the twisting wing shown in Fig. 2.2(a) in terms of total twist angle ($\Phi$) and angle of attack ($\alpha$); and (b) for the conventional wing shown in Fig. 2.2(b) in terms of flap deflection angle ($\delta$) and angle of attack ($\alpha$). Reprinted from [46].

Figure 2.7(a) shows the drag coefficient ($C_D$) variation as the twist angle ($\Phi$) and angle of attack ($\alpha$) vary, while Fig. 2.7(b) shows the impact of varying the flap deflection angle ($\delta$) and $\alpha$ on $C_D$. These contour plots provide a few interesting trends. Firstly, for low values of $\alpha$ ($< 4°$), the two wing designs have similar drag characteristics with the twisting wing delivering slightly less drag. This is desirable since aircraft typically cruise at lower angles of attack. The second trend observed was that as $\alpha$ increases, the conventional wing exhibits much better drag characteristics. This observation can be attributed to the fact that portions of the twisting wing, specifically the wing tip, begin to experience stall, thereby causing a much larger drag force, when both values of $\Phi$ and $\alpha$ are high. However, higher values of $\alpha$ are only needed during specific flight regimes like takeoff and landing and the effect of increased drag is offset by the rapid increment of lift.

Figure 2.8(a) shows the lift-to-drag ratio ($C_L/C_D$) as a function of twist angle $\Phi$ and angle of attack $\alpha$, while Fig. 2.8(b) shows $C_L/C_D$ as a function of the flap deflection angle $\delta$ and $\alpha$. Overall, these contour plots indicate that for any of the studied angles of attack $\alpha$, using wing twisting is more favorable in the achievement of higher lift-to-drag ratios than using a trailing flap. Thus, these results demonstrate that the twisting wing that does not use control surfaces is more aerodynamically efficient than the conventional wing.

To explore the effects of the discontinuities introduced by the trailing flap of the conventional wing, Fig. 2.9 shows the lift-to-drag ratio $C_L/C_D$ of the twisting and conventional wings having respectively a twist angle $\Phi$ and a flap deflection angle $\delta$ of $0°$. In these configurations, both wings have identical shapes with the only difference being that the twisting wing has a continuous outer surface and the conventional has a discontinuity between its main wing region and the flap. The curves in Fig. 2.9 show that the smooth and continuous surface of the twisting wing delivered superior performance–*i.e.,* improvement in lift-to-drag ratio– when compared to the conventional design with a separated flap in the domain of positive angles of attack, where aircraft normally cruise.

Figure 2.10 is a sample illustration of the pressure distribution over the wing external surface and the streamline pattern around the twisting wing. The figure shows lower pressure values at the top surface of the wing tip compared to the root, which indicates an increasing lift distribution along the wingspan direction.

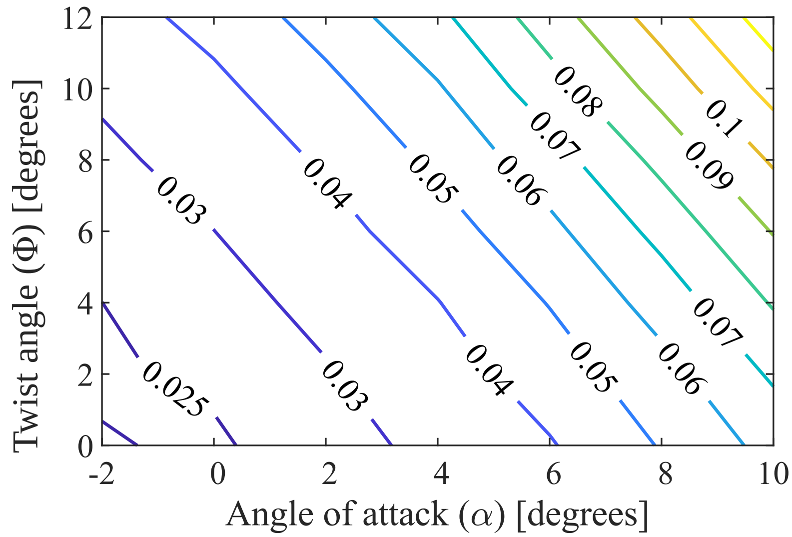


(a) Drag coefficient ($C_D$) of the twisting wing.

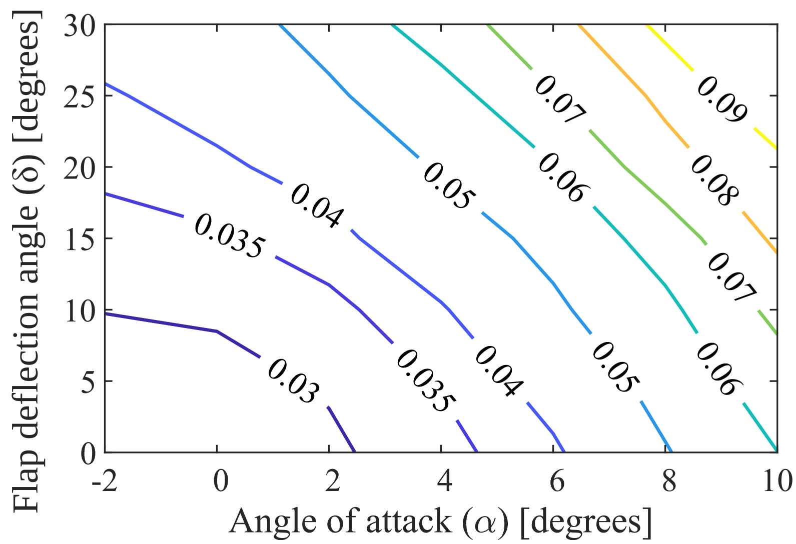


(b) Drag coefficient ($C_D$) of the conventional wing.

Figure 2.7: Contour plots of drag coefficient ($C_D$): (a) For the twisting wing shown in Fig. 2.2(a) in terms of total twist angle ($\Phi$) and angle of attack ($\alpha$); and (b) for the conventional wing shown in Fig. 2.2(b) in terms of flap deflection angle ($\delta$) and angle of attack ($\alpha$). Reprinted from [46].

Since the proposed wing design of this research is made up of high-performance, metallic material (specific material details will be provided in Chapter 4) that can be used in more demanding applications while the reference Carl Goldberg Falcon 56 Mk II vehicle is made up of light-weight balsa wood, a direct comparison between the two vehicles cannot be made.

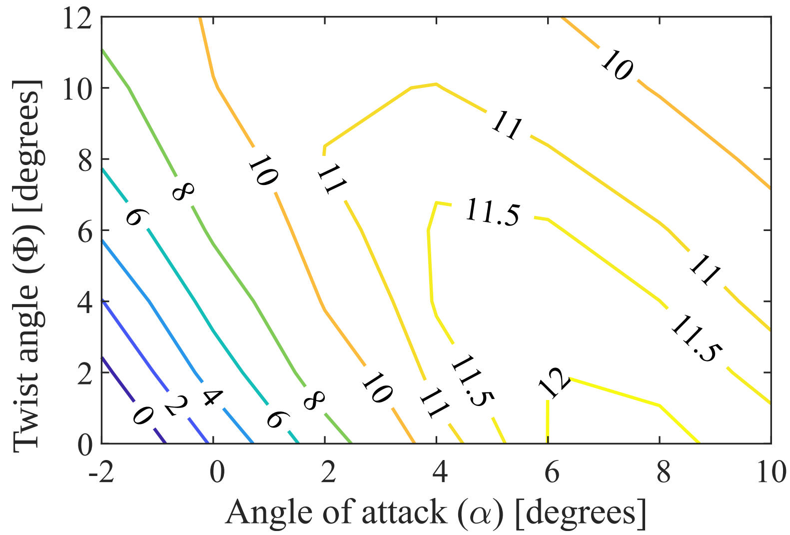


(a) Lift-to-drag ratio ($C_L/C_D$) of the twisting wing.

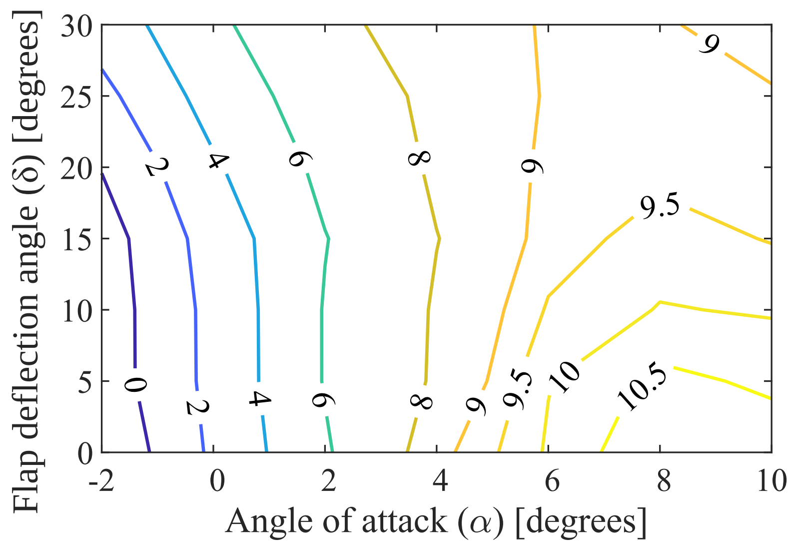


(b) Lift-to-drag ratio ($C_L/C_D$) of the conventional wing.

Figure 2.8: Contour plots of lift-to-drag ratio ($C_L/C_D$): (a) For the twisting wing shown in Fig. 2.2(a) in terms of total twist angle ($\Phi$) and angle of attack ($\alpha$); and (b) for the conventional wing shown in Fig. 2.2(b) in terms of flap deflection angle ($\delta$) and angle of attack ($\alpha$). Reprinted from [46].

Nonetheless, the aerodynamic analysis presented in this chapter offers valuable insights and reaffirms the superior performance of the twisting wing thereby justifies the design motivation. Furthermore, the trends observed in this chapter remains relevant even for much bigger wing designs since the data obtained were dimensionless. Even though for bigger wings, the data will be slightly different due to the change in the Reynolds Number, the overall behavior remains the same.

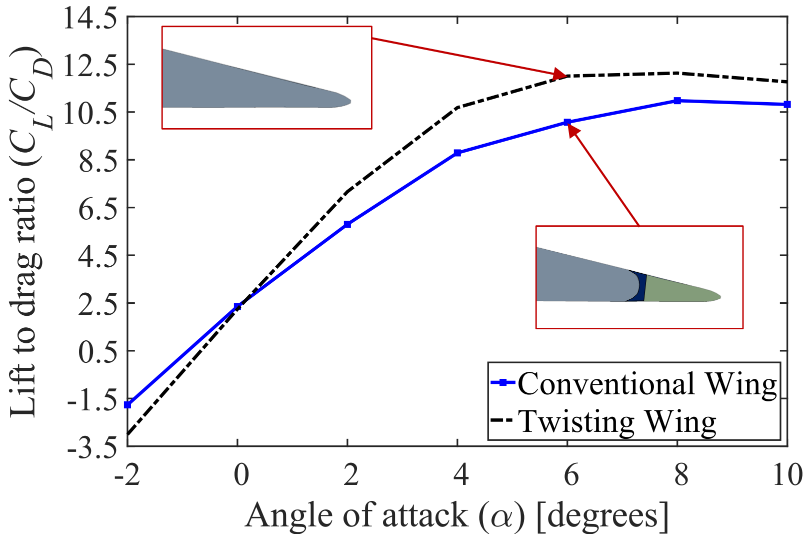


Figure 2.9: Lift-to-drag ratio ($C_L/C_D$) of the conventional and twisting wings with no flap deflection ($\delta = 0°$) and no twist ($\Phi = 0°$), respectively. Close-up views of the trailing edge of both wings are illustrated. Reprinted from [46].

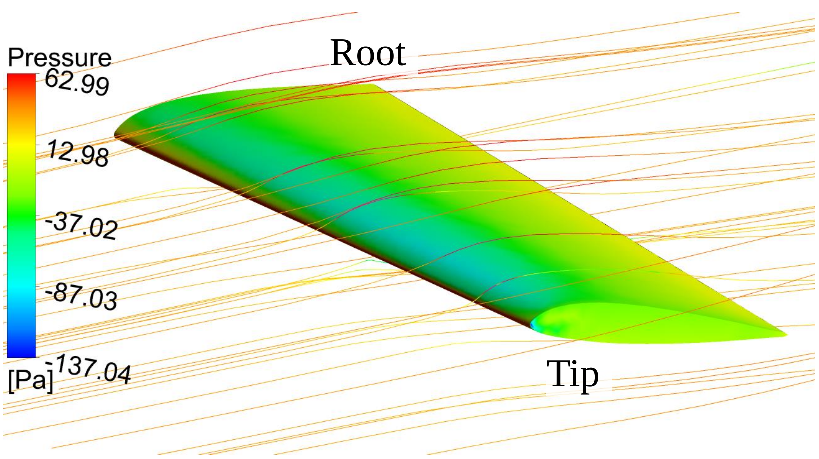


Figure 2.10: Pressure distribution on a sample twisting wing surface and flow streamline visualization. Reprinted from [46].

# Chapter 3

# Implementation of Torsional Tensegrity Mechanism

[1] [2]Having demonstrated the advantages in aerodynamic efficiency of a smooth twisting wing compared to legacy designs with control surfaces, this chapter proceeds to the description of the torsional tensegrity mechanism that enables such a twisting motion. The torsional tensegrity mechanism devised herein is inspired by the twisting column described in [62], which was applied to a cylindrical tower.

[1]Portions of this section are reprinted or adapted from [Nguyen K. Pham and Edwin A. Peraza Hernandez, 2021, "Modeling and design exploration of a tensegrity-based twisting wing," Journal of Mechanisms and Robotics. https://doi.org/10.1115/1.4050149]. Figures and texts are reprinted by permission of the American Society of Mechanical Engineers.

[2]Portions of this section are reprinted or adapted from [Nguyen K. Pham and Edwin A. Peraza Hernandez, 2021, "Modeling and design exploration of a morphing wing enabled by a twisting tensegrity mechanism," Proceedings of the 2021 AIAA SciTech Forum and Exposition, AIAA 2021-0099, virtual conference. https://doi.org/10.2514/6.2021-0099]. Figures are reprinted by permission of the American Institute of Aeronautics and Astronautics, Inc.

## 3.1 Tensegrity Column Design

The torsional tensegrity mechanism used in this work is comprised by a set of *rings*, *ribs*, and a *central spar* connected by a *network of wires*. Figure 1.1 depicts an early prototype of the mechanism while Fig. 3.1 provides a close-up schematic view of the various components forming the mechanism. The network of wires represents the tensile strings of the tensegrity system. The central spar is aligned along the span direction of the wing and runs from root to tip. It provides bending stiffness to the wing. The rings distributed along the length of the spar are allowed to rotate relative to it. Each of the internal ribs possesses a circular hole with a diameter larger than that of the central cylindrical spar, along which the central spar passes. The ribs are responsible for maintaining the airfoil shape of the wing under internal twisting motion and external aerodynamic forces. The torsional tensegrity mechanism is divided into various *cells* along the span of the wing, each bounded by two ribs. All the rings and ribs are concentric relative to the central spar, as shown in Fig. 3.1(a). The wires are evenly arranged in a circular pattern around the spar as illustrated in Fig. 3.1(b). The entire torsional tensegrity mechanism is covered with an external skin (not shown in Fig. 3.1) that enables the production of lift force and transfer of the external aerodynamic forces to the internal structure.

The wires are classified into longitudinal wires, stabilizer wires, and actuator wires, as indicated in Fig. 3.1(b). The *stabilizer wires* connect the ribs (located at the bounds of each cell) to the rings (located at the middle of each cell) and provide stability to these components. The *longitudinal wires* are oriented along the span direction of the wing at the initial configuration while the *actuator wires* are oriented off-axis.

When the length of the actuator wires is shortened, either by intrinsic material actuation or by mechanical means, these wires create a torque that produces twist within the mechanism. This twisting motion also causes the longitudinal wires to elongate and provide an opposing

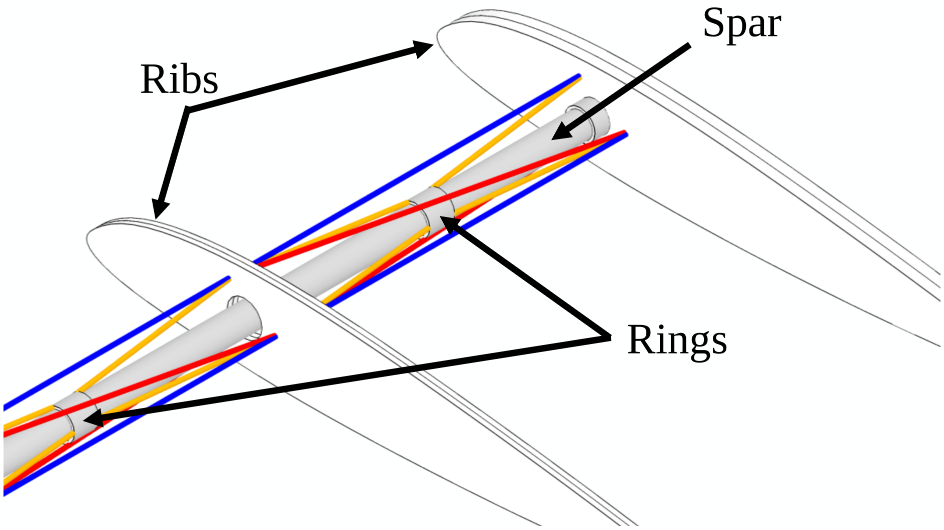


(a) Ribs, rings, and spar.

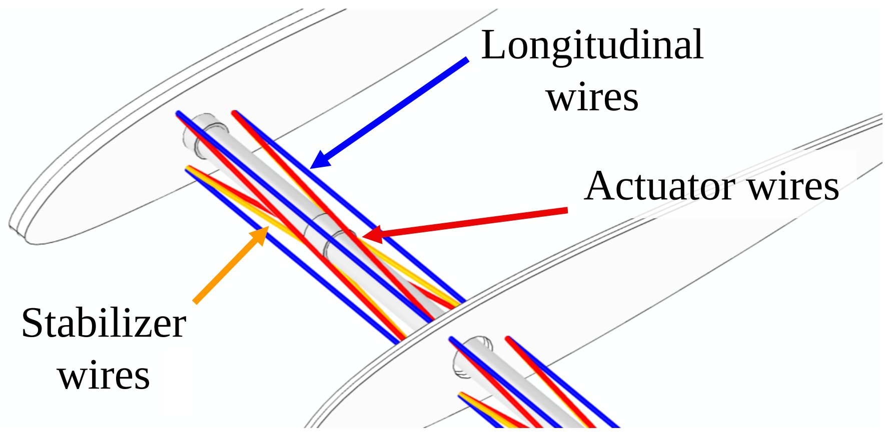


(b) Wire network.

Figure 3.1: Close-up view of the components of a cell within the torsional tensegrity mechanism. Reprinted from [46].

torque. When the actuator wires are relaxed, the torque exerted by the longitudinal wires restore the mechanism back to its original configuration. Figure 3.2 provides a simplified depiction of this process. This schematic also illustrates the twist angle of the individual cell ($\varphi$), measured between the two end faces of the cell.

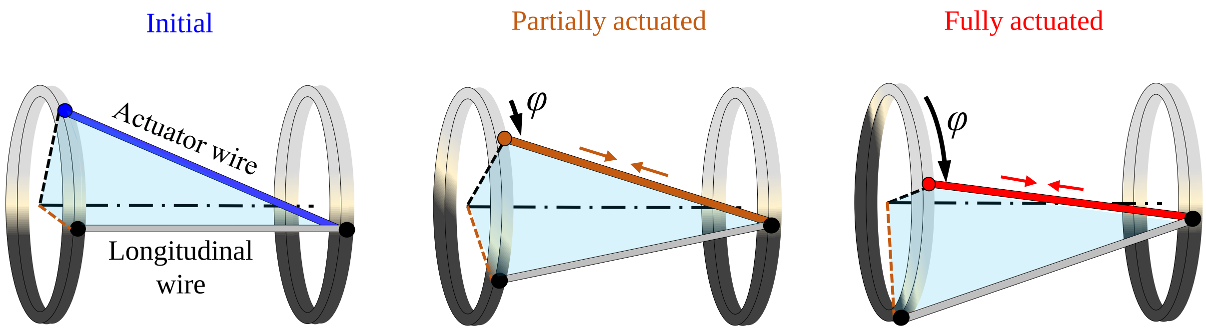


Figure 3.2: Simplified schematics of the initial, partially actuated, and fully actuated configurations of a cell in the torsional tensegrity mechanism illustrating how twisting deformation is obtained. Reprinted from [48].

## 3.2 Mathematical Derivation of Wire Network Placement

Figure 3.3 shows the coordinate system and index convention used to mathematically define the wire network within the torsional tensegrity mechanism. The origin of the right-handed, three-dimensional Cartesian coordinate system is set to coincide with the intersecting point of the axis of the spar and the rib at the wing root. The $x$-axis is collinear to the chord line of the airfoil and is oriented from the leading edge to the trailing edge. The $z$-axis is collinear to the axis of the spar and is oriented from the root of the wing to the tip. The $y$-axis completes the right-handed coordinate system.

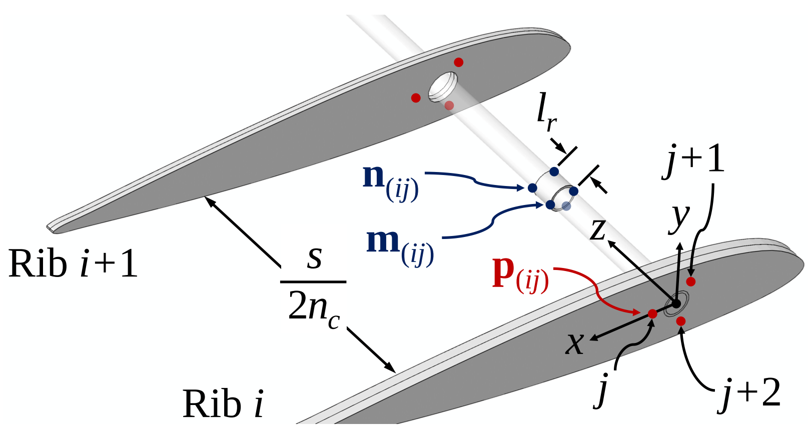


Figure 3.3: Schematic showing coordinate convention and wire end points $\mathbf{n}_{(ij)}$, $\mathbf{m}_{(ij)}$, and $\mathbf{p}_{(ij)}$. Adapted from [46].

The two topological design parameters of the tensegrity-based twisting wing are the *number of cells* ($n_c$) and *number of wire sets* ($n_w$). Each wire set features an actuator wire, a longitudinal wire, and two stabilizer wires. These two variables, $n_c$ and $n_w$, are considered in the DOE study presented in Section 5.1. Figure 3.4 shows torsional tensegrity mechanisms with 3, 5, and 7 cells along the wingspan, and Fig. 3.5 shows torsional tensegrity mechanisms with different number of wire sets.

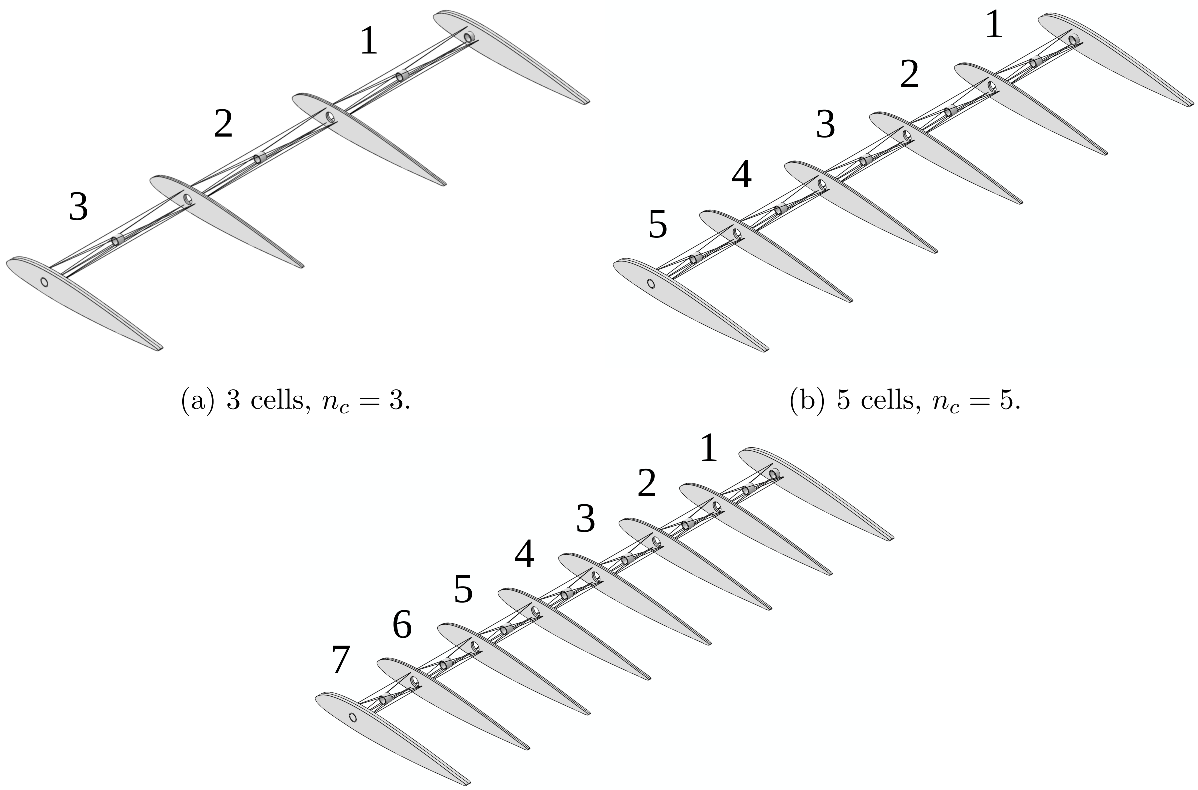


(a) 3 cells, $n_c = 3$.

(b) 5 cells, $n_c = 5$.

(c) 7 cells, $n_c = 7$.

Figure 3.4: Torsional tensegrity mechanisms having different number of cells. The central spar is omitted for the sake of visualization. Reprinted from [46].

The index $i \in \{0, \ldots, n_c - 1\}$ indicates the rib number starting from 0 at the wing root to $n_c - 1$ at the wing tip. The spacing of the ribs, or cell span, shown in Fig. 3.3 is given by $s/(2n_c)$.[3] The index $j \in \{0, \ldots, n_w - 1\}$ indicates the wire set number starting from the point that radially coincides with the $x$-axis ($j = 0$) and progresses in the counterclockwise direction of the $x$-$y$ plane. Since the wire sets are uniformly distributed in a circular pattern around the spar, the angle between each wire set is given by $2\pi/n_w$. Other size parameters involved in the wire network arrangement are the axial length of the rings ($l_r$, shown in Fig. 3.3), the radial distance between the wire end points and the center of the spar ($R$), and the middle radius of the rings ($r$). Both $R$ and $r$ are functions of the spar radius ($r_s$), one of the studied variables in the DOEs detailed in Chapters 5 and 6. The results obtained from those DOEs are discussed at the end of the respective chapters and reveal the effect of varying $r_s$, and thus these two parameters, on the twisting performance of the wing.

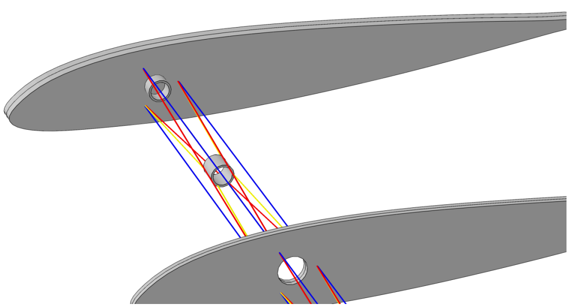

(a) 3 sets of wires, $n_w = 3$.

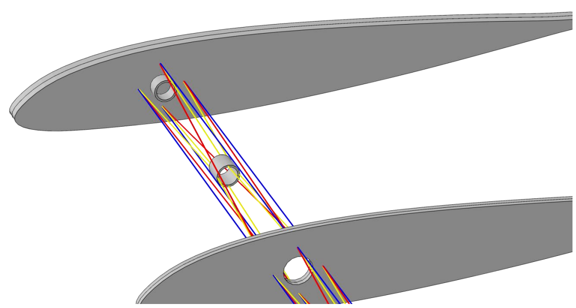

(b) 4 sets of wires, $n_w = 4$.

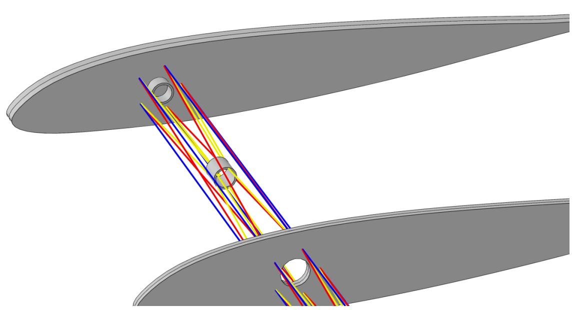

(c) 5 sets of wires, $n_w = 5$.

Figure 3.5: Torsional tensegrity mechanisms having different number of wire sets. The central spar is omitted for the sake of visualization.

[3]The wingspan $s$ includes the length of the two wings of an aircraft. Thus, a single wing has a length of $s/2$ from root to tip.

The position vectors of the wire end points are denoted by $\mathbf{p}_{(ij)}$, $\mathbf{m}_{(ij)}$, $\mathbf{n}_{(ij)} \in \mathbb{R}^3$. These points are respectively located at the ribs, at the root side of the rings, and at the tip side of the rings as indicated in Fig. 3.3. The components of the position vectors are defined as follows:

$$\mathbf{p}_{(ij)} = \begin{bmatrix} R\cos\left(\frac{2\pi j}{n_w}\right) \\ R\sin\left(\frac{2\pi j}{n_w}\right) \\ \frac{si}{2n_c} \end{bmatrix}, \tag{3.1}$$

$$\mathbf{m}_{(ij)} = \begin{bmatrix} r\cos\left(\frac{2\pi j}{n_w}\right) \\ r\sin\left(\frac{2\pi j}{n_w}\right) \\ \frac{s}{2n_c}\left(i+\frac{1}{2}\right) - \frac{l_r}{2} \end{bmatrix}, \tag{3.2}$$

$$\mathbf{n}_{(ij)} = \begin{bmatrix} r\cos\left(\frac{2\pi j}{n_w}\right) \\ r\sin\left(\frac{2\pi j}{n_w}\right) \\ \frac{s}{2n_c}\left(i+\frac{1}{2}\right) + \frac{l_r}{2} \end{bmatrix}. \tag{3.3}$$

Figure 3.6 provides illustrations of each type of wire. The layout of the wires is defined by the connectivity relations provided in Table 3.1. This table defines the end points of each of the wires in the torsional tensegrity mechanism. For example, the positions of the end points of the longitudinal wire with indices $i = 2$ and $j = 1$ are $\{\mathbf{p}_{(21)}, \mathbf{p}_{(31)}\}$, the positions of the end points of the actuator wire with the same indices are $\{\mathbf{p}_{(21)}, \mathbf{p}_{(32)}\}$, and the positions of the end points of the two stabilizer wires with the same indices are respectively $\{\mathbf{p}_{(21)}, \mathbf{m}_{(21)}\}$ and $\{\mathbf{n}_{(21)}, \mathbf{p}_{(31)}\}$. In total, the torsional tensegrity mechanism contains $n_c n_w$ longitudinal wires, $n_c n_w$ actuator wires, and $2n_c n_w$ stabilizer wires.

Within each cell, the longitudinal wires are attached to the two ribs bounding the cell. The end points of the longitudinal wires share the same index $j$ (indicating that they have the same radial coordinate) since they are oriented parallel to the spanwise direction. This arrangement enables them to stretch when the wing is twisted. Thus, they can restore the wing to its untwisted configuration after the wing undergoes torsional deformation. The actuator wires also span the entire cell; however, the end points of the actuator wires at rib $i$ have an index of $j$ while the end points at rib $i+1$ have an index of $j+1$. This radial coordinate selection provides the actuator wires with an angular deviation from the spanwise direction, which allows them to twist each cell of the wing when they are contracted. Lastly, the end points of each stabilizer wire share the same index $j$. Each stabilizer wire connects a rib to a ring to ensure stability and concentricity of the entire tensegrity mechanism.

| **Wire type** | **Start point** | **End point** |
|---|---|---|
| Longitudinal | $\mathbf{p}_{(ij)}$ | $\mathbf{p}_{(i+1\ j)}$ |
| Actuator | $\mathbf{p}_{(ij)}$ | $\mathbf{p}_{(i+1\ j+1 (\mathrm{mod}\, n_w))}$ |
| Stabilizer | $\mathbf{p}_{(ij)}$<br>$\mathbf{n}_{(ij)}$ | $\mathbf{m}_{(ij)}$<br>$\mathbf{p}_{(i+1\ j)}$ |

Table 3.1: Wire end point connectivity; $i \in \{0, \ldots, n_c - 1\}, j \in \{0, \ldots, n_w - 1\}$.

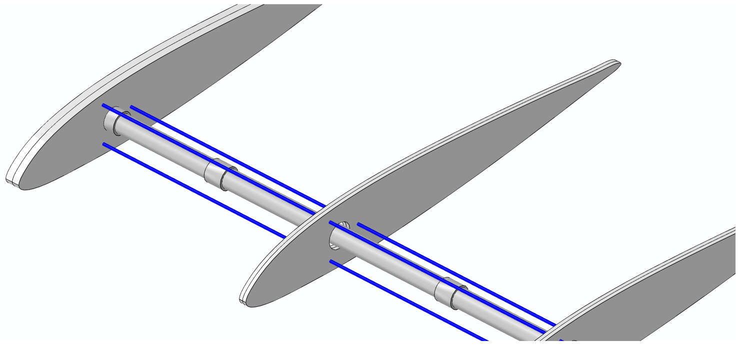

(a) Longitudinal wires.

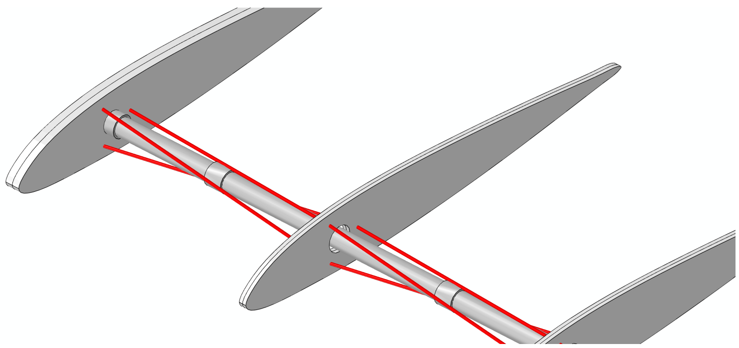

(b) Actuator wires.

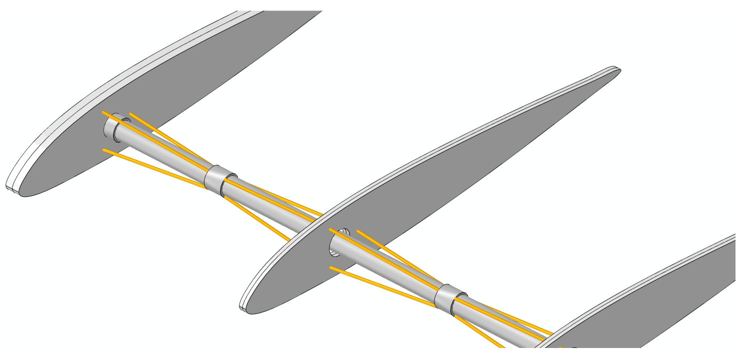

(c) Stabilizer wires.

Figure 3.6: Placement of (a) longitudinal wires, (b) actuator wires, and (c) stabilizer wires. Reprinted from [46].

# Chapter 4

# Finite Element Model

[1] [2] After defining the torsional tensegrity mechanism that enables the twisting motion of the wing in the previous chapter, a finite element model (FEM) of the entire wing is developed to explore its deformation and stress responses. Section 4.1 outlines the development of the parametric FEM and the boundary conditions imposed. Section 4.2 describes the methods used to simulate the actuator wire contraction. Finally, Section 4.3 provides details regarding the post-processing steps required after each simulation is completed. `Abaqus CAE`™ is employed to perform finite element analysis (FEA) in this study. Again, a chord length ($c$) of 25.31 cm and a wingspan ($s$) of 142.24 cm are assumed based on the rectangular wing of the Carl Goldberg Falcon 56 Mk II R/C UAV.

[1] Portions of this section are reprinted or adapted from [Nguyen K. Pham and Edwin A. Peraza Hernandez, 2021, "Modeling and design exploration of a tensegrity-based twisting wing," Journal of Mechanisms and Robotics. https://doi.org/10.1115/1.4050149]. Figures and texts are reprinted by permission of the American Society of Mechanical Engineers.

[2] Portions of this section are reprinted or adapted from [Nguyen K. Pham and Edwin A. Peraza Hernandez, 2021, "Modeling and design exploration of a morphing wing enabled by a twisting tensegrity mechanism," Proceedings of the 2021 AIAA SciTech Forum and Exposition, AIAA 2021-0099, virtual conference. https://doi.org/10.2514/6.2021-0099]. Figures are reprinted by permission of the American Institute of Aeronautics and Astronautics, Inc.

## 4.1 Finite Element Parametric Modeling

The geometry and topology of the finite element model are parameterized using a `Python` script along with a `MATLAB`™ algorithm. The `MATLAB` algorithm allows for a wide range of design parameters such as the number of cells ($n_c$) and wire sets ($n_w$), the thickness of the skin ($t_s$) and ribs ($t_r$), spar radius ($r_s$), the wire diameters ($d_{act}$) and ($d_{pass}$), and the material types of three primary component groups to be considered. It also generates the design space required based on the number of inputs and the options available. The `Python` script then receives the design inputs from `MATLAB` and proceeds to automatically create the FEA model and provide the structural responses.

Three-dimensional continuum elements are used to represent the spar and the rings. Shell elements are used to represent the ribs and the skin due to their small thickness compared to their planform dimensions. Truss elements are used to model all the wires. Specifically, the spar is modeled as a cylinder discretized by `C3D8R` elements (eight-node brick elements with reduced integration). The rings are discretized using `C3D10` elements (10-node tetrahedral elements). The skin and the ribs are discretized using `S4R` elements (linear 4-node shell elements with reduced integration). Stiffeners, often observed in wings, are omitted to simplify the model. Finally, the wire members are discretized using `T3D2` elements (2-node linear 3-D truss). The points connecting the wires to the ribs and rings are enforced to be nodal locations. A mesh convergence study is conducted to ensure that an appropriate mesh refinement is employed. Figure 4.1 shows a sample mesh discretization of the external and internal components of the wing.

The analysis step type employed in the `Abaqus` simulations is dynamic-implicit, considering quasi-static deformations. The implicit scheme allows the step size to be large without yielding significant inaccuracy in the obtained solutions. Non-linear geometry (*i.e.*, `NLGEOM` in `Abaqus` [7]) is used because various locations of the wing, particularly the tip, undergo large rotations.

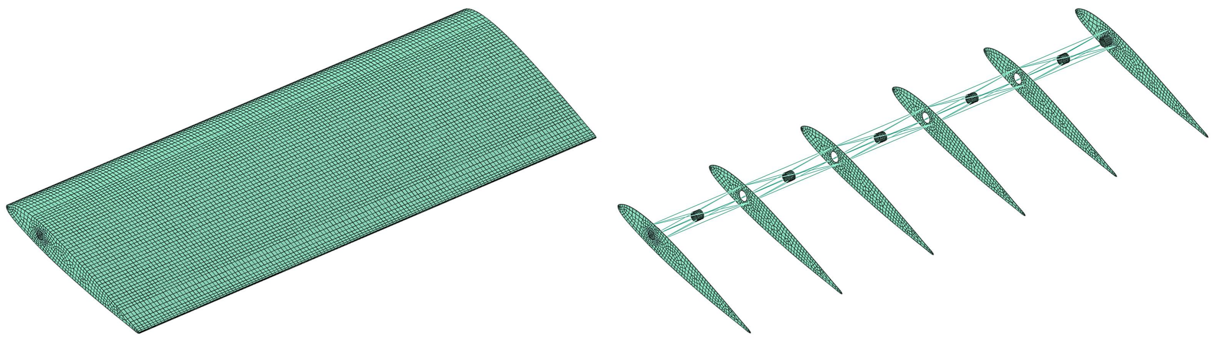

Figure 4.1: Finite element meshes of external and internal components of the tensegrity-based twisting wing. Reprinted from [46].

The boundary conditions of the finite element model are illustrated in Fig. 4.2. The rib at the root of the wing is fully fixed, representing its attachment to the fuselage. An additional ring is placed on the root rib at the location where the spar comes into contact with this rib. A non-penetration, frictionless contact interaction is defined between the spar, the root rib, and the inner face of the ring at this location to constrain the spar movement to only rotation about its own axis. On the opposite side, the rib at the tip of the wing also has an additional ring attached to it, which is tied to the tip end of the spar. Another non-penetration, frictionless contact interaction is defined between the inner face of the rings distributed along the wingspan and the circumferential face of the spar. This contact interaction ensures that the rings stay concentric to the spar and are allowed to freely rotate relative to the spar.

The CFD analyses described in Section 2.2 provide the pressure coefficient ($c_p$) distribution of the airfoil along the top and bottom surfaces of the wing, which is shown in Fig. 4.3. The pressure coefficient $c_p$ is defined as:

$$c_p = \frac{p - p_\infty}{\frac{1}{2}\rho v^2}, \tag{4.1}$$

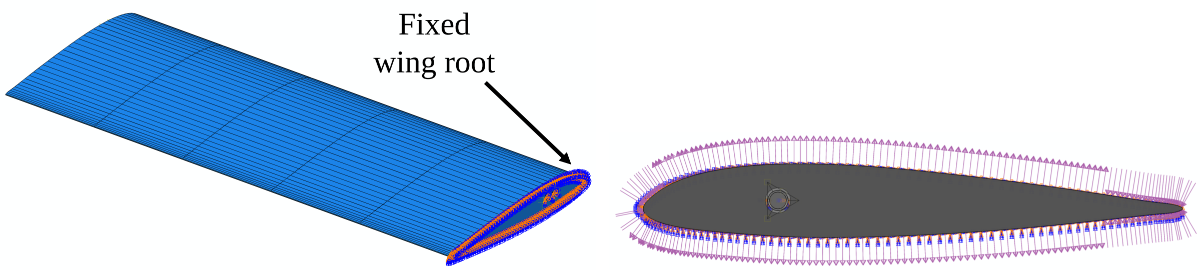


(a) Fixed wing root.

(b) Pressure distribution.

Figure 4.2: Boundary conditions: (a) Fixed wing root, and (b) aerodynamic pressure distribution on wing skin. Reprinted from [48].

where $\frac{1}{2}\rho v^2$ is the dynamic pressure, $\rho$ is the air density, $v$ is the air speed, $p_\infty$ is the ambient pressure, and $p$ is the total air pressure. These values are assumed at standard sea level air density ($\rho = 1.225$ kg/m$^3$ and $p_\infty = 101325$ Pa) and typical air speed for the Carl Goldberg Falcon 56 Mk II R/C UAV ($v = 20$ m/s). The pressure applied at each location in the wing skin ($\Delta p = p - p_\infty$) is calculated using Eq. (4.1) and the local value of $c_p$, and is then mapped onto the external surfaces of the wing in the finite element model to simulate the aerodynamic loads.

In the FEA model, just as in potential prototypes of the studied morphing wing, the skin is directly bonded to the ribs to ensure that the aerodynamic airfoil shape of the wing is maintained during torsional deformation. This also improves the overall structural integrity of the wing as bonding the ribs with the skin prevents significant wrinkles and warping to be exhibited on the skin resulting from the interactions between these two components during morphing.

The components of the wing are divided into four categories based on their function within the wing structure. The first group includes the ribs, spar, and stabilizer rings. These components were assumed to be made from metal sheets or bars. Aluminum alloys and Titantium alloys, both commonly used within the aerospace industry were considered candidates. The second category of material covers the external skin. Since the skin must be flexible to be

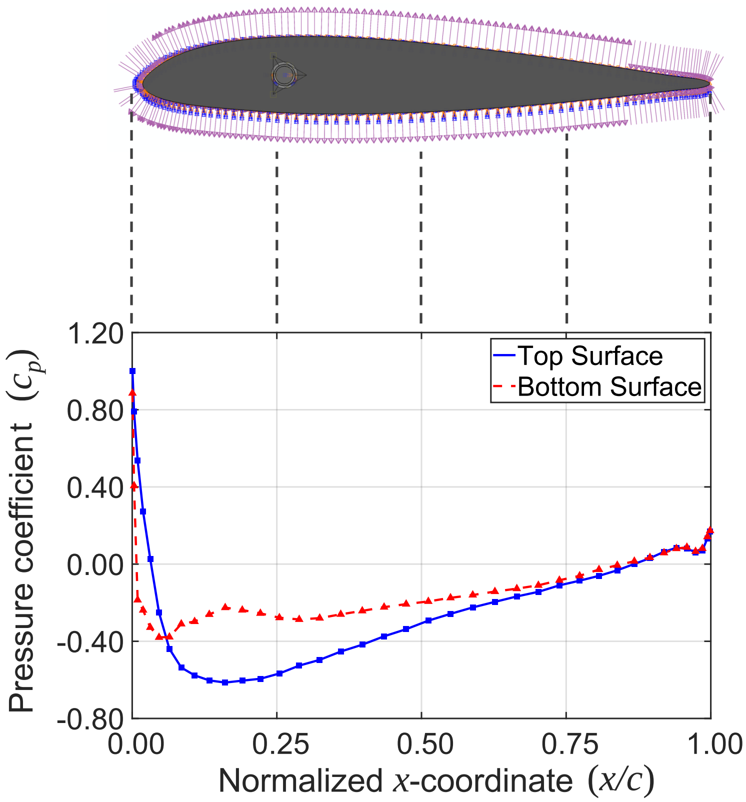


Figure 4.3: Section pressure coefficient distribution at $\alpha = 0°$. Reprinted from [22].

morphed during wing twisting while remain adequately stiff to sustain aerodynamic loads and debris, flexible engineered polymers are the preferred choice. For simplicity, the longitudinal and stabilizer wires, both of which are passive wires, are assumed to be made from the same material. These members are the primary load-bearing members of the tensegrity structure and therefore need to be made from metallic alloys. Lastly, the actuator wires belong to a group on their own. Specific material candidates and their respective performance will be provided and discussed in Chapter 5.

## 4.2 Simulating Actuation Mechanism

The author implemented two different methods to simulate the contraction of the contraction behavior of the actuator wires of the torsional tensegrity mechanism. As previously discussed in Section 3.1, the actuator wires can be activated via either intrinsic material properties or through mechanical means. However, both of the mentioned options require further studies and analysis. Initially, for the studies presented in Sections 5.1 – 5.2, to simulate the contraction, an artificial thermal expansion coefficient of 0.0004 m/(mK) is assigned to the material of the actuator wires. As a boundary condition, a temperature change of −10 K is applied, which causes the actuator wires to contract by a strain amount of 0.004 (0.4%) and twist the wing.

[3] Chapter 6 provides an introduction to shape memory alloys and and evaluation for the use of SMAs as a viable option to actuate the torsional deformation. In the DOE presented in Section 6.3, the user-defined material subroutine (`UMAT`) for SMAs—developed by Karakalas and colleagues [31]—is used to create the shape memory material assignment for the actuator wires. The properties of the SMA used will be further presented in Section 6.1. To facilitate the torsional tensegrity mechanism via activation of the shape memory actuator wires, a temperature increase of 135° K, starting from 238° K, is implemented as a boundary condition.

## 4.3 Post-processing

After each simulation, the `Python` script of the FEA model exports *structural mass* ($m_s$), the node coordinate variables, and the stress variables. The post-processing script then detects the time step where any of the components reached the tensile strength. The maximum von

[3]Portion of this paragraph is adapted from Ref. [22].

Mises stress ($\sigma_{VM}$) of each component group is then extracted from the stress outputs. From the coordinate variables, the $x$- and $y$-coordinates of the leading edge and the trailing edge of the rib at the tip of the wing are extracted and used to calculate $\Phi$, the *total twist angle*. From these output variables, the most favorable design of each study is selected based on the ratio between $\Phi$ and $m_s$ (*i.e.,* the *twist angle per unit mass*), a figure of merit that is denoted by $\eta$ and is defined as:

$$\eta = \frac{\Phi}{m_s}. \tag{4.2}$$

The most efficient and thus most favorable design has the highest value of $\eta$.

The `Abaqus CAE` post-processing module also helps in creating contour plots of the deformation and stress levels. These contour plots reveal valuable insights to the overall structural responses and help identify unintended phenomenon. For example, the occurrence of wrinkles on the skin as the wing deforms and areas of high stress concentrations that require additional reinforcement were both observed and identified in these contour plots.

As part of post-processing, `MATLAB` is used primarily to process the output data. One routine is created to generate the Pareto frontier chart which reveals the set of most favorable designs based on the minimum mass, maximum twist angle criteria. Another set of `MATLAB` routine are created to generate contour plots and main effect plots which reveal the impacts of varying design variables and unveil which variable has the largest impacts on the overall performance. These plots and their respective interpretation are provided in Chapter 5 and 6.

## 4.4 Scalability of Tensegrity System

As previously mentioned, tensegrity systems are highly scalable and this concept can be scaled up and be applied to bigger design systems. Although the size variables of the FEA models presented in this chapter were based on the RC-scale Carl Goldberg Falcon 56 Mk II UAV, the primary components such as the ribs, rings, skin, and spar can be manufactured to any desired size using any conventional manufacturing methods with commercially available materials. As for the wires, if thicker wires are needed to actuate and stabilize bigger wings, they can simply be weaved from smaller wires. Lastly, a unique property of tensegrity system and one that makes it reliable is the fact that the load-bearing members uniformly experience either tensile or compression loads such that there is no complex multidirectional stress fields that can trigger additional failure modes, as such, they can be scaled to much larger sizes.

# Chapter 5

# Design of Experiment Studies

[1] [2]This chapter provides an overview of the design of experiment (DOE) studies that were conducted. Section 5.1 details the first DOE which analyzed the impact of varying two topological parameters, the number of cells and number of wire sets. Section 5.2 is a case study that was done to analyze the effect of cell spacing. Finally, Section 5.3 describes a DOE that analyzed the effect of varying ten different design variables.

## 5.1 Topological Design Parameters Impact

As mentioned in Section 3.1, two topological design parameters of the tensegrity-based twisting wing are the *number of cells* ($n_c$) and *number of wire sets* ($n_w$). A DOE study using

[1]Portions of this section are reprinted or adapted from [Nguyen K. Pham and Edwin A. Peraza Hernandez, 2021, "Modeling and design exploration of a tensegrity-based twisting wing," Journal of Mechanisms and Robotics. https://doi.org/10.1115/1.4050149]. Figures and texts are reprinted by permission of the American Society of Mechanical Engineers.

[2]Portions of this section are reprinted or adapted from [Nguyen K. Pham and Edwin A. Peraza Hernandez, 2021, "Modeling and design exploration of a morphing wing enabled by a twisting tensegrity mechanism," Proceedings of the 2021 AIAA SciTech Forum and Exposition, AIAA 2021-0099, virtual conference. https://doi.org/10.2514/6.2021-0099]. Figures are reprinted by permission of the American Institute of Aeronautics and Astronautics, Inc.

the FEA model presented in the previous chapter is conducted to evaluate the structural response of tensegrity twisting wings having different combinations of $n_c$ and $n_w$. The numbers of cells is varied from three to nine while the number of wire sets is varied from three to ten.

The list of assumed size parameters employed in this study is summarized in Table 5.1. Diameters for the longitudinal, stabilizer, and actuator wires are adopted based on market availability. The skin thickness is assumed to be 1.25 mm based on the standard sheet thickness of the material employed for this component. The internal ribs dividing the cells of the torsional mechanism have a thickness of 8.00 mm whereas the ribs at the two ends are designated to be 16.00 mm thick, which ensures sufficient stiffness at the wing tip and root. Finally, the spar diameter, $R$, and $r$ are respectively assumed to be 12.00 mm, 15.00 mm, and 6.60 mm.

| **Parameter** | **Value [unit]** |
|---|---|
| Wingspan ($s$) | 142.2 [cm] |
| Chord length ($c$) | 25.31 [cm] |
| Skin thickness | 1.25 [mm] |
| Thickness of internal ribs | 8.00 [mm] |
| Thickness of root and tip ribs | 16.00 [mm] |
| Spar diameter | 12.00 [mm] |
| Radial distance between the wire end points and the center of the spar ($R$) | 15.00 [mm] |
| Middle radius of the rings ($r$) | 6.60 [mm] |
| Diameter of longitudinal and stabilizer wires | 0.81 [mm] |
| Diameter of actuator wires | 3.25 [mm] |

Table 5.1: Assumed size parameters for topological design parameter DOE.

Three materials are used in the model and Table 5.2 lists their relevant parameters which include the tensile modulus, Poisson's ratio, yield strength, and mass density. All materials are assumed to be isotropic and linearly elastic since strains are not expected to exceed the small strain regime. A factor of safety of 1.5 is assumed. Aluminum 6061-T6, a traditional and commonplace aerospace alloy, is assigned to the rings, ribs, and the spar. This material group is shown in Fig. 5.1(a). The material parameters of aluminum 6061-T6 are obtained from [36]. Grade 5 Titanium alloy is used for the wires and its material parameters are obtained from [2]. Since titanium alloys typically possess high tensile strength, they are an ideal candidate for the tensile, load-bearing members of the tensegrity mechanism used in this wing. For simplicity, it is assumed that all the wires are composed of the same material in this study. An illustration of the Grade 5 Titanium alloy material group is provided in Fig. 5.1(b). Lastly, as mentioned in Section 4.1, the skin must be flexible to allow for wing twisting while maintaining a degree of stiffness to prevent damages caused by debris or aerodynamic loads during flight. These two requirements make a flexible thermoplastic material a preferred choice. The skin shown in Fig. 5.1(c) is composed of Covestro Desmopan™ 790 thermoplastic polyurethane (TPU). TPU is known to be durable and can operate at a wide range of temperatures, making it a suitable material for the wing skin. The material parameters of TPU are obtained from the website of a manufacturer [12].

Further material selection for the different components of the wing is addressed in later sections of this work with the goal being reduction of weight weight and increase flexibility to controlled twist while maintaining significant strength and stiffness against unwanted deformations.

| **Material** | **Elastic modulus [GPa]** | **Poisson's ratio** | **Strength [MPa]** | **Mass density [kg/m$^3$]** |
|---|---|---|---|---|
| Al 6061-T6, Fig. 5.1(a) | 68.9 | 0.30 | 276.0 | 2700.0 |
| Grade 5 Ti, Fig. 5.1(b) | 113.8 | 0.33 | 880.0 | 4430.0 |
| Desmopan 790 TPU, Fig. 5.1(c) | 0.1 | 0.48 | 54.0 | 1210.0 |

Table 5.2: Material parameters for topological design parameters DOE.

The remaining figures in this section include the Pareto front in Fig. 5.2 and contour plots in Figs. 5.3–5.7 showing the effects of varying numbers of cells $n_c$ and the numbers of wire sets $n_w$ on $\Phi$, $m_s$, and $\sigma_{VM}$ of the different material groups, respectively. The Pareto front

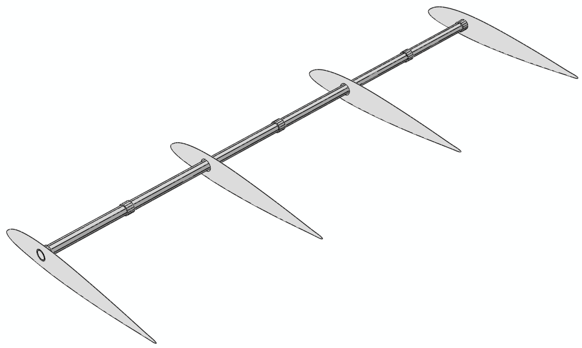

(a) Al 6061-T6.

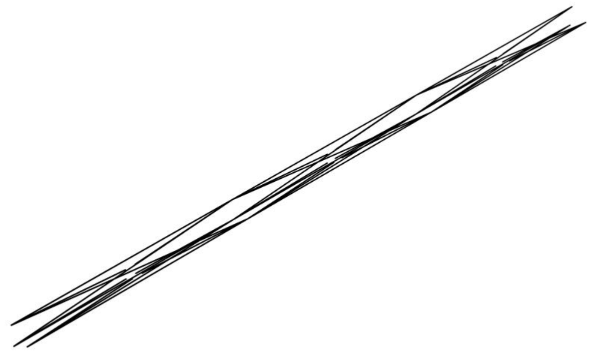

(b) Grade 5 Ti.

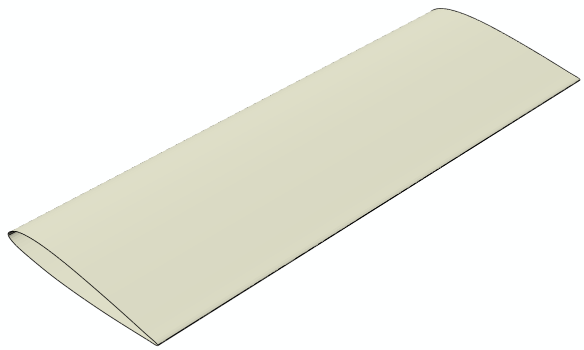

(c) Desmopan 790 TPU.

Figure 5.1: Components of the wing displayed according to their material assignment. Reprinted from [46].

in Fig. 5.2 is generated in the $\Phi$ and $m_s$ space, where high values of twist angle $\Phi$ and low values of structural mass $m_s$ are preferred. Using the selection criterion defined by Eq. (4.2), the design having eight cells and four wire sets, which delivered a value of $\eta = 5.93°/\text{kg}$, corresponds to the most favorable design.

The subsequent figures are contour plots of the response parameters. The most favorable design point based on the criterion of Eq. (4.2) is marked on each contour as a diamond for reference. Figure 5.3, which is the contour plot of total twist angle ($\Phi$) in terms of $n_w$ and $n_c$, shows that as $n_c$ increases, $\Phi$ also increases. It is observed that $n_w$ also has an impact on the total twist angle. However, the influence from varying this parameter on $\Phi$ is much less when compared to the influence from changing $n_c$.

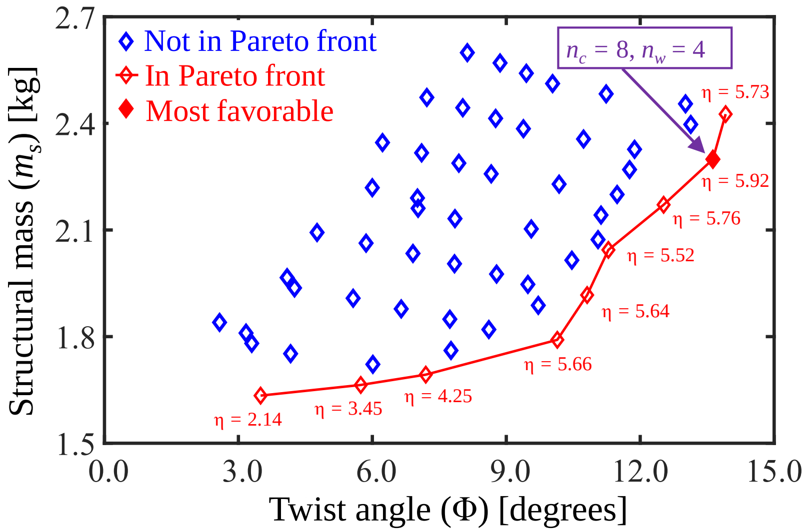


Figure 5.2: Response parameters of the simulated designs in the structural mass ($m_s$) vs. twist angle ($\Phi$) space. The Pareto front is indicated. The most favorable design is selected according to the *twist angle per unit mass* criterion ($\eta$) defined in Eq. (4.2). The values of $\eta$ for the designs in the Pareto front are also indicated. Results of topology parameter DOE. Reprinted from [46].

The complexity of the wing increases with the number of sections and wire sets which in turn also increases the structural mass $m_s$. Figure 5.4 shows the $m_s$ contour plot which reflects an increase as $n_c$ and $n_w$ increase. It is observed that varying the number of cells $n_c$, had a much larger impact on $m_s$. This is understandable since adding more cells requires additional ribs and rings whereas adding more wire sets only introduces additional wires.

Using the criterion of Eq. (4.2), Fig. 5.5 is generated showing $\eta$ for the different combinations of $n_c$ and $n_w$. It is observed that varying $n_w$ has a larger impact on this criterion.

Per Table 5.2, material failure typically occurs at 276.0 MPa for 6061-T6 aluminum alloy, which is reduced to 184.0 MPa when a 1.5 safety factor is applied. It is observed that in every design iteration, the failure von Mises stress is reached at the interface between the rib at the tip and the spar, both of which are aluminum components. For this reason, the 6061-T6 aluminum strength constrained the wing from twisting further in this design study. A contour plot of maximum von Mises in the aluminum components (ribs, rings, and spar)

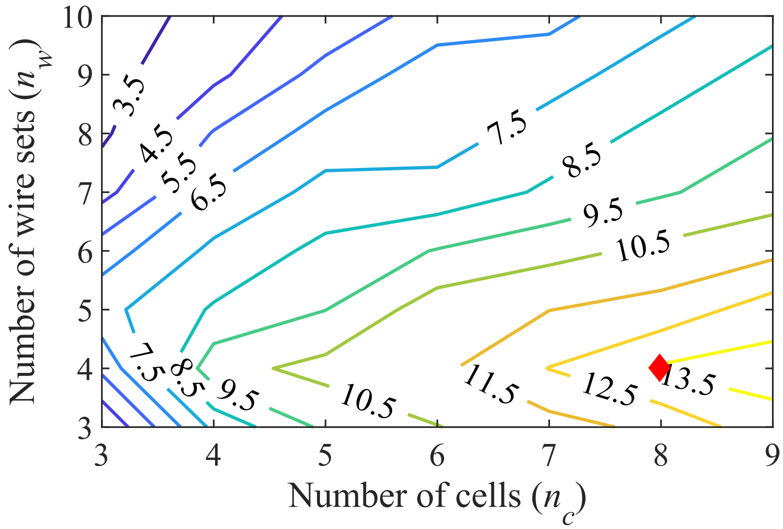


Figure 5.3: Contour plot of twist angle ($\Phi$) [degrees]. The most favorable design according to the criterion defined in Eq. (4.2) is indicated. Results of topology parameter DOE. Reprinted from [46].

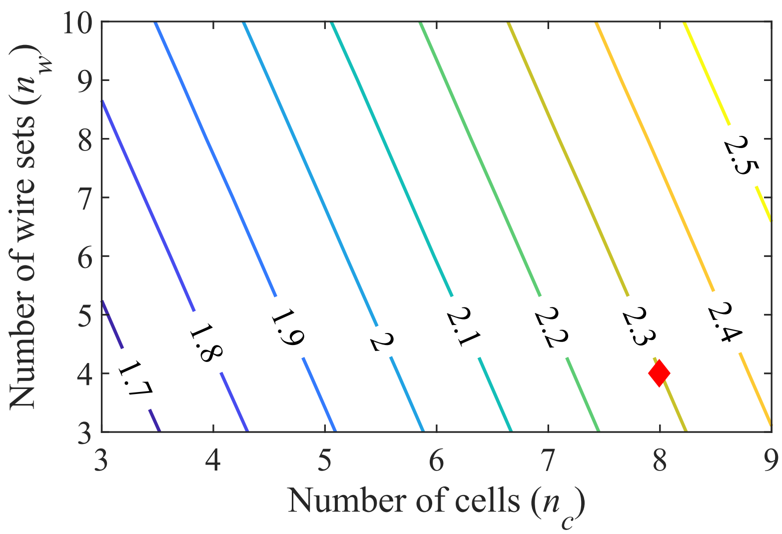


Figure 5.4: Contour plot of structural mass ($m_s$) [kg]. The most favorable design according to the criterion defined in Eq. (4.2) is indicated. Results of topology parameter DOE. Reprinted from [46].

is not presented herein since it would show a value of 184 MPa (the failure value) at all the design points. For the most favorable design, the location of maximum stress specifically occurred where the rib at the tip contacts the edge of the spar cross-section as shown in Fig. 5.6. A similar stress distribution is observed in all the other studied designs. Further

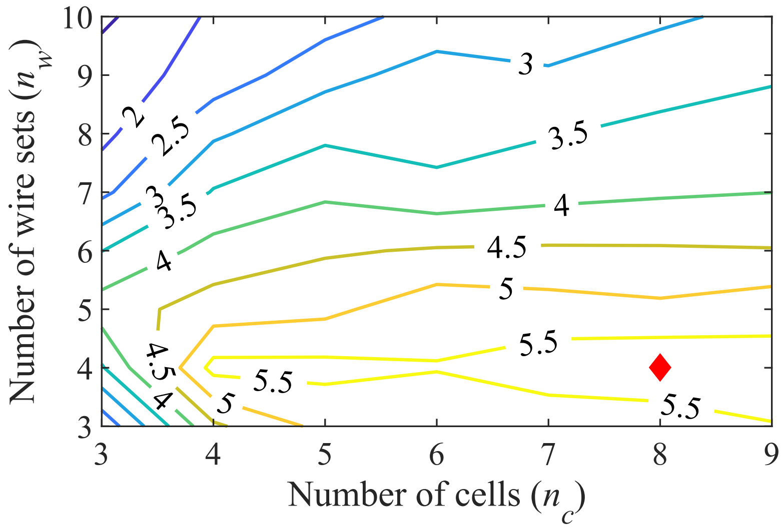


Figure 5.5: Contour plot of total twist angle per unit structural mass ($\eta$) [°/kg]. The most favorable design according to the criterion defined in Eq. (4.2) is indicated. Results of topology parameter DOE. Reprinted from [46].

work needs to be conducted to effectively alleviate stress concentrations that may arise at detailed features of the wing during morphing.

The contour plots in Fig. 5.7 depict the maximum stresses experienced in the other two material groups, the titanium wires and TPU skin for all design iteration. Figure 5.7(a) is the contour plot of the maximum stress levels experienced by the wires. As predicted, increasing the number of wire sets has an inverse effect on the maximum stress levels. For Grade 5 titanium wires, yielding occurs at 880.0 MPa, after adjusting for a 1.5 safety factor, the constraint comes down to approximately 586.7 MPa which is well above the stress levels shown. The longitudinal wires in the cell at the wing tip experienced the highest stresses. Finally, Fig. 5.7(b) illustrates the maximum von Mises stresses within the skin. It confirms the fact that every design iteration delivered a stress level that is well below the strength of TPU.

A parameter of interest in the practical application of the presented torsional wing is the energy required to perform the twisting motion. Although the exact power or energy re-

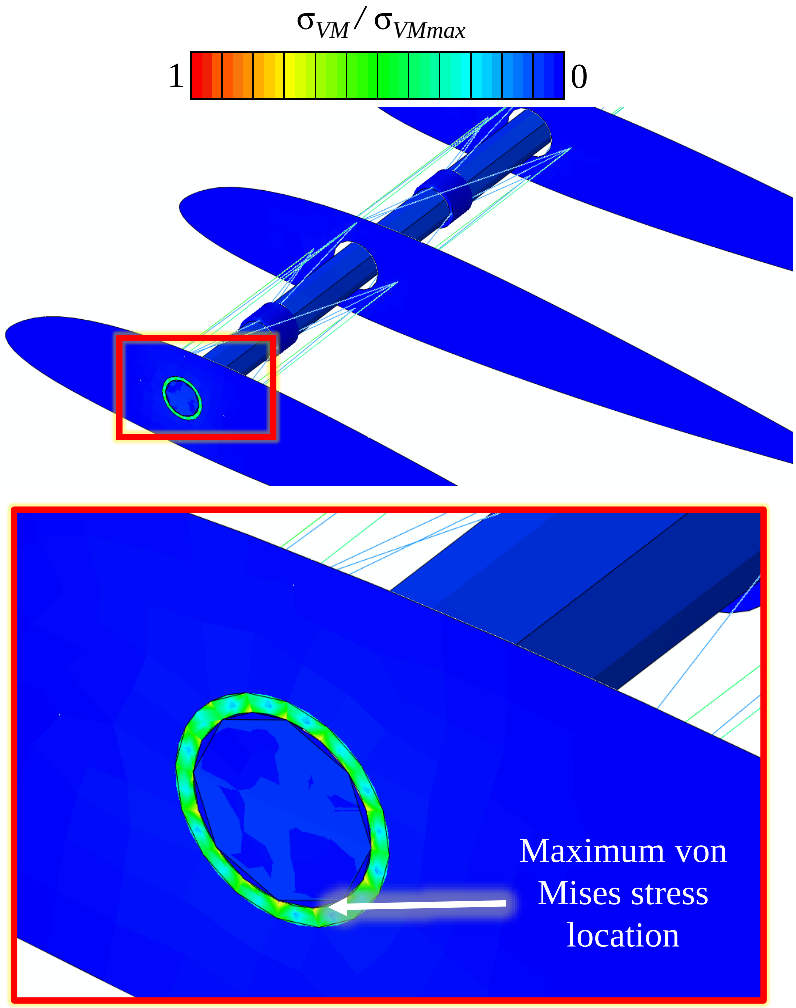


Figure 5.6: Contour plot of von Mises stress $\sigma_{VM}$ normalized by its maximum value $\sigma_{VMmax}$ for the most favorable design. The location of maximum von Mises stress is at the connection between the rib at the tip and the edge of the spar cross-section. Results of topology parameter DOE. Reprinted from [46].

quired to twist the wing can only be calculated once the specific actuation mechanism has been determined (*e.g.*, electrical motors contracting the actuator wires by pulling them or actuator wires formed by shape memory alloys), the total energy of the wing after twisting to its maximum allowable angle minus its total energy before twisting is reported herein as a preliminary indicator. The total energy values of the wing before and after torsional deformation are retrieved from the `Abaqus CAE` history output variable `ETOTAL`. The reported energy values would not exactly correspond to the actual energy required to twist the wing, as motors or shape memory alloys introduce energy inefficiencies, but it is expected that the actual energy required will be proportional to these reported values. Figure 5.8 provides the contour plot of total energy of the wing after twisting to its maximum allowable angle minus its total energy before twisting. Low values are obtained since the majority of the deformation of the wing during twisting occurs at the skin, which is composed of a compliant polymeric material. It is observed that the most favorable design based on twist angle per unit mass ($\eta$) is located in the region with the highest energy values.

Figure 5.9 presents the $y$-axis displacement plots at the initial configuration, 50% twist, and 100% twist of the wing with eight cells and four wire sets–the most favorable design. These figures confirmed the tensegrity-based twisting wing concept, showing a twisted wing with a continuous external surface. It is observed from the simulations that small wrinkles appear on the skin surface as the wing twists, which are typically unfavorable in morphing wings.

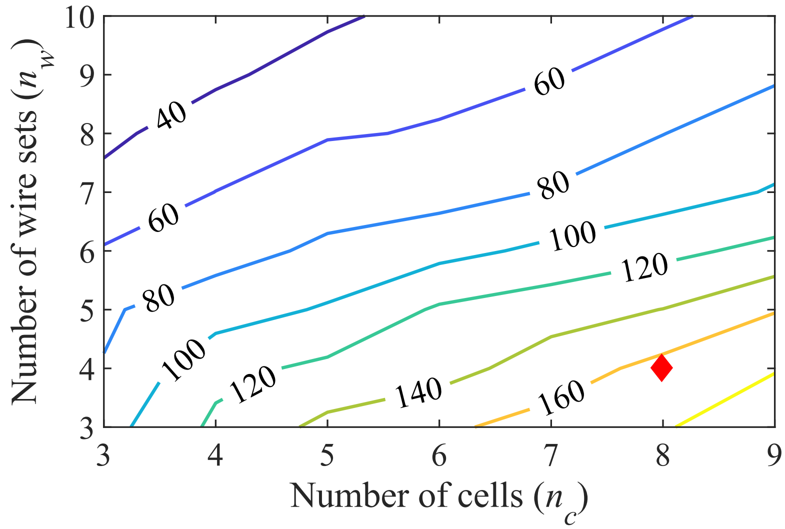


(a) Maximum von Mises stress in the wire network [MPa]. Maximum allowable value considering safety factor: 586.6 MPa.

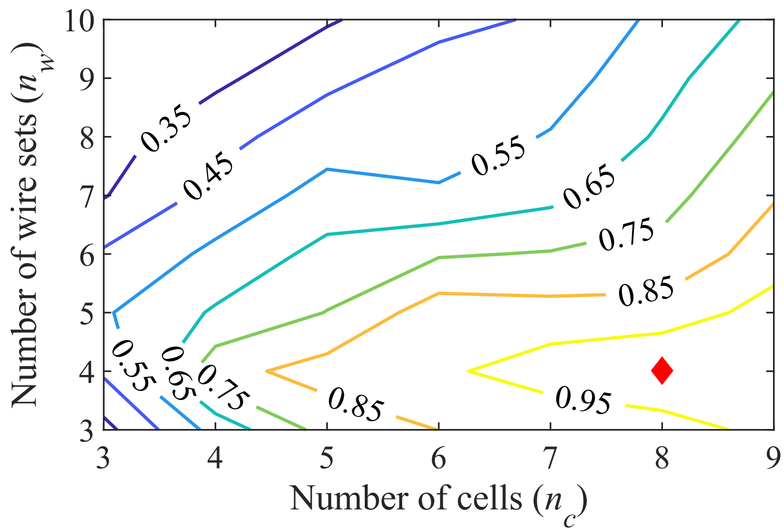


(b) Maximum von Mises stress in the skin [MPa]. Maximum allowable value considering safety factor: 36.0 MPa. Results of topology parameter DOE. Reprinted from [46].

Figure 5.7: Contour plots of maximum von Mises stress obtained for the wire and skin components at the onset of material failure. The component that reached the failure von Mises stress in all simulations is the rib located at the tip of the wing. The most favorable design according to the criterion defined in Eq. (4.2) is indicated. Results of topology parameter DOE. Reprinted from [46].

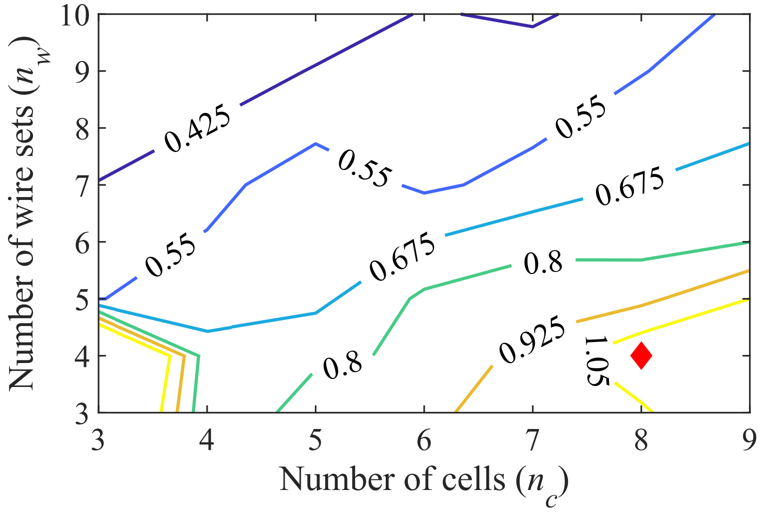


Figure 5.8: Contour plot of total energy of the wing after twisting to its maximum allowable angle minus its total energy before twisting. The reported values have units of Joules. The most favorable design according to the criterion defined in Eq. (4.2) is indicated. Results of topology parameter DOE. Reprinted from [46].

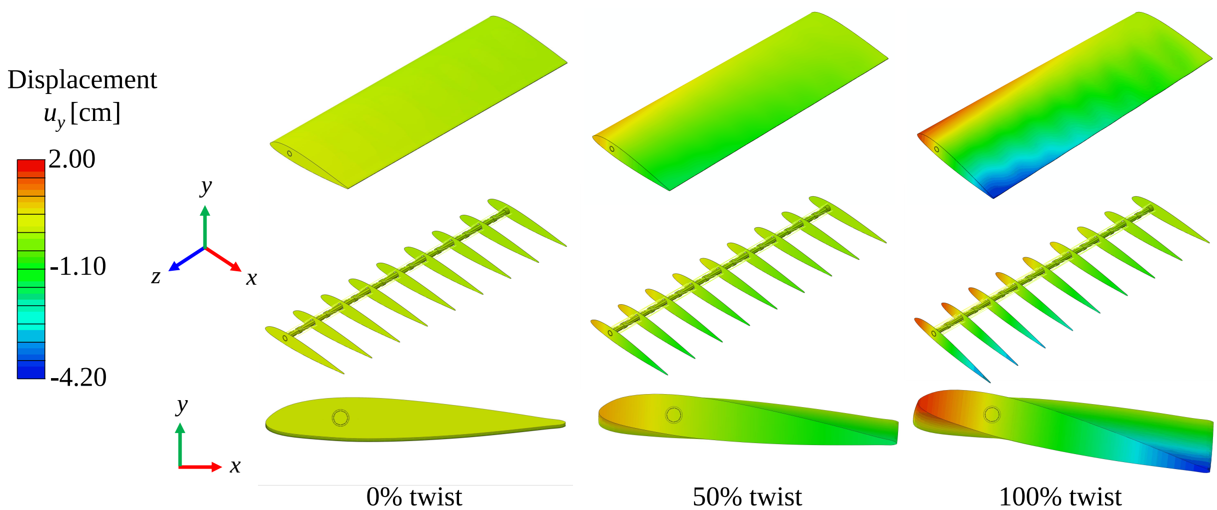


Figure 5.9: Most favorable tensegrity wing design of topological parameter DOE according to the criterion defined in Eq. (4.2) at different configurations during twisting. The internal mechanism of the wing is formed by eight cells and four wire sets ($n_c = 8$, $n_w = 4$). Maximum achievable twist angle $\Phi = 13.6°$, structural mass $m_s = 2.3kg$, and $\eta = 5.93°/kg$. Results of topology parameter DOE. Reprinted from [46].

## 5.2 Case Study on Cell Span Distribution

The effect of varying the cell spacing on the maximum achievable twist angle is studied in this section. Wing designs with different cell span distributions are simulated and their maximum achievable twist angles before failure are reported. A linear distribution of the length of the cells along the span direction between tip and root is assumed. This linear distribution is defined by a single parameter denoted as $\Gamma$ which represents the ratio of the tip cell span to the root cell span. If $\Gamma < 1$, the cell span increases towards the root; if $\Gamma > 1$, the cell span increases towards the tip; and if $\Gamma = 1$, the cell span is uniform. Figure 5.10 shows the seven cases studied. All other size and topological parameters of the studied wings correspond to those of the most favorable design found in the design of experiments study and shown in Fig. 5.9. Thus, the case where $\Gamma = 1$ corresponds to that shown in Fig. 5.9.

The difference between maximum achievable twist angle $\Phi$ and the reference value $\Phi_{ref}$ (assumed to be that of the wing with a uniform cell span distribution, $\Gamma = 1$) vs. $\Gamma$ is shown in Fig. 5.11. It is observed that the wing with uniform cell distribution ($\Gamma = 1$) provides the largest achievable twist angle, and that increasing the cell span towards either the tip or the root directions decreases the achievable twist angle. Hence, these results suggest that uniform cell spacing is the most favorable distribution to achieve the largest twist angles. It is also observed that the difference in twist angles between all the simulated cases is very small, where all of them are within less than 1.1% difference from the reference distribution.

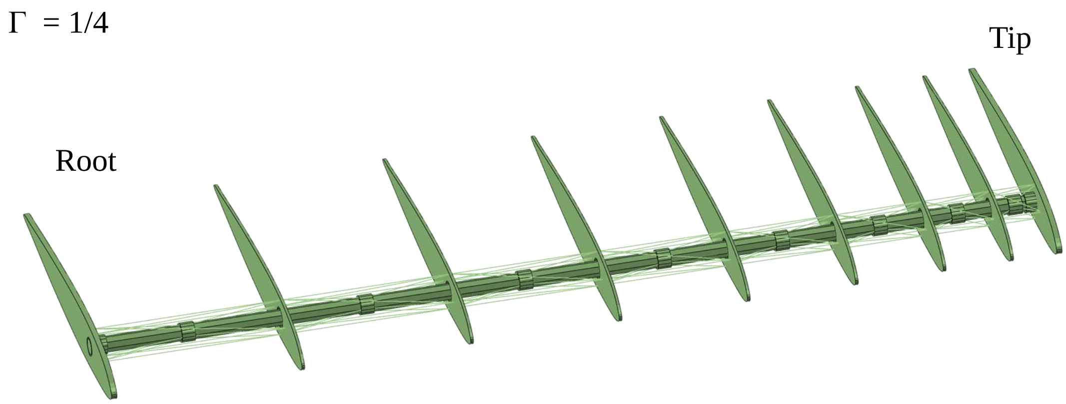


(a)

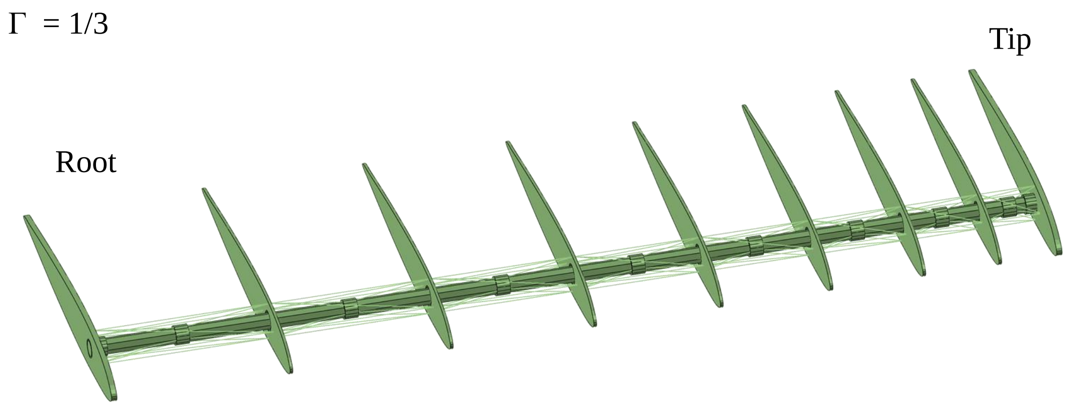


(b)

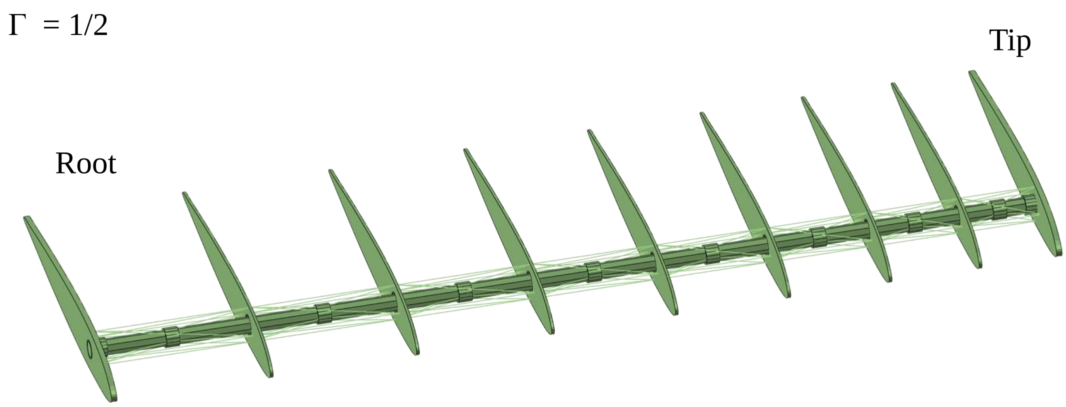


(c)

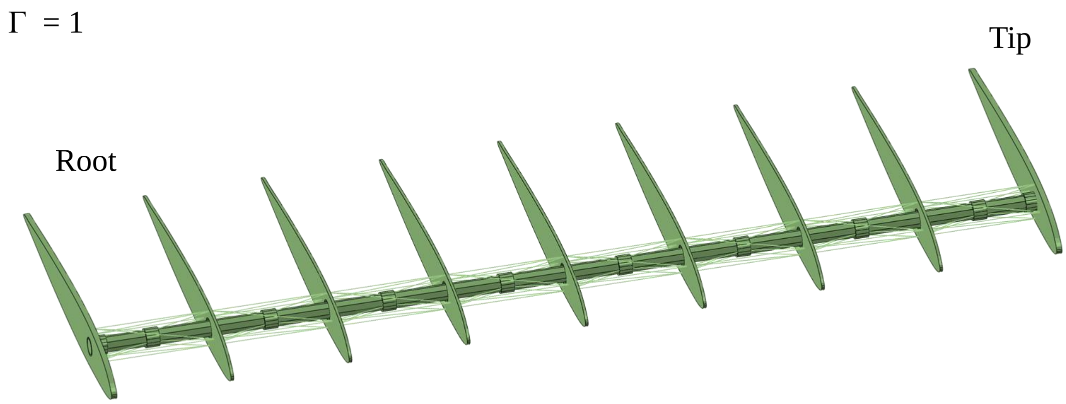


(d)

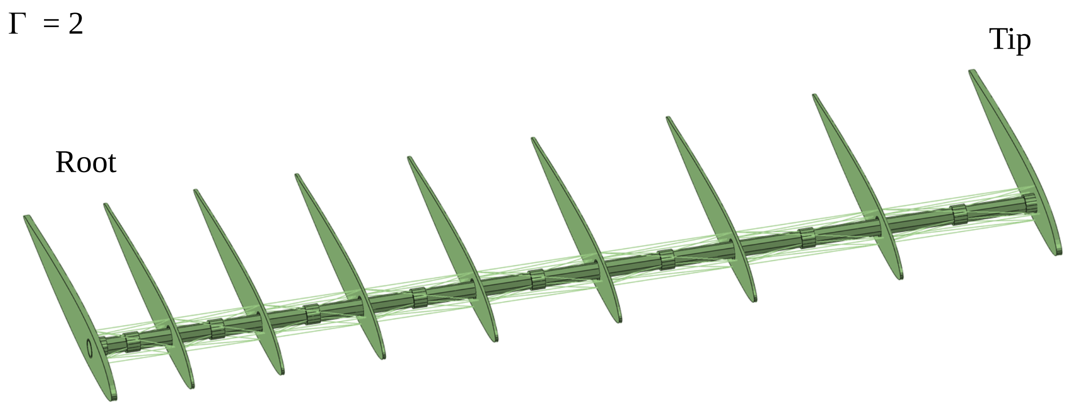


(e)

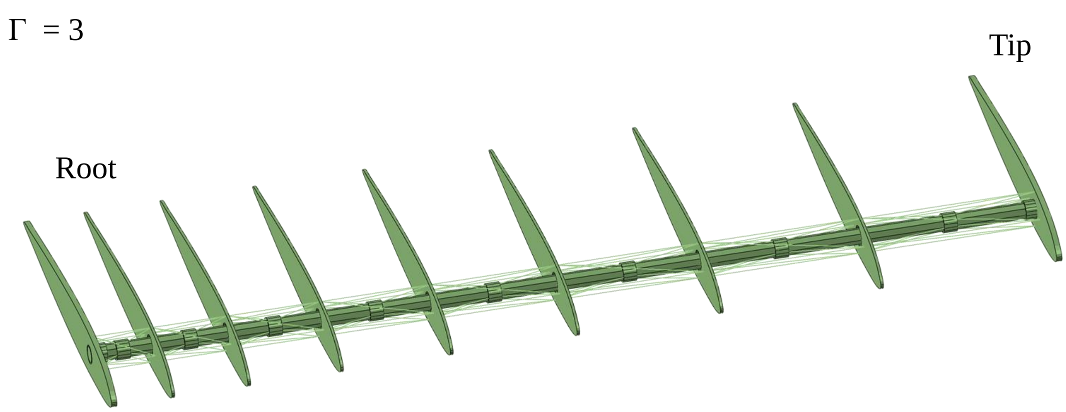


(f)

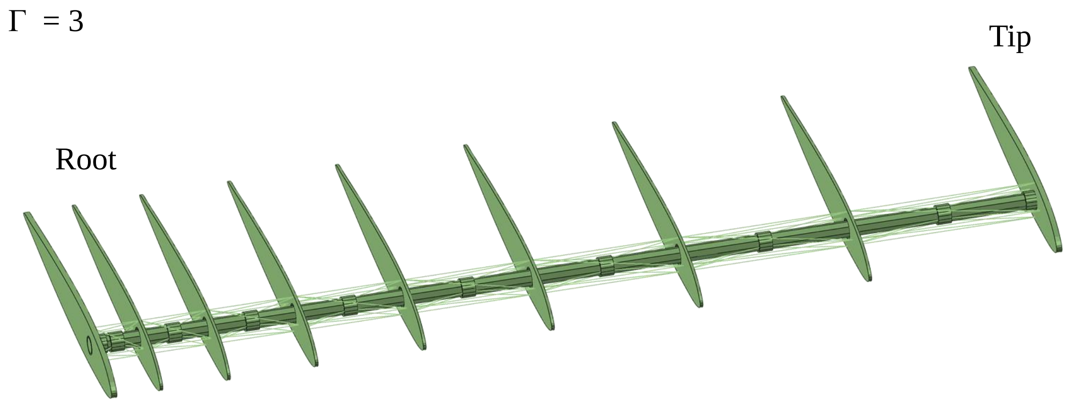


(g)

Figure 5.10: Schematics showing the internal structure of wings with different values of ratio of tip cell span to root cell span (Γ). Case study of topology parameter DOE. Adapted from [46].

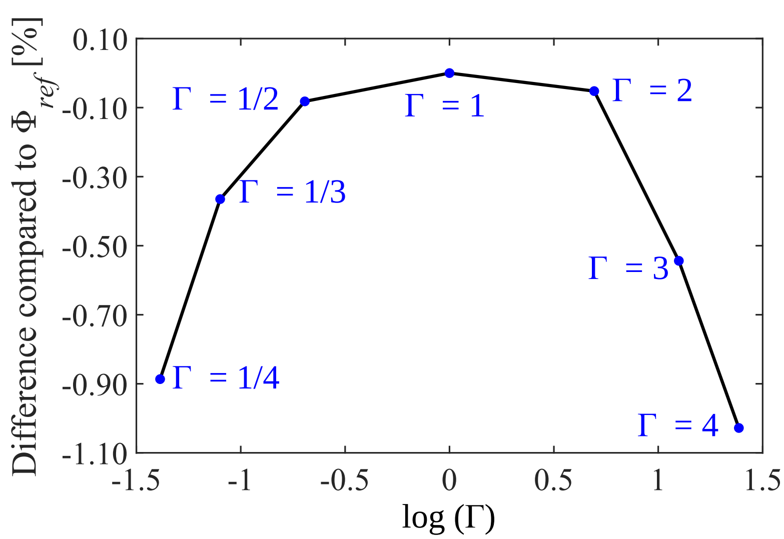


Figure 5.11: Difference between maximum achievable twist angle Φ and the reference value $\Phi_{ref}$ (for $\Gamma = 1$) vs. Γ. The provided data points correspond to those of the wings shown in Fig. 5.10. Results of topology parameter DOE case study. Reprinted from [46].

## 5.3 Critical Design Parameters Impact

[3]The work presented in this section was conducted to provide an evaluation on the effect of varying critical design parameters and determine the primary performance drivers. The `MATLAB` script varies the design parameters such as the number of cells $n_c$ and wire sets $n_w$, the thickness of the skin $t_s$ and ribs $t_r$, spar radius $r_s$, the wire diameters $d_{act}$ and $d_{pass}$, and the material types of three primary component groups. Since the total number of design variables was ten and each had five initial options, testing and evaluating every possible design iterations is unrealistic. The Taguchi method was developed to evaluate a representative set of combinations for experimentation, it is chosen to generate the initial design space to reduce the computation time. A Taguchi orthogonal array is created based on the algorithm outlined in [72]. With ten design variables and five levels for each variable, the algorithm generates an orthogonal array of 125 different designs. The Taguchi method ensured that each option of each parameter is tested in ten different combinations.

Table 5.3 lists out all the design variables and their respective design values and choices. The options for $n_c$ and $n_w$ were selected based on previous design study detailed in Ref. [47]. The standard sheet thicknesses of the materials employed to make the skin serve as reference for the assumed thickness values of this component. The spar radius and the thickness of the ribs are assumed values. Finally, market availability dictates the diameters for the longitudinal, stabilizer, and actuator wires.

As stated in Section 4.1, components are divided into categories based on their function within the wing structure. The first group includes the ribs, spar, and stabilizer rings. These components are assumed to be made from metal sheets or bars. Aluminum alloys

[3]Portions of this section are reprinted or adapted from [Nguyen K. Pham and Edwin A. Peraza Hernandez, 2021, "Modeling and design exploration of a morphing wing enabled by a twisting tensegrity mechanism," Proceedings of the 2021 AIAA SciTech Forum and Exposition, AIAA 2021-0099, virtual conference. https://doi.org/10.2514/6.2021-0099]. Figures are reprinted by permission of the American Institute of Aeronautics and Astronautics, Inc.

| **Parameter** | **Studied values** | | | | |
|---|---|---|---|---|---|
| Taguchi array value | (1) | (2) | (3) | (4) | (5) |
| Number of cells ($n_c$) | 4 | 5 | 6 | 7 | 8 |
| Number of wire sets ($n_w$) | 3 | 4 | 6 | 8 | 10 |
| Skin thickness ($t_s$) [mm] | 1.25 | 1.50 | 1.75 | 2.00 | 2.25 |
| Spar radius ($r_s$) [mm] | 3.00 | 4.00 | 5.00 | 6.00 | 7.00 |
| Rib thickness ($t_r$) [mm] | 3.00 | 4.00 | 5.00 | 8.00 | 10.00 |
| Diameter of actuator wires ($d_{act}$) [mm] | 0.813 | 1.016 | 1.829 | 2.337 | 3.251 |
| Diameter of passive wires (longitudinal and stabilizer wires) ($d_{pass}$) [mm] | 0.813 | 1.016 | 1.829 | 2.337 | 3.251 |
| Material for ribs, spar, and rings | 7075-T73 Al | 6061-T6 Al | 2024-T3 Al | Ti-6Al-4V | 3003-H14 Al |
| Material for skin | Desmopan 790 TPU | Desmopan 9650DU TPU | Teflon PTFE | RTP700A LDPE | 2004CX3 LDPE |
| Material for wires | Gr. 5 Ti | Gr. 2 Ti | CRES 304 | CRES 410 | Al 1100-O |

Table 5.3: Critical design parameters and their studied values.

and Titantium alloys, both commonly used within the aerospace industry for structural components are employed. The second category of material covers the external skin. In this study, thermoplastic polyurethane (TPU), polytetrafluoroethylene (PTFE), and low-density polyethylene (LDPE), are deemed as possible candidates. Finally, for simplicity, the wires are grouped into one category and are assumed to be made from the same material. These members are the primary load-bearing and actuating members of the tensegrity structure, and therefore, need to be made from metal alloys. Two grades of Titanium alloys, two grades of corrosion resistant steel (CRES), and one aluminum alloy are considered in this design experiment. Table 5.4 summarizes the critical properties of the materials used in the simulations. These properties are obtained from the manufacturers of the materials and literature sources. Again, selecting the appropriate material for each component of the wing will be an area of concentration in future studies to maximize the structural strength-to-weight ratio and increase the tensegrity structural flexibility to controlled twist.

| Material | Tensile modulus [GPa] | Poisson's ratio | Strength [MPa] | Mass density [kg/m$^3$] |
|---|---|---|---|---|
| **Ribs, spar, and rings** | | | | |
| Al 7075-T73 | 72.0 | 0.33 | 435.0 | 2810.0 |
| Al 6061-T6 | 68.9 | 0.33 | 276.0 | 2700.0 |
| Al 2024-T3 | 73.1 | 0.33 | 345.0 | 2780.0 |
| Ti-6Al-4V | 114.0 | 0.33 | 1100.0 | 4430.0 |
| Al 3003-H14 | 68.9 | 0.33 | 145.0 | 2730.0 |
| **Skin** | | | | |
| Desmopan 790 TPU | 0.100 | 0.48 | 54.0 | 1210.0 |
| Desmopan 9650DU TPU | 0.340 | 0.48 | 58.0 | 1160.0 |
| Teflon PTFE | 0.400 | 0.46 | 41.4 | 2140.0 |
| RTP700A LDPE | 0.207 | 0.46 | 6.0 | 920.0 |
| 2004CX3 LDPE | 0.240 | 0.46 | 10.0 | 921.0 |
| **Wires** | | | | |
| Gr. 5 Ti | 113.8 | 0.34 | 880.0 | 4430.0 |
| Gr. 2 Ti | 102.0 | 0.37 | 340.0 | 4510.0 |
| CRES 304 | 193.0 | 0.29 | 215.0 | 8000.0 |
| CRES 410 | 200.0 | 0.27 | 1225.0 | 7800.0 |
| Al 1100-O | 68.9 | 0.33 | 34.0 | 2710.0 |

Table 5.4: Material properties of critical design parameters DOE.

At the end of the study, the results were tabulated and sorted to determine the main effect caused by changing one of the design parameters. Out of the 125 tested configurations, one design iteration delivered the highest value of the maximum twist angle ($\Phi$) of 19.5°and a mass of 1.805 kg without violating any of the stress constraints. This means, using Eq. (4.2), the calculated value of $\eta$ was 10.85°/kg. In both categories of $\Phi$ and $\eta$, this design iteration ranked highest and therefore was deemed as the most favorable.

Figures 5.12 - 5.21 are the main effect plots for the various design parameters. On each plot, the average values of the entire data sample were included for reference. The favorable design option is also identified on each plot. Figures 5.12 and 5.13 are main effect plots of the two variables $n_c$ and $n_w$ which are the number of cells and wire sets respectively. The structural mass plots clearly indicated that as these two variables increase, the wing becomes heavier.

On the other hand, for these two design variables, the twist angle plots were inconclusive and require further investigation in future work.

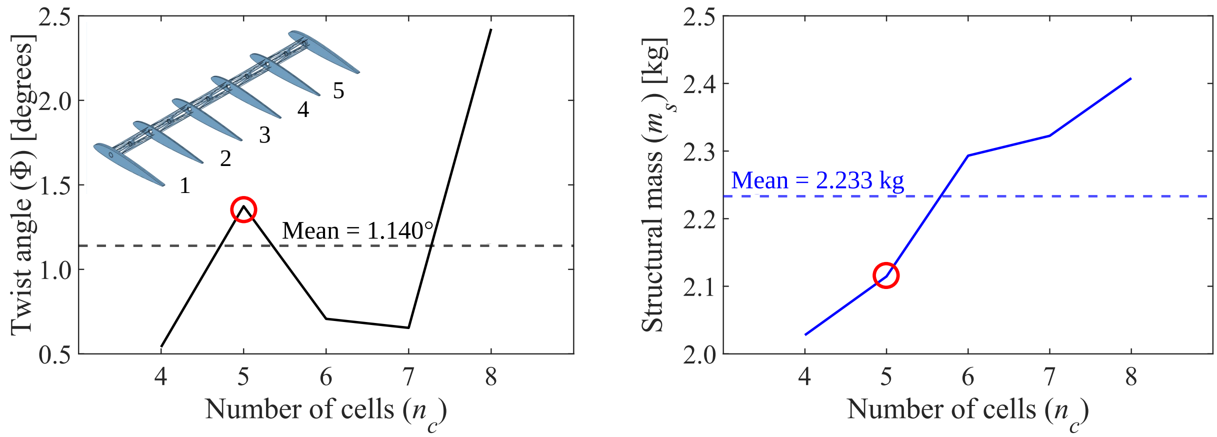


Figure 5.12: Main effect of varying number of cells ($n_c$) to twist angle ($\Phi$) and structural mass ($m_s$). The most favorable design option based on Eq. (4.2) is identified. Results of critical design parameters DOE. Reprinted from [48].

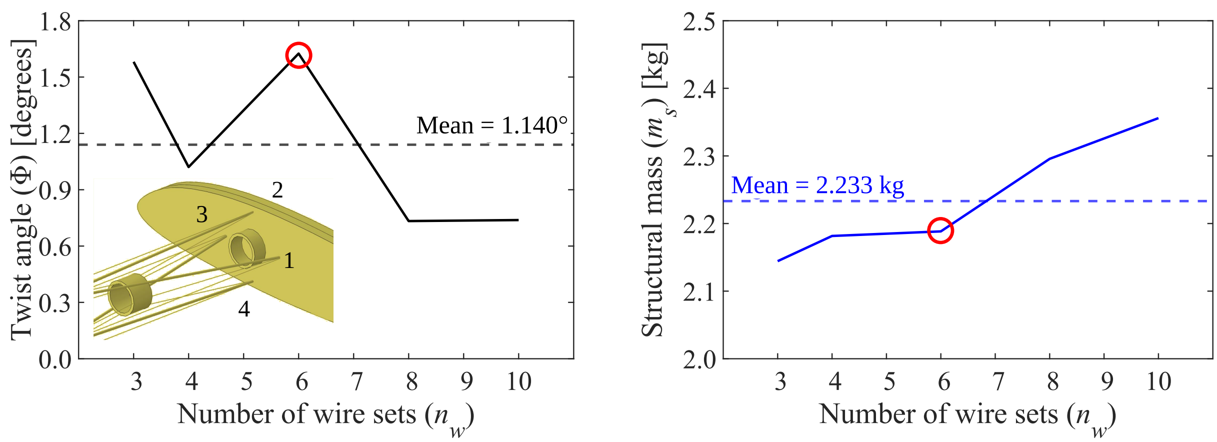


Figure 5.13: Main effect of varying number of wire sets ($n_w$) to twist angle ($\Phi$) and structural mass ($m_s$). The most favorable design option based on Eq. (4.2) is identified. Results of critical design parameters DOE. Reprinted from [48].

Figures 5.14 - 5.16 are main effect plots derived from changing the skin thickness ($t_s$), the spar radius ($r_s$), and rib thickness ($t_r$) in respective order. Once again, the structural mass plots reveal a proportional correlation between the values of these design parameters and $m_s$. The skin thickness main effect plot for twist angle featured a v-shape trendline. Since none of the designs caused the skin to go into a high-stress state, it was determined that 1.25

mm is the favorable value for the skin thickness. The spar radius main effect plot showed a proportional relation between $r_s$ and $\Phi$ meaning a larger spar will deliver a higher twist angle. Lastly, for the rib thickness ($t_r$), the twist angle plot was inconclusive and requires further study. It is reasonable to speculate that as the number of design variables decreases in more refined models, clearer trends can be determined.

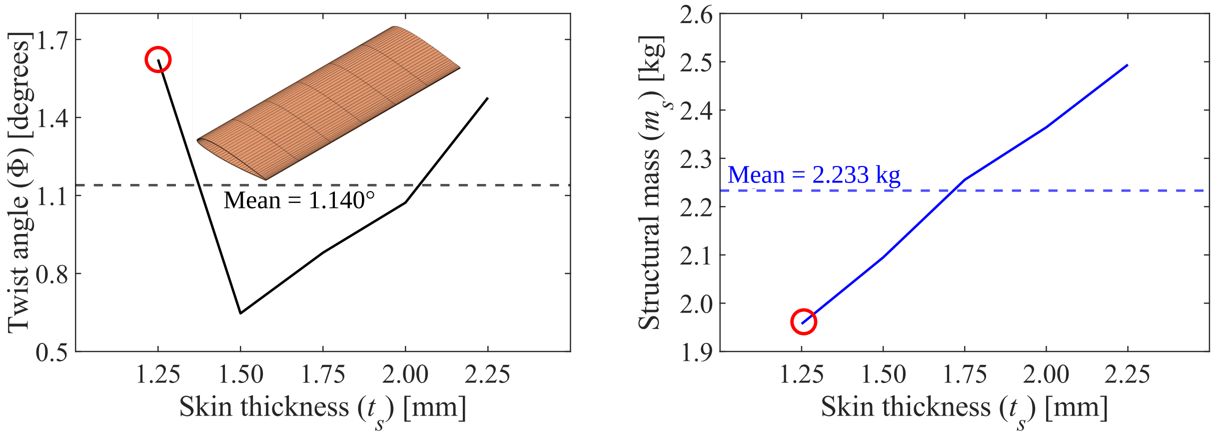


Figure 5.14: Main effects of varying skin thickness ($t_s$) to twist angle ($\Phi$) and structural mass ($m_s$). The most favorable design option based on Eq. (4.2) is identified. Results of critical design parameters DOE. Reprinted from [48].

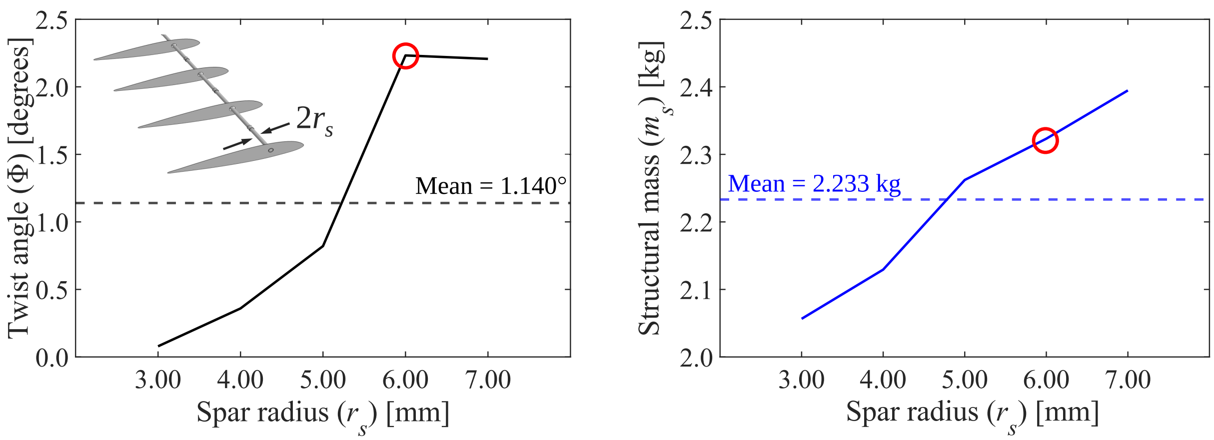


Figure 5.15: Main effects of varying spar radius ($r_s$) to twist angle ($\Phi$) and structural mass ($m_s$). The most favorable design option based on Eq. (4.2) is identified. Results of critical design parameters DOE. Reprinted from [48].

Figures 5.17 and 5.18 are the main effect plots resulting from the change in the diameters of the wires. The structural mass plots offer clear trends and show a proportional relation between the wire diameters and structural mass. The trend observed in the twist angle plot for the actuating wire diameter ($d_{act}$) shows a favorable relation between this variable and $\Phi$. Conversely, the passive wire diameter ($d_{pass}$) has an adverse relation with $\Phi$. It can be concluded from these two plots that to maximize the twist angle, the passive wires diameters must be much smaller than those of the actuator wires. This observation is confirmed in the most favorable design configuration where the values for $d_{pass}$ and $d_{act}$ are at opposite ends of the spectrum.

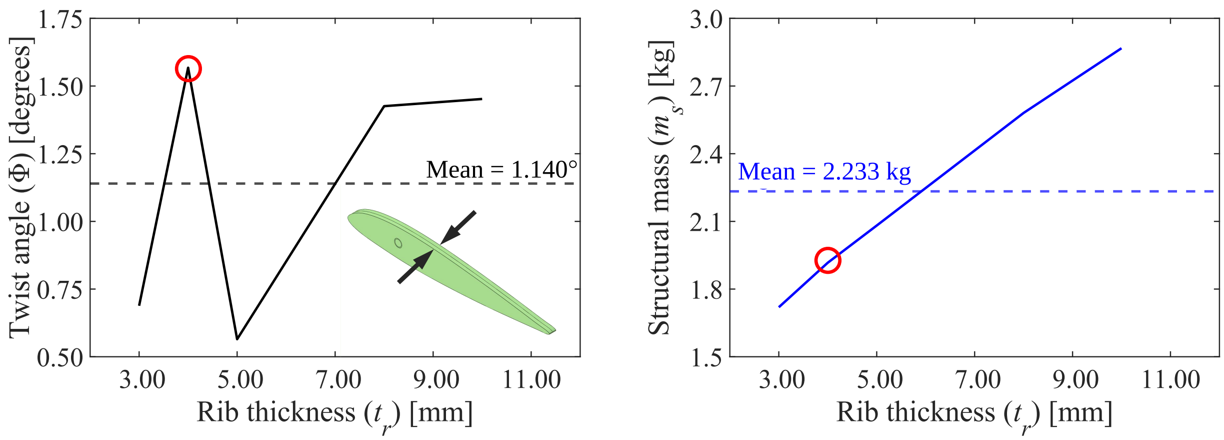


Figure 5.16: Main effects of varying rib thickness ($t_r$) to twist angle ($\Phi$) and structural mass ($m_s$). The most favorable design option based on Eq. (4.2) is identified. Results of critical design parameters DOE. Reprinted from [48].

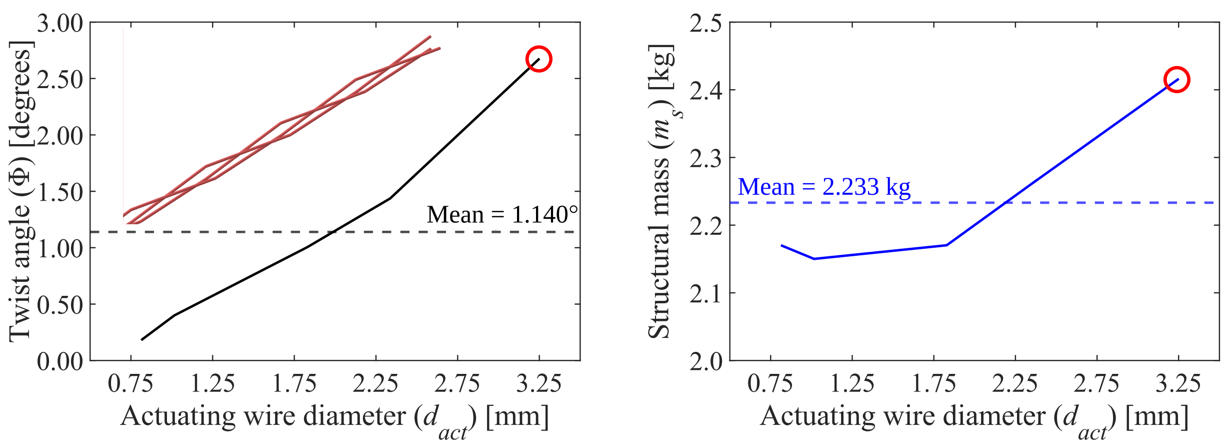


Figure 5.17: Main effects of varying actuator wire diameter ($d_{act}$) to twist angle ($\Phi$) and structural mass ($m_s$). The most favorable design option based on Eq. (4.2) is identified. Results of critical design parameters DOE. Reprinted from [48].

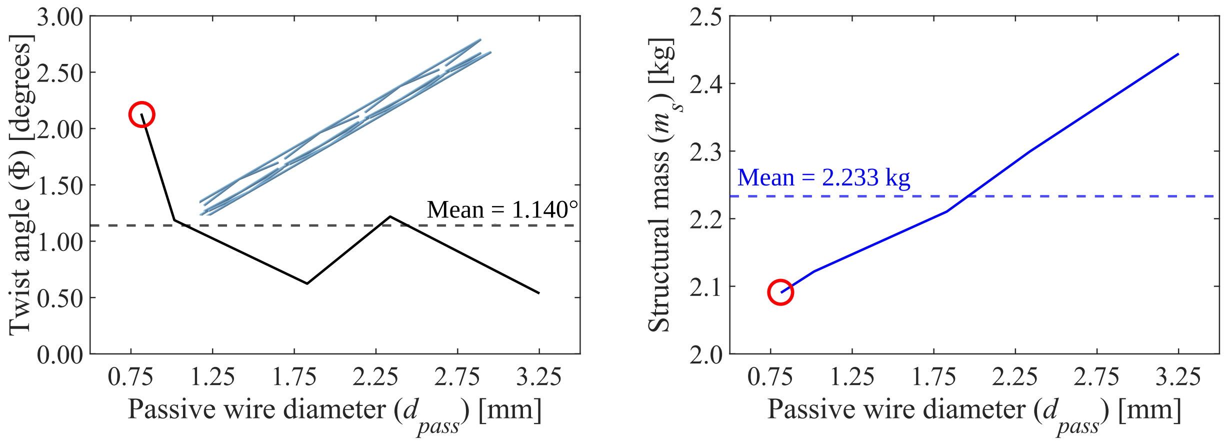


Figure 5.18: Main effects of varying passive (stabilizer and longitudinal) diameter ($d_{pass}$) to twist angle ($\Phi$) and structural mass ($m_s$). The most favorable design option based on Eq. (4.2) is identified. Results of critical design parameters DOE. Reprinted from [48].

Figures 5.19 - 5.21 are the main effect plots produced from changing the material for the components of the wing. Through these plots, the ideal materials for each component group are determined. In Fig. 5.19, although Ti-6Al-4V led to a significant increase in the structural mass ($m_s$), it delivered a superior maximum twist angle ($\Phi$) when compared against other materials. The improvement in ($\Phi$) outweighs the mass penalty and therefore makes Ti-6Al-4V the optimal material to make the ribs, spar, and stabilizer rings. As for the skin, from the plots of Fig. 5.20, 2004CX3 LDPE, was determined to be the material of choice. Even though 2004CX3 LDPE was only second highest in producing the averaged maximum value of $\Phi$, it offered a dramatic drop for the structural mass when compared to Desmopan 790 TPU–which had the highest averaged $\Phi$ value. Lastly, through Fig. 5.21, Gr.5 Ti alloy was chosen as the most favorable material for the wires. The choice was made based on the fact that it delivered the highest twist angle ($\Phi$) with the second lowest structural mass ($m_s$). Furthermore, titanium alloys, with their impressively high strength-to-weight ratio makes them the ideal candidate to produce the wires which are the primary load bearing and actuating members of the structure. As previously mentioned, the materials used in this study only offered a baseline for the design to start from. The material selection for each component will be further studied and optimized in future work to maximize the overall performance and improve the economic aspect of the tensegrity wing design.

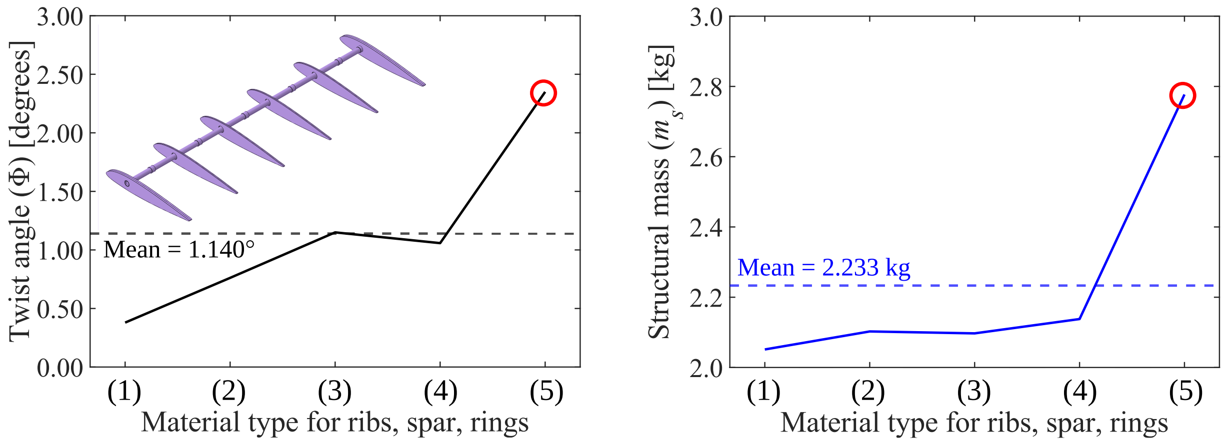


Figure 5.19: Main effects of changing material for the rings, ribs, and spar to twist angle ($\Phi$) and structural mass ($m_s$). The five options are (1) Al 3003-H14 (2) Al 2024-T3 (3) Al 6061-T6 (4) Al 7075-T73 (5) Ti-6Al4V. The most favorable design option based on Eq. (4.2) is identified. Results of critical design parameters DOE. Reprinted from [48].

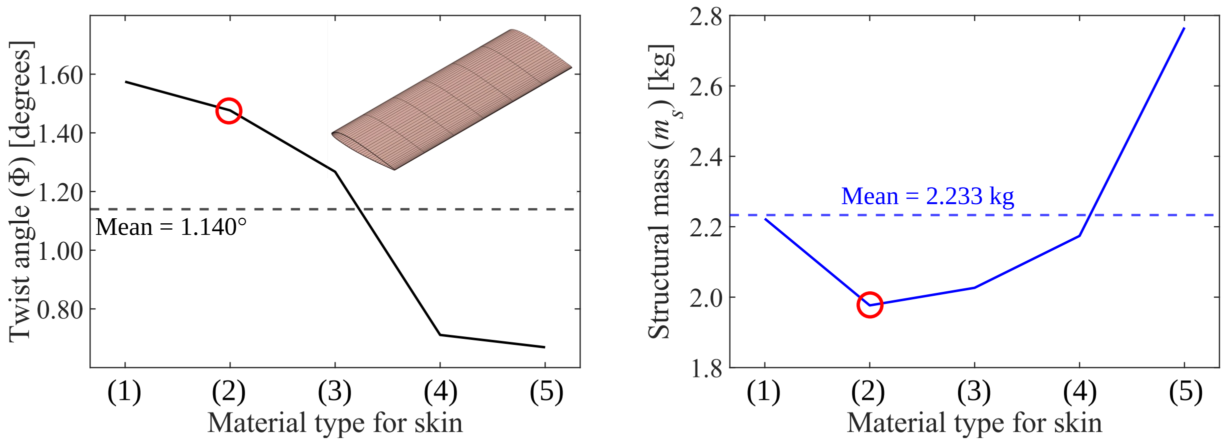


Figure 5.20: Main effects of changing material for the skin to twist angle ($\Phi$) and structural mass ($m_s$). The five options are (1) Desmopan 790 TPU (2) 2004CX3 LDPE (3) RTP700A LDPE (4) Desmopan 9650DU TPU (5) Teflon PTFE. The most favorable design option based on Eq. (4.2) is identified. Results of critical design parameters DOE. Reprinted from [48].

Figure 5.22 provides displacement contours of the most favorable design at the initial configuration, 50% deformation, and 100% deformation configurations. Table 5.5 offers a summary of the design parameters and characteristics of this design configuration.

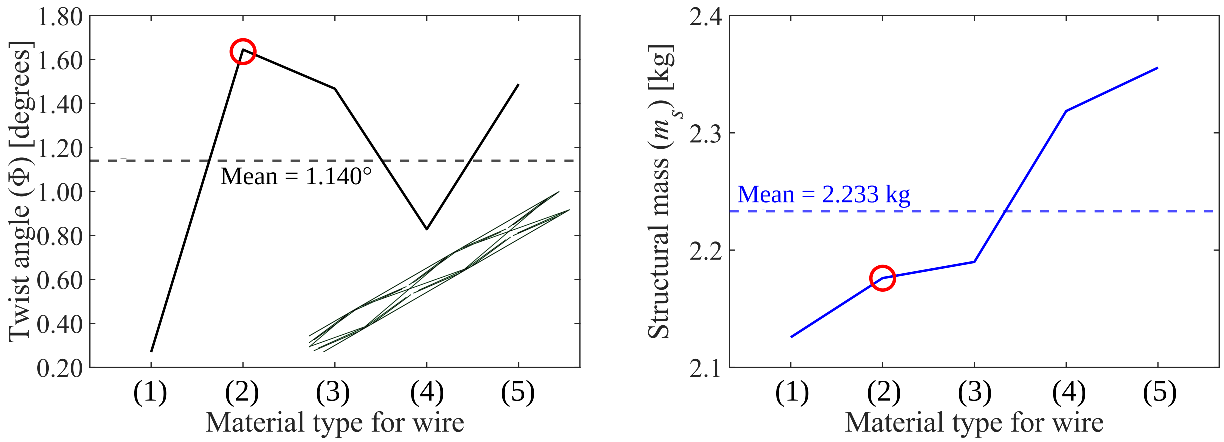


Figure 5.21: Main effects of changing material for the wires to twist angle (Φ) and structural mass ($m_s$). The five options are (1) Al 1100-O (2) Gr.5 Ti (3) Gr.2 Ti (4) CRES 304 (5) CRES 410. The most favorable design option based on Eq. (4.2) is identified. Results of critical design parameters DOE. Reprinted from [48].

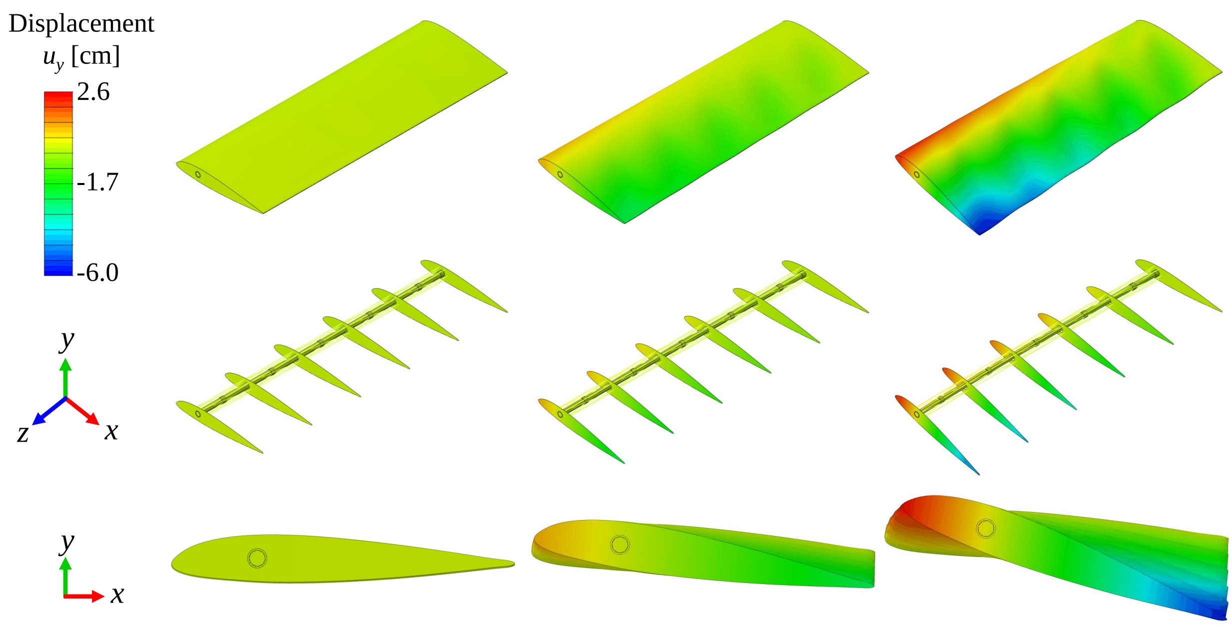


Figure 5.22: Deformation contours of the most favorable design in the critical design parameters DOE according to the criterion defined in Eq. (4.2) at different configurations during twisting. The parameters of this design are listed in Table. 5.5. Results of critical design parameters DOE. Reprinted from [48].

From the displacement contours presented in Section 5.1 and 5.3, it is observed that the skin experienced some warpage and wrinkling during the twisting motion, especially toward the wing tip where there is a greater amount of displacement. This phenomenon can lead to

| **Parameter** | **Value [unit]** |
|---|---|
| Number of cells ($n_c$) | 5 |
| Number of wire sets ($n_w$) | 6 |
| Skin thickness ($t_s$) | 1.25 [mm] |
| Spar radius ($r_s$) | 6.00 [mm] |
| Thickness of ribs ($t_r$) | 4.00 [mm] |
| Diameter of actuator wires ($d_{act}$) | 3.25 [mm] |
| Diameter of passive wires (longitudinal and stabilizer wires) ($d_{pass}$) | 0.81 [mm] |
| Material for ribs, spar, and rings | Ti-6Al-4V |
| Material for skin | 2004CX3 LDPE |
| Material for wires | Gr. 5 Ti |
| Total twist angle ($\Phi$) | 19.586° |
| Structural mass ($m_s$) | 1.805 [kg] |
| Twist angle per unit mass ($\eta$) | 10.85 [°/kg] |

Table 5.5: Parameters of the most favorable design of critical design parameters DOE.

flow disturbance and increase drag, which is highly undesirable. Utilization of pre-strained polymer sheets or anisotropic composites with different stiffnesses depending on directions have previously been studied and demonstrated their viability in resolving this issue [29, 68]. Both concepts will be included in future optimization study as the design matures. Furthermore, a trade-off study needs to be conducted to determine an optimal skin design that offers both stiffness and flexibility.

# Chapter 6

# Evaluation of Shape Memory Alloys as Means of Actuation

[1]This chapter presents an introduction to shape memory alloys (SMAs) and provides an evaluation of how well it performs as the primary means of actuation behind the tensegrity torsional mechanism. Section 6.1 describes SMAs, the shape memory effect (SME), and the underlying physics that allow them to possess such property. Section 6.3 lays out the DOE that was conducted to evaluate its performance.

## 6.1 Overview of Shape Memory Alloys (SMAs)

Shape memory alloys (SMAs) are alloys that can recover plastic strain completely when they are heated above a certain temperature [64]. SMAs often exhibit two attractive properties known as the shape memory effect (SME) and pseudoelasticity. SME has been observed in Au-Cd, In-Tl, Cu-Al-Ni, and Ni-Ti alloy and is primarily attributed to the martensitic

[1]Portions of this section are reprinted or adapted from [22].

transformation and complete shape recovery is often associated with the detwinning process under constant stress condition [24, 64]. Utilization of SME have allowed engineers to design devices such as mechanical actuators as shown in Ref. [56] or self-extending stents as shown in Ref. [41]. On the other hand, pseudoelasticity is associated with stress-induced phase transformation from austenite to detwinned martensite during loading and subsequent reversal to the austenite phase upon unloading [24]. The pseudoelastic property of SMAs have been used to design semi-active suspension systems [73] and vibration dampers in buildings or bridges [63].

In this work, SMAs are used as actuators to activate the torsional tensegrity mechanism, therefore, the shape memory effect (SME) is discussed in further details. Figures 6.1, the phase diagram, and 6.2, the loading-unloading transformation loop, can be used to further explain the underlying physical phenomenon of SME. Consider the loading steps 1-4, labeled on both figures. In step 1, the SMA wire is pre-stressed and starts in the martensite phase. If the wire is heated past the $A_s$ boundary, the austenite start transformation temperature, transformation from martensite to austenite begins. At step 2, once the temperature reach the $A_f$ boundary, the austenite finish transformation temperature, the material is fully transformed into the austenite phase and large strains (up to 6%) is recovered. The amount of strain recovered during this process is called "transformation strain" or "actuation strain" [24]. Such recovery is caused by the crystallographic differences between austenite and martensite. This completes the loading cycle. To begin the unloading cycle, the material needs to be heated to the $M_s$ boundary, the martensite start transformation temperature, which is point 3. As temperature increases toward point 4, the martensite finish transformation temperature $M_f$ boundary, the material transforms back to martensite crystalline structure and the strain returns.

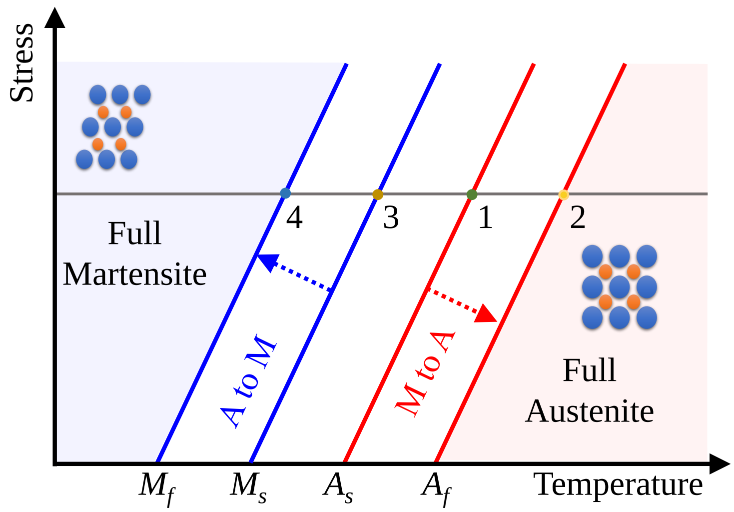


Figure 6.1: Phase diagram schematic highlighting isobaric SME loading path. The corresponding transformation path is shown in Fig. 6.2.

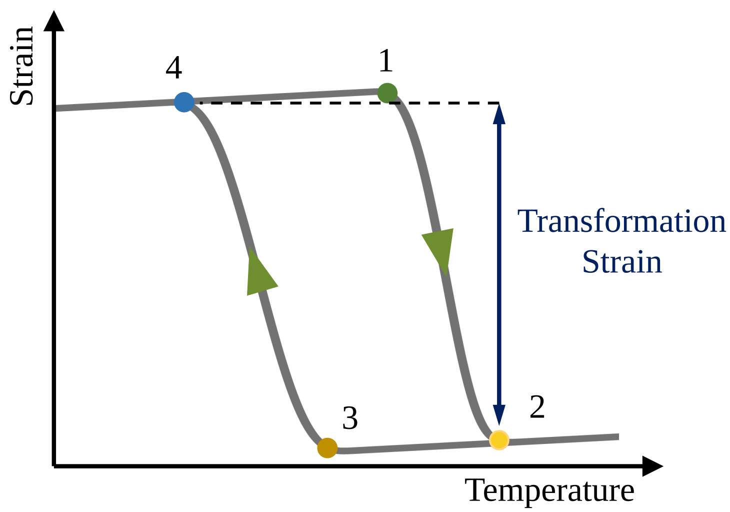


Figure 6.2: SME transformation loop under isobaric condition. The corresponding phase diagram is shown in Fig. 6.1.

## 6.2 SMA-enabled Tensegrity Wing Prototype

This study encompasses experimental testing to assess the twisting capability of the proposed wing design. A preliminary prototype of a tensegrity twisting wing was fabricated by undergraduate students from the Mechanical and Aerospace Engineering Department at the University of California, Irvine. The wing prototype includes wooden ribs trimmed to the shape of the Falcon airfoil using laser cutting technique. The central spar utilizes an aluminum rod that extends spanwise through each rib. Composed of aluminum wires, the stabilizer and longitudinal wires are bounded by plastic stabilizer rings. The preliminary wing prototype demonstrates twisting motion through manual modulation of actuator wire tension.

In this work, SMA wires are integrated into the wing prototype to enable twisting capabilities through SMA actuation. The SAES Getters SmartFlex®, 0.3 mm thick, trained SMA wire actuator is used. Joule heating is achieved using an external 6V electric battery as shown with the setup in Fig. 6.3(a). Each battery terminal is connected to the SMA wire at the wing root and the wing tip, respectively, through a pair of electrical wire clamps. Upon the establishment of the connection to complete a closed circuit, an electrical current is sent through the SMA wire to increase the SMA temperature. The heating induces contraction in the SMA wire length due to the reverse transformation into the martensite phase from its initial austenite phase. Figure 6.3(b) shows the wing twisting motion enabled by SMA wire actuation in the initial, partially twisted, and fully twisted configurations from top to bottom, respectively. Observations from the testing also exhibit quiet, spark-free, and debris-less actuation. After reaching the fully twisted configuration, the electrical connection between the SMA wire and the battery is removed. A combination of natural and forced convection is employed to cool the SMA wire to the ambient temperature. The SMA wire stretches as it undergoes forward transformation to return to the martensite phase during the cooling process. The tensegrity column returns to its initial untwisted configuration after the SMA wire attains its original length at the ambient temperature. The SMA wire actuation cycle is subsequently repeated for multiple iterations, in which the testing demonstrates consistency in the twisting capabilities of the wing design.

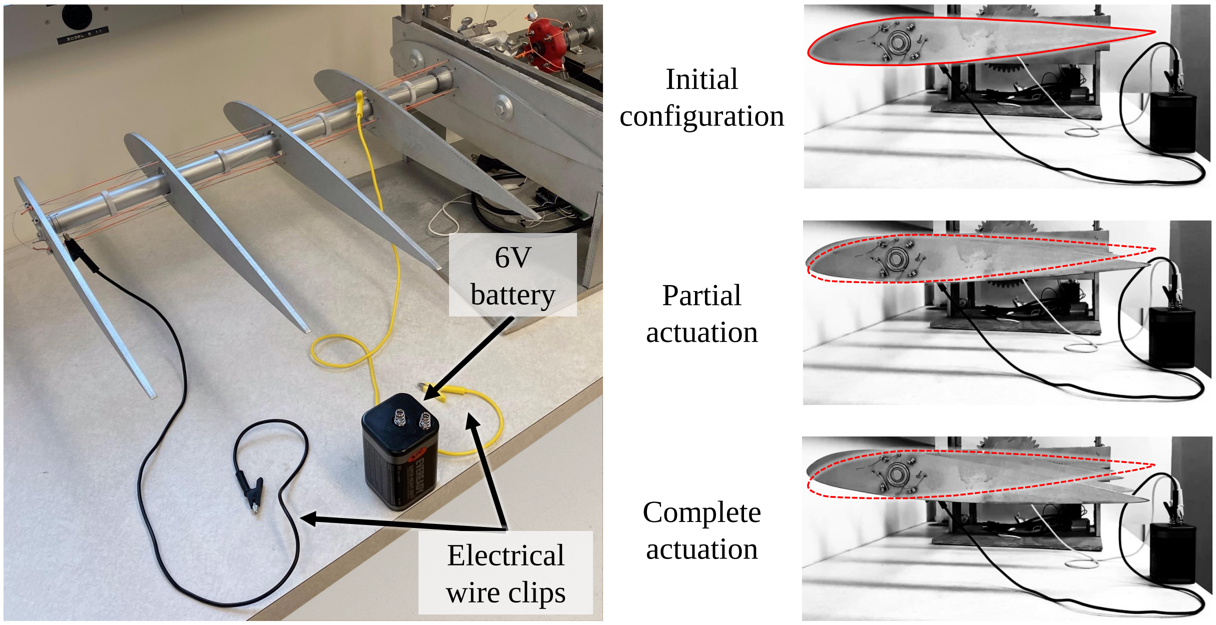


(a) Tabletop tensegrity wing prototype.

(b) Three configurations of wing prototype during twisting.

Figure 6.3: Tensegrity wing prototype. (a) Tabletop tensegrity wing prototype. The SMA wires within the tensegrity mechanism are actuated by connecting them to a 6V battery using electrical wire clips. (b) Three configurations of wing prototype during twisting enabled by connecting the SMA actuator wires to the battery. Reprinted from [22].

## 6.3 SMA Actuation Design of Experiment

A design-of-experiment is devised to evaluate the effectiveness of using SMAs as the actuating mechanism and determine the critical design drivers. In this design exercise, the actuator wires, shown in Fig. 3.6(b), are made from $Ni_{51}Ti_{49}$ shape memory alloys. A MATLAB™ algorithm is used in conjunction with Abaqus CAE to create the FEA model and calculate the structural response to aerodynamic loads and SMA activation. The properties of the $Ni_{51}Ti_{49}$ SMA, laid out in Table 6.1, are referenced from works conducted by Machairas *et al.* and Karakalas *et al.* [31, 34]. The phase diagram associated with the material properties in Table. 6.1 is shown in Fig. 6.4. To facilitate the torsional tensegrity mechanism via actuation of the shape memory actuator wires, a temperature increase of 135 K, starting from 238 K, is implemented.

| **Property** | **Value [unit]** | **Property** | **Value [unit]** |
|---|---|---|---|
| Density | 6500 [kg m$^{-3}$] | Strength | 880 [MPa] |
| Martensite finish transformation temperature ($M_f$) | 283 [K] | Martensite start transformation temperature ($M_s$) | 311 [K] |
| Austenite start transformation temperature ($A_s$) | 313 [K] | Austensite finish transformation temperature ($A_f$) | 336 [K] |
| Thermal expansion coefficient of martensite | -2.61 10$^{-5}$ [K$^{-1}$] | Thermal expansion coefficient of austenite | -3.02 10$^{-5}$ [K$^{-1}$] |
| Stress influence coefficient for martensite | 8.34 [MPa K$^{-1}$] | Stress influence coefficient for austenite | 9.02 [MPa K$^{-1}$] |
| Elastic modulus of martensite | 25.6 [GPa] | Elastic modulus of austenite | 66.20 [GPa] |
| Thermal conductivity of both phases | 18 [W K$^{-1}$ m$^{-1}$] | Specific heat capacity of both phases | 470 [J K$^{-1}$ kg$^{-1}$] |
| Maximum transformation strain | 0.048 | Poisson's ratio | 0.33 |
| Smooth hardening coefficients | 0.0924, 0.0736, 0.1118, 0.0756 | Back stress | 82.05 [MPa] |
| Transformation strain parameter | 1.29 10$^{-8}$ [Pa$^{-1}$] | | |

Table 6.1: SMA material parameters. Obtained from Ref. [31].

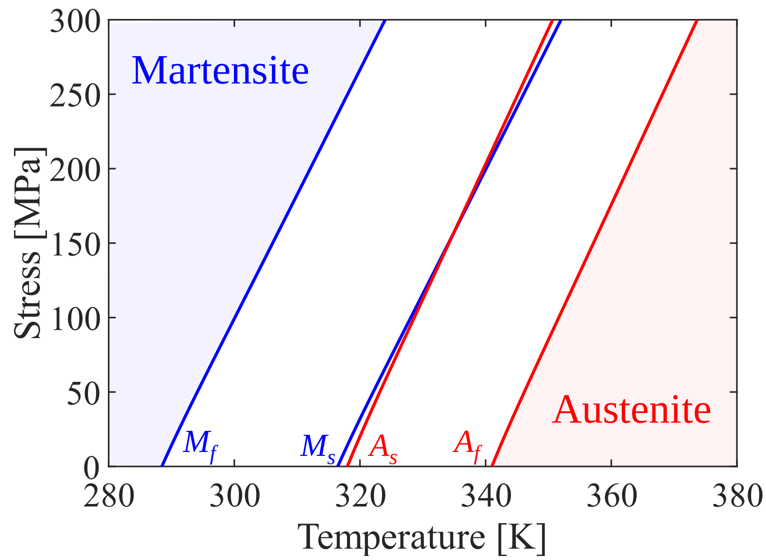


Figure 6.4: Phase diagram schematic highlighting isobaric SME loading path. Adapted from [22].

The `MATLAB` script varies design parameters such as the number of cells $n_c$ and wire sets $n_w$, the thickness of the skin $t_s$ and ribs $t_r$, and spar radius $r_s$. Each of these variables has five initial options, giving a total of 3125 possible design iterations. Since testing and evaluating every possible design iterations is unrealistic, the Taguchi method is employed once again to generate an initial representative design space that can be evaluated to reduce the computation time. Based on the algorithm outlined by Leung and Wang, a 25×5 Taguchi orthogonal array is created [72]. Table 6.2 lists the studied design variables and their respective design values. Based on results of Chapter 5, the values for $n_c$ and $n_w$ were selected. The skin thickness, the spar radius and the thickness of the ribs are assumed values based on trends previously presented.

| **Parameter** | **Studied values** | | | | |
|---|---|---|---|---|---|
| Taguchi array value | (1) | (2) | (3) | (4) | (5) |
| Number of cells ($n_c$) | 4 | 5 | 6 | 7 | 8 |
| Number of wire sets ($n_w$) | 3 | 4 | 5 | 6 | 7 |
| Skin thickness ($t_s$) [mm] | 1.00 | 1.25 | 1.50 | 1.75 | 2.00 |
| Spar radius ($r_s$) [mm] | 4.00 | 4.50 | 5.00 | 5.50 | 6.00 |
| Rib thickness ($t_r$) [mm] | 4.00 | 5.00 | 6.00 | 7.00 | 8.00 |

Table 6.2: Design parameters and their studied values used in SMA actuation DOE.

Other critical design variables such as the wire diameters, wing span, and chord length were fixed in this study. While the wire diameters design values were selected based on the results of Section 5.3. The design values of the mentioned variables are summarized in Table 6.3.

| **Parameter** | **Values** |
|---|---|
| Chord length | 25.3 [cm] |
| Wing half span | 71.1 [cm] |
| Diameter of actuator wires | 3.25 [mm] |
| Diameter of passive wires (longitudinal and stabilizer wires) | 0.81 [mm] |
| Axial length of the rings ($l_r$) | 10.0 [cm] |

Table 6.3: Fixed design parameters and their values used in SMA actuation DOE.

Not counting the SMA actuator wires, the wing structure is composed of three major categories, separated based on their functional properties. The ribs, spar, and stabilizer rings, which are assumed to be made up of Al 7075-T73 alloy, make up one group. Although in the results presented in Section 5.3, Ti-6Al-4V demonstrated superior performance, Al 7075-T73, the runner up and a commonly used aerospace alloy, is chosen for this study due to its lightweight, manufactureability, and economic benefits. The second category of material is the external skin which requires both flexibility and sturdiness. Engineered polymers are the preferred choice for this component category since they offer both morphing capability and stiffness to sustain aerodynamic loads and debris. Sabic 2004-CX3 low-density polyethylene (LDPE) is deemed as a suitable candidate. Finally, the passive wires are grouped into one category and are assumed to be made from the same material. Since these members are the primary load-bearing members of the tensegrity structure they need to be made from a metallic alloy. Gr. 5 Ti alloy is considered in this experiment based on their proven performance as shown in Chapter 5. Table 6.4 list the material types involved in this design study.

| **Component** | **Material** | **Elastic modulus [GPa]** | **Poisson's ratio** | **Strength [MPa]** | **Mass density [kg/m$^3$]** |
|---|---|---|---|---|---|
| Ribs, spar, and rings | Al 7075-T73 | 72.0 | 0.33 | 435.0 | 2810.0 |
| Skin | 2004CX3 LDPE | 0.240 | 0.46 | 10.0 | 921.0 |
| Passive wires | Gr. 5 Ti | 113.8 | 0.34 | 880.0 | 4430.0 |

Table 6.4: Properties of materials used in SMA actuation DOE.

The most favorable design from this DOE based on Eq. (4.2), which exhibited the highest value of $\eta$ corresponding to 7.85°/kg, displayed a maximum twist angle ($\Phi$) of 15.85° and a mass ($m_s$) of 2.02 kg without having any components reach their respective failure values. This design iteration ranked highest in both categories of $\Phi$ and $\eta$, and thus, was deemed as the most favorable. Figures 6.5 - 6.9 are the main effects plots of the five design parameters with the mean values of $\Phi$ and $m_s$ included for reference. The most favorable design choice, chosen based on the criterion set forth in Eq. (4.2) is also identified on each plot with a red rhombus.

The main effects plots that consider the topological parameters $n_c$ and $n_w$, which are the number of cells and wire sets respectively, are correspondingly displayed in Figs. 6.5 and 6.6. The structural mass main effects plots clearly indicated a proportional relationship between these two variables and the structural mass. For $n_c$, the twist angle plot also indicated a directly favorable relationship. On the other hand, an inverted V-shape pattern is observed for the twist angle plot of $n_w$ and the four wire sets design delivered the most favorable outcome.

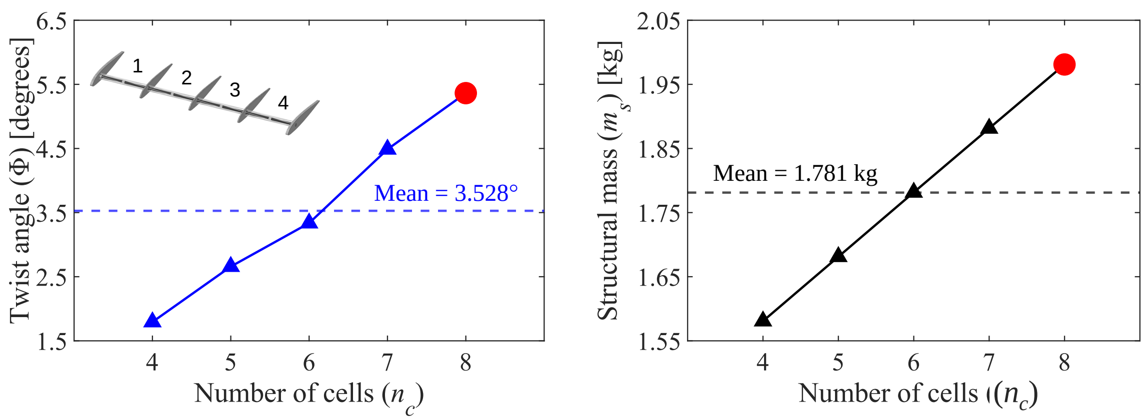


Figure 6.5: Main effect plots of twist angle and mass in terms of number of cells ($n_c$). The red circle indicates the level that provides the highest twist angle per unit mass ($\eta$). Results of SMA DOE. Adapted from [22].

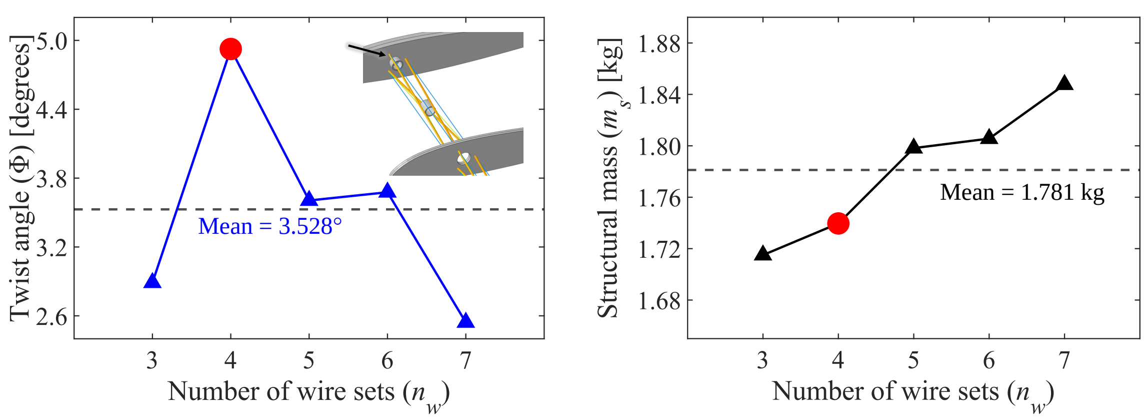


Figure 6.6: Main effect plots of twist angle and mass in terms of number of wires ($n_w$). The red circle indicates the level that provides the highest twist angle per unit mass ($\eta$). Results of SMA DOE. Adapted from [22].

Figures 6.7 - 6.9, in respective order, are main effects plots resulting from varying the three variables: skin thickness ($t_s$), the spar radius ($r_s$), and rib thickness ($t_r$). The structural mass plots in Figs. 6.8 and 6.9 show a direct proportion between these design parameters and structural mass $m_s$. Alternatively, a parabolic response was displayed in Fig. 6.7. The main effects plot associated with the influence of the spar radius illustrated a favorable relation between $r_s$ and $\Phi$, which indicates that a thicker spar will provide a larger twist angle. This result is in agreement with earlier studies [48]. The main effects plot associated with the influence of skin thickness on the twist angle shows an negative relation between $t_s$ and $\Phi$. The 1.00 mm skin delivered the highest value of $\Phi$ and $\eta$. In regards to the rib thickness ($t_r$), the twist angle plot was inconclusive and requires further study as it featured an inverted V-shape. The designs with 7.00 mm thick ribs delivered the highest amount of twist angle on average. It is reasonable to speculate that the number of cells ($n_c$), spar radius ($r_s$), and skin thickness ($t_s$) are the dominant design variables since varying them has a much larger impact on the wing performance. Lastly, in more refined models, clearer trends can be determined as the number of studied design variables decreases and bigger sample sizes are analyzed.

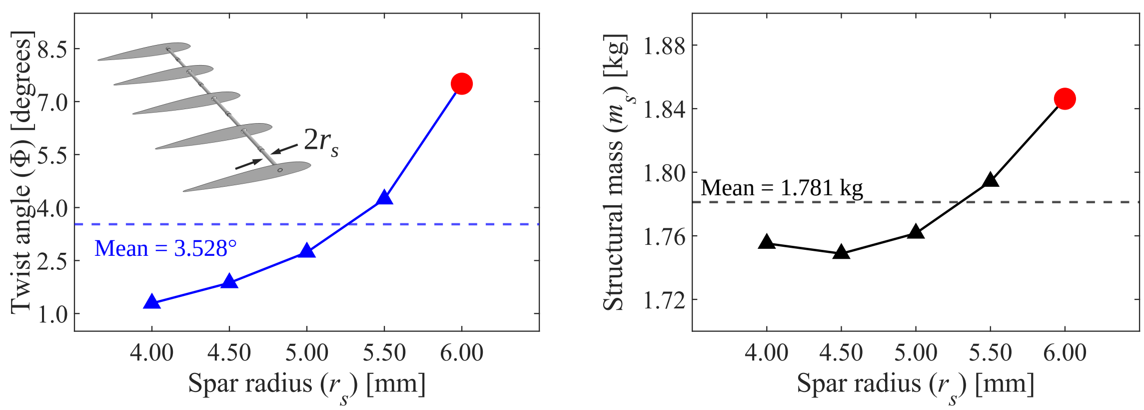


Figure 6.7: Main effects plots of twist angle and mass in terms of spar radius ($r_s$). The red circle indicates the level that provides the highest twist angle per unit mass ($\eta$). Results of SMA DOE. Adapted from [22].

Figure 6.10 are displacement contours of the most favorable design at the initial configuration, 50% deformation, and 100% deformation configurations. The martensite volume fraction variation is provided in Fig. 6.11 for the entire heating-cooling cycle. Table 6.5 summarizes the design parameters and characteristics of this design configuration.

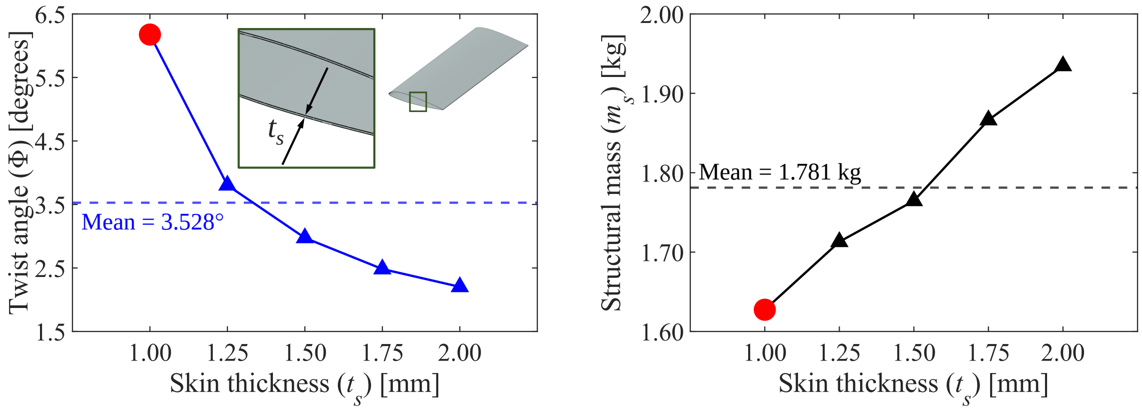


Figure 6.8: Main effects plots of twist angle and mass in terms of skin thickness ($t_s$). The red circle indicates the level that provides the highest twist angle per unit mass ($\eta$). Results of SMA DOE. Adapted from [22].

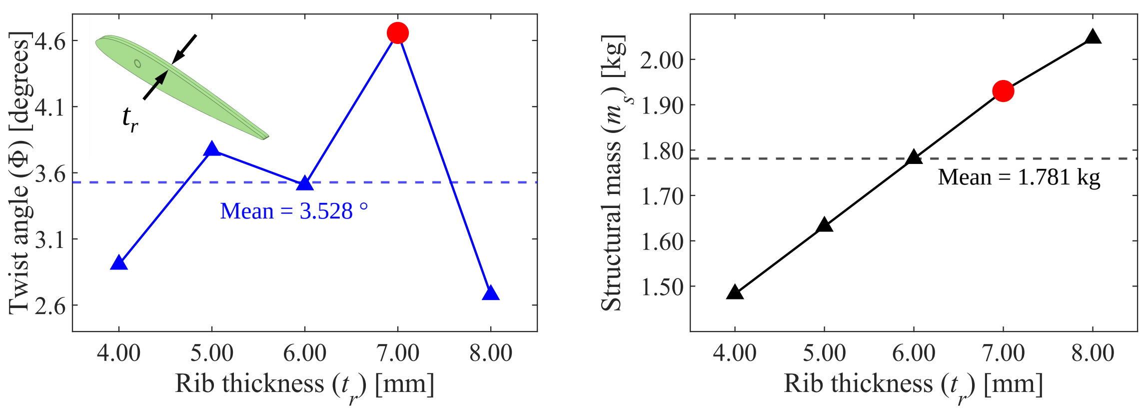


Figure 6.9: Main effects plots of twist angle and mass in terms of rib thickness ($t_r$). The red circle indicates the level that provides the highest twist angle per unit mass ($\eta$). Results of SMA DOE. Adapted from [22].

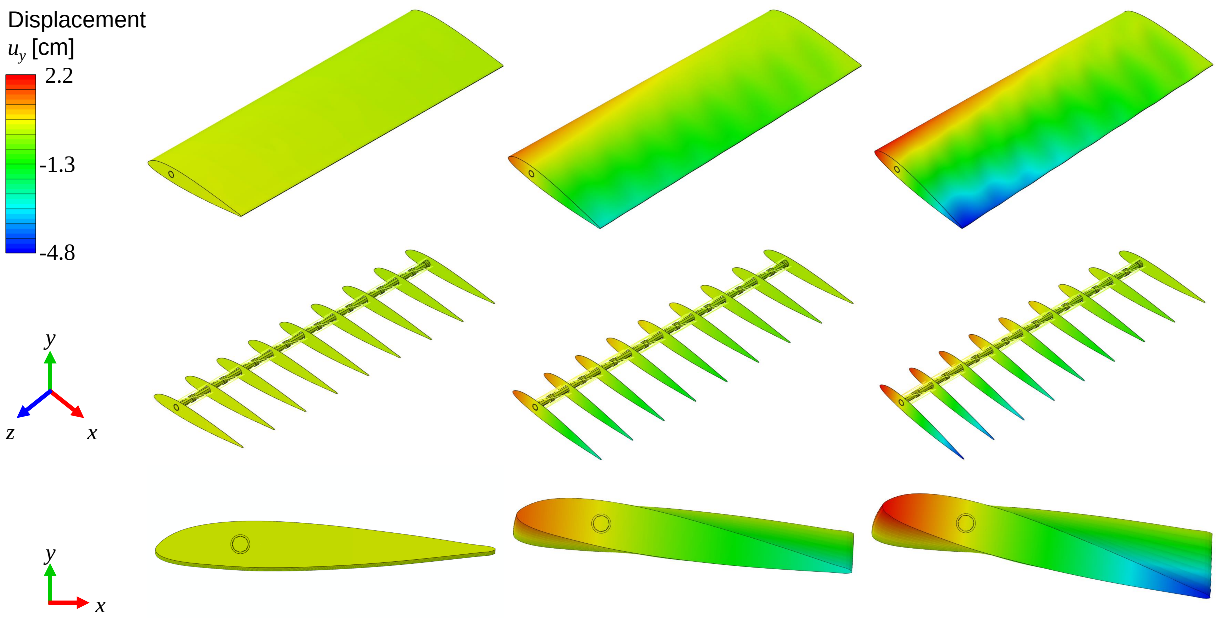


Figure 6.10: Deformation contours of the most favorable design of the SMA DOE according to the criterion defined in Eq. (4.2) at different configurations during twisting. The parameters of this design are listed in Table. 6.5. Results of SMA DOE. Adapted from [22].

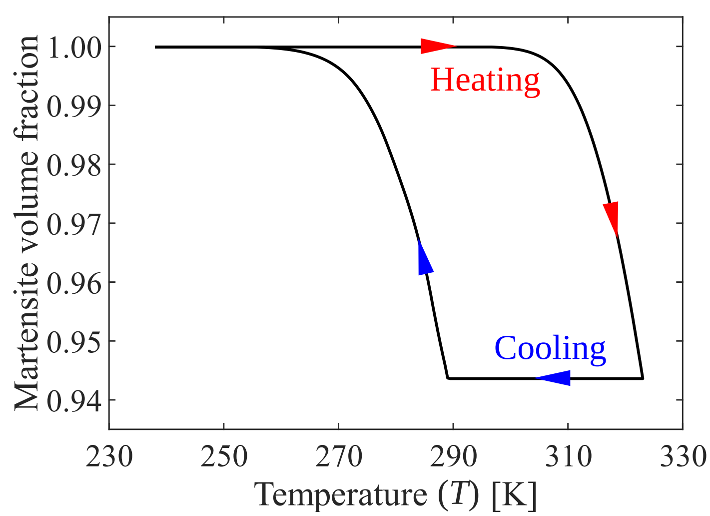


Figure 6.11: Martensite volume fraction variation against temperature change during activation and inactivation cycle. Results of SMA DOE. Adapted from [22].

The results from this chapter suggests that SMAs are suitable candidates to produce the actuator wires. One area of concern for SMAs actuator is their response time to actuation signal. In a highly demanding scenario like during flight, delays in response to control signal can be catastrophic. However, on going and promising research are being conducted to

| **Parameter** | **Value [unit]** |
|---|---|
| Number of cells ($n_c$) | 8 |
| Number of wire sets ($n_w$) | 4 |
| Skin thickness ($t_s$) | 1.00 [mm] |
| Spar radius ($r_s$) | 6.00 [mm] |
| Thickness of ribs ($t_r$) | 7.00 [mm] |
| Diameter of actuator wires ($d_{act}$) | 3.251 [mm] |
| Diameter of passive wires (longitudinal and stabilizer wires) ($d_{pass}$) | 0.813 [mm] |
| Material for ribs, spar, and rings | Al 7075-T73 |
| Material for skin | 2004CX3 LDPE |
| Material for passive wires | Gr. 5 Ti |
| Total twist angle ($\Phi$) | 15.85° |
| Structural mass ($m_s$) | 2.02 [kg] |
| Twist angle per unit mass ($\eta$) | 7.86 [°/kg] |

Table 6.5: Parameters of the most favorable design of SMA DOE.

resolve this concern for SMAs actuators. In Ref. [57], multiple heating and cooling schemes are presented, out of which, resistive heating and forced convective cooling appears to be the ideal options for wing twist actuation. In other works, various heating and cooling schemes are proposed to obtain high speed SMA actuation. In Ref. [51], the researchers varied parameters such as capacitance and voltage to obtained actuation response time as low as 4.61 ms. Likewise, Motzki *et al.* presented a heating scheme with short pulses and high voltage that delivered response times in the range of 40 ms [42]. Typically, the cooling time of SMAs is much higher than that of the heating time and therefore, can cause significant delay in returning the twisted wing to its original configuration. This issue was tackled in Ref. [27], where the authors utilised the critical radius associated with concentric layers of thermal material and highly conductive material to reduce cooling time and thus, improve the practicality of SMA actuators.

# Chapter 7

# Conclusions and Suggested Future Work

## 7.1 Conclusions

[1] [2] This thesis presented a design and modeling study on a novel twisting wing enabled by an internal tensegrity mechanism that exerts torsional deformation. The torsional tensegrity mechanism was able to twist the entire wing from root to tip, thereby modulating the local angle of attack of the wing throughout its span. This modulation in the distribution of spanwise angle of attack enabled the change in the aerodynamic characteristics of the wing, which can be used in implementation to control the lift, drag, and roll of an aircraft.

[1] Portions of this section are reprinted or adapted from [Nguyen K. Pham and Edwin A. Peraza Hernandez, 2021, "Modeling and design exploration of a tensegrity-based twisting wing," Journal of Mechanisms and Robotics. https://doi.org/10.1115/1.4050149]. Figures and texts are reprinted by permission of the American Society of Mechanical Engineers.

[2] Portions of this section are reprinted or adapted from [Nguyen K. Pham and Edwin A. Peraza Hernandez, 2021, "Modeling and design exploration of a morphing wing enabled by a twisting tensegrity mechanism," Proceedings of the 2021 AIAA SciTech Forum and Exposition, AIAA 2021-0099, virtual conference. https://doi.org/10.2514/6.2021-0099]. Figures are reprinted by permission of the American Institute of Aeronautics and Astronautics, Inc.

Unlike conventional wings that employ attached control surfaces such as ailerons and flaps to alter their aerodynamic characteristics, the twisting wing can exhibit changes in such characteristics while having a continuous outer skin. Computational fluid dynamics analyses demonstrated that the twisting wing exhibits higher aerodynamic efficiency, as quantified by a larger lift-to-drag ratio, than an equivalent conventional wing having a control surface.

The internal structure of the wing was subsequently described and parameterized. It consisted of a network of wires connected to the ribs of the wing forming a cylindrical tensegrity column along the wingspan, and a central spar that provided bending stiffness to the wing. To evaluate the structural deformation, mass, and stress responses, a parametric finite element model of the wing, one that allowed for a number of different design variables to be inputted, was developed. The model had a halfspan of 71.12 cm and a chord length of 25.31 cm which came from a reference vehicle, the Carl Goldberg Falcon 56 Mk II R/C UAV.

Subsequently, a DOE study quantifying the influence of the topological parameters of the torsional tensegrity mechanism on the achievable twist angle ($\Phi$), structural mass ($m_S$), and stress in the different components of the wing was performed. The maximum attainable twist angle from root to tip per unit mass for a wing with these dimensions, without any location of the wing exceeding their allowable stress, was 5.93°/kg. The torsional tensegrity mechanism for this design was composed of eight cylindrical cells and four sets of actuator wires along the circumferential perimeter of each cell. Overall, designs with large number of cells and small number of wire sets exhibited higher twist angles per unit mass. The work conducted in this first part of the research and the obtained results have delivered valuable insights into the impacts of topological parameters (number of wire sets $n_w$ and number of cells $n_c$) on the overall performance of the wing.

Followed by the study on the topological design parameters, a case study was conducted to evaluate how different cell span distribution can have an impact on the overall performance. Seven different cell span distribution designs were tested and the twist angles delivered are all within 1% difference. Although, varying the cell span had little impact to the overall performance of the wing, it was concluded that an evenly distributed tensegrity wing with identical cell spans delivered the most optimal performance in terms of twisting angle.

Subsequently, a more in-depth DOE using the Taguchi method was conducted to quantify the influence of varying the design parameters to the torsional tensegrity mechanism. The dependent variables of interest remain the same. Out of the 125 different design iterations and configurations, one design delivered an impressive 19.5°of twist angle while meeting all of the material stress constraints. The geometric characteristics of this design can be found in Table 5.5. The data obtained also offer insights into the primary design drivers and allow for future studies to be more focused on optimization. Particularly, the main effect plots from this DOE confirmed the impact of increasing the number of cells ($n_c$). Furthermore, they also showed an increase in the actuator wire diameter correlates with an increase in the maximum obtainable twist angle.

The final DOE in this research was performed to evaluate the performance of shape memory alloys (SMA) as a means to actuate wing twist and analyze the effects of altering the topological and geometrical design parameters of the wing. The most favorable design studied in the DOE provided a substantial 15.85° total twist angle without any material failure and had a mass of 2.02 kg, its design parameters are shown in Table 6.5 alongside other parameters for this design. The main effect plots obtained from this study clarified some performance trends that were not as apparent in the previous DOE. Specifically, the impacts of varying the skin thickness ($t_s$) and the spar radius ($r_s$) were clearly shown. From these main effect plots, it was observed that an increase in $r_s$ directly translates to a increase in the twist angle ($\Phi$). Alternatively, an increase in $t_s$ led to a decrease in $\Phi$.

Concurrent to the FEA analysis, the wing torsional deformation triggered by SMA wire actuation was demonstrated through a fabricated tensegrity wing prototype equipped with commercially obtained SMA wire actuators. SMA wires were integrated into the tensegrity mechanism to rotate the ribs coaxially to the central spar through actuation (contraction) induced by Joule heating. The obtained twist angle was comparable to the twist angle observed from the FEA model. Accordingly, both experimental and computational analyses demonstrated the twisting capabilities of the SMA-enabled tensegrity wing. The design study results provided understanding towards the influence of each design parameter to facilitate design optimization in future work.

## 7.2 Suggested Future Work

The approach required to allow contraction in the actuator wires of the tensegrity mechanism needs to be further addressed in future studies. Two possible options include using actuator wires composed of smart materials such as shape memory alloys or using motors that contract the actuator wires by pulling them. Although thermally actuated shape memory alloys (SMAs) are potential actuation methods and their application in tensegrity structure has been demonstrated in this research as well as in other settings [8, 15, 35, 55] , their slow time response to a control signal, due to the time required to heat and cool the wires, poses an obstacle in aeronautical applications. Future work need to entail the characterization and feasibility studies of the actuation speed of the SMA actuators and the investigation of heating and cooling schemes that may enable sufficiently fast thermal actuation cycles.

The next phase of this research is to perform optimization to deliver a functional morphing wing that maximizes the twist-angle-to-mass ratio. As research in this topic moves forward, it is critical that an optimized tensegrity-based twisting wing prototype is fabricated and tested to validate and demonstrate the motion of the torsional mechanism and the structural integrity of the wing during twisting. Additionally, wind tunnel and in flight testing should be performed to confirm the computational fluid dynamics results and fully comprehend the lift-controlling effects that a twisting wing can exhibit along with other aerodynamic characteristics such as drag-reduction and roll-control. Lastly, a more in-depth comparative study needs to be conducted between the tensegrity twisting wing design and the conventional wing to account for every aspect of performance such as aerodynamic efficiency, structure weight, and power requirement.

# Bibliography


[1] Airfoil Tools. Falcon - Falcon airfoil used on the Carl Goldberg Falcon 56 Mk II R/C powerplane, 2020. Data retrieved from website of Airfoil Tools, `http://airfoiltools.com/airfoil/details?airfoil=falcon-il`. Last Accessed 09/27/2020.

[2] ASM Aerospace Specification Metals, Inc. Titanium Ti-6Al-4V (Grade 5), annealed, 2020. Data retrieved from the MatWeb website, `http://asm.matweb.com/search/SpecificMaterial.asp?bassnum=MTP641`. Last Accessed: 09/27/2020.

[3] D. D. Baldwin and E. A. Peraza Hernandez. Design of tensegrity-based lattices with engineered load-bearing and thermal expansion properties. In *ASME 2020 International Design Engineering Technical Conferences and Computers and Information in Engineering Conference*, pages DETC2020–22705, V010T10A074, 08 2020.

[4] A. Beyene and J. Peffley. A morphing blade for wave and wind energy conversion. In *OCEANS 2007-Europe*, pages 1–6. IEEE, 2007.

[5] B. R. Bielefeldt, D. J. Hartl, J. D. Hodson, G. W. Reich, P. S. Beran, A. M. Pankonien, and J. D. Deaton. Graph-based interpretation of L-system encodings toward aeroelastic topology optimization of a morphing airfoil in supersonic flow. In *Smart Materials, Adaptive Structures and Intelligent Systems*, volume 59131, page V001T04A013, 2019.

[6] Q. Boehler, I. Charpentier, M. S. Vedrines, and P. Renaud. Definition and computation of tensegrity mechanism workspace. *Journal of Mechanisms and Robotics*, 7(4):044502, 2015.

[7] R. J. Boulbes. *Troubleshooting Finite-Element Modeling with Abaqus*. Springer, 2020.

[8] G. M. Butler and E. A. Peraza Hernandez. Tensegrity structures incorporating actuator and pseudoelastic shape memory alloys. In *International Mechanical Engineering Congress and Exposition*, pages IMECE2020–24645. American Society of Mechanical Engineers, 2020.

[9] F. T. Calkins and J. H. Mabe. Flight test of a shape memory alloy actuated adaptive trailing edge flap. In *Smart Materials, Adaptive Structures and Intelligent Systems*, volume 50480, page V001T04A007, 2014.

[10] C. Cesnik and E. Brown. Modeling of high aspect ratio active flexible wings for roll control. In *43rd AIAA/ASME/ASCE/AHS/ASC Structures, Structural Dynamics, and Materials Conference*, page 1719, 2002.

[11] Y. S. Chung, J.-H. Lee, J. H. Jang, H. R. Choi, and H. Rodrigue. Jumping tensegrity robot based on torsionally prestrained SMA springs. *ACS Applied Materials & Interfaces*, 11(43):40793–40799, 2019.

[12] Covestro. Desmopan copolymers: Flexible, durable and versatile, 2020. Data retrieved from website of Covestro, `https://www.solutions.covestro.com/en/brands/desmopan`. Last Accessed: 09/27/2020.

[13] M. C. de Oliveira, R. E. Skelton, and W. Chan. Minimum mass design of tensegrity towers and plates. In *Proceedings of the 45th IEEE Conference on Decision and Control*, pages 2314–2319. IEEE, 2006.

[14] Y. Dong, Z. Boming, and L. Jun. A changeable aerofoil actuated by shape memory alloy springs. *Materials Science and Engineering: A*, 485(1):243–250, 2008.

[15] F. A. dos Santos, A. Rodrigues, and A. Micheletti. Design and experimental testing of an adaptive shape-morphing tensegrity structure, with frequency self-tuning capabilities, using shape-memory alloys. *Smart Materials and Structures*, 24(10):105008, 2015.

[16] A. Emiliavaca, C. J. de Araújo, C. R. Souto, and A. Ries. Characterization of shape memory alloy micro-springs for application in morphing wings. *Smart Materials and Structures*, 28(1):015010, nov 2018.

[17] M. Furet and P. Wenger. Kinetostatic analysis and actuation strategy of a planar tensegrity 2-X manipulator. *Journal of Mechanisms and Robotics*, 11(6):060904, 2019.

[18] O. S. Gabor, A. Koreanschi, and R. M. Botez. Low-speed aerodynamic characteristics improvement of ATR 42 airfoil using a morphing wing approach. In *IECON 2012 - 38th Annual Conference on IEEE Industrial Electronics Society*, pages 5451–5456, 2012.

[19] R. Goyal, E. A. Peraza Hernandez, and R. E. Skelton. Analytical study of tensegrity lattices for mass-efficient mechanical energy absorption. *International Journal of Space Structures*, 34(1-2):3–21, 2019.

[20] R. Goyal, R. E. Skelton, and E. A. Peraza Hernandez. Design of minimal mass load-bearing tensegrity lattices. *Mechanics Research Communications*, 103:103477, 2020.

[21] R. Goyal, R. E. Skelton, and E. A. Peraza Hernandez. Efficient design of lightweight reinforced tensegrities under local and global failure constraints. *Journal of Applied Mechanics*, 87(11):111005, 2020.

[22] W. Guan, N. K. Pham, and E. A. Peraza Hernandez. Design exploration of a tensegrity twisting wing enabled by shape memory alloy wire actuation. In *SPIE Smart Structures + Nondestructive Evaluation 2021 Digital Forum*, 2021.

[23] D. J. Hartl and D. C. Lagoudas. Aerospace applications of shape memory alloys. *Proceedings of the Institution of Mechanical Engineers, Part G: Journal of Aerospace Engineering*, 221(4):535–552, 2007.

[24] D. J. Hartl and D. C. Lagoudas. Aerospace applications of shape memory alloys. *Proceedings of the Institution of Mechanical Engineers, Part G: Journal of Aerospace Engineering*, 221(4):535–552, 2007.

[25] J. V. Henrickson, R. E. Skelton, and J. Valasek. Shape control of tensegrity airfoils. In *AIAA Guidance, Navigation, and Control Conference*, page 1864, 2016.

[26] J. D. Hodson, A. P. Christopherson, J. D. Deaton, A. M. Pankonien, G. W. Reich, and P. S. Beran. Aeroelastic topology optimization of a morphing airfoil in supersonic flow using evolutionary design. In *AIAA Scitech 2019 Forum*, page 1466, 2019.

[27] S. Huang, M. Leary, T. Ataalla, K. Probst, and A. Subic. Optimisation of ni–ti shape memory alloy response time by transient heat transfer analysis. *Materials & Design*, 35:655–663, 2012.

[28] B. Jenett, S. Calisch, D. Cellucci, N. Cramer, N. Gershenfeld, S. Swei, and K. C. Cheung. Digital morphing wing: active wing shaping concept using composite lattice-based cellular structures. *Soft Robotics*, 4(1):33–48, 2017.

[29] J. J. Joo, G. W. Reich, and J. T. Westfall. Flexible skin development for morphing aircraft applications via topology optimization. *Journal of Intelligent Material Systems and Structures*, 20(16):1969–1985, 2009.

[30] W.-R. Kang, E. H. Kim, M.-S. Jeong, and I. Lee. Morphing wing mechanism using an SMA wire actuator. *International Journal of Aeronautical and Space Sciences*, 13(1):58–63, 2012.

[31] A. A. Karakalas, T. T. Machairas, A. G. Solomou, and D. A. Saravanos. Modeling of partial transformation cycles of smas with a modified hardening function. *Smart Materials and Structures*, 28(3):035014, 2019.

[32] S. Kota, R. Osborn, G. Ervin, D. Maric, P. Flick, and D. Paul. Mission adaptive compliant wing–design, fabrication and flight test. In *RTO Applied Vehicle Technology Panel (AVT) Symposium*. RTO-MP-AVT-168, Evora, Portugal, 2009.

[33] P. B. Leal, M. A. Savi, and D. J. Hartl. Aero-structural optimization of shape memory alloy-based wing morphing via a class/shape transformation approach. *Proceedings of the Institution of Mechanical Engineers, Part G: Journal of Aerospace Engineering*, 232(15):2745–2759, 2018.

[34] T. T. Machairas, A. G. Solomou, A. A. Karakalas, and D. A. Saravanos. Effect of shape memory alloy actuator geometric non-linearity and thermomechanical coupling on the response of morphing structures. *Journal of Intelligent Material Systems and Structures*, 30(14):2166–2185, 2019.

[35] D. Martins and P. J. P. Gonçalves. On the dynamics of a smart tensegrity structure using shape memory alloy. In *Journal of Physics: Conference Series*, volume 1264, page 012001. IOP Publishing, 2019.

[36] MATWEB Material property data. Aluminum 6061-T6; 6061-T651, 2020. Data retrieved from the MatWeb website, `http://www.matweb.com/search/DataSheet.aspx?MatGUID=b8d536e0b9b54bd7b69e4124d8f1d20a&ckck=1`. Last Accessed: 09/27/2020.

[37] A. S. Mills, D. H. Myszka, D. C. Woods, J. J. Joo, and A. P. Murray. The structural suitability of tensegrity aircraft wings. In *AIAA Scitech 2020 Forum*, page 0480, 2020.

[38] G. Molinari, A. F. Arrieta, and P. Ermanni. Aero-structural optimization of three-dimensional adaptive wings with embedded smart actuators. *AIAA Journal*, 52(9):1940–1951, 2014.

[39] K. Moored and H. Bart-Smith. Investigation of clustered actuation in tensegrity structures. *International Journal of Solids and Structures*, 46(17):3272–3281, 2009.

[40] K. W. Moored and H. Bart-Smith. The analysis of tensegrity structures for the design of a morphing wing. In *ASME 2005 International Mechanical Engineering Congress and Exposition*, pages 81–89, 2005.

[41] N. Morgan. Medical shape memory alloy applications—the market and its products. *Materials Science and Engineering: A*, 378(1-2):16–23, 2004.

[42] P. Motzki, T. Gorges, M. Kappel, M. Schmidt, G. Rizzello, and S. Seelecke. High-speed and high-efficiency shape memory alloy actuation. *Smart Materials and Structures*, 27(7):075047, 2018.

[43] D. H. Myszka and J. J. Joo. A study on the structural suitability of tensegrity structures to serve as morphing aircraft wings. In *ASME 2018 International Design Engineering Technical Conferences and Computers and Information in Engineering Conference*, pages DETC2018–85945, V05BT07A005, 2018.

[44] K. Pajunen, P. Johanns, R. K. Pal, J. J. Rimoli, and C. Daraio. Design and impact response of 3D-printable tensegrity-inspired structures. *Materials & Design*, 182:107966, 2019.

[45] R. Pecora, F. Amoroso, and L. Lecce. Effectiveness of wing twist morphing in roll control. *Journal of Aircraft*, 49(6):1666–1674, 2012.

[46] N. Pham and E. A. Peraza Hernandez. Modeling and design exploration of a tensegrity-based twisting wing. *Journal of Mechanisms and Robotics*, 2021.

[47] N. K. Pham and E. A. Peraza Hernandez. Design exploration of a tensegrity-based twisting wing. In *ASME 2020 International Design Engineering Technical Conferences and Computers and Information in Engineering Conference*, pages DETC2020–22656, V010T10A072. American Society of Mechanical Engineers Digital Collection, 2020.

[48] N. K. Pham and E. A. Peraza Hernandez. Modeling and design exploration of a morphing wing enabled by a twisting tensegrity mechanism. In *AIAA Scitech 2021 Forum*, page 0099, 2021.

[49] W. Phillips, N. Alley, and W. Goodrich. Lifting-line analysis of roll control and variable twist. *Journal of Aircraft*, 41(5):1169–1176, 2004.

[50] W. F. Phillips, S. R. Fugal, and R. E. Spall. Minimizing induced drag with wing twist, computational-fluid-dynamics validation. *Journal of Aircraft*, 43(2):437–444, 2006.

[51] J. Qiu, J. Tani, D. Osanai, and Y. Urushiyama. High-speed actuation of shape memory alloy. In *Smart Structures and Devices*, volume 4235, pages 188–197. International Society for Optics and Photonics, 2001.

[52] J. Rieffel, F. Valero-Cuevas, and H. Lipson. Automated discovery and optimization of large irregular tensegrity structures. *Computers & Structures*, 87(5-6):368–379, 2009.

[53] J. J. Rimoli. On the impact tolerance of tensegrity-based planetary landers. In *57th AIAA/ASCE/AHS/ASC Structures, Structural Dynamics, and Materials Conference*, page 1511, 2016.

[54] H. Rodrigue, S. Cho, M.-W. Han, B. Bhandari, J.-E. Shim, and S.-H. Ahn. Effect of twist morphing wing segment on aerodynamic performance of UAV. *Journal of Mechanical Science and Technology*, 30(1):229–236, 2016.

[55] J. L. Rohmer, E. A. Peraza Hernandez, R. E. Skelton, D. J. Hartl, and D. C. Lagoudas. An experimental and numerical study of shape memory alloy-based tensegrity/origami structures. In *ASME 2015 International Mechanical Engineering Congress and Exposition*, pages IMECE2015–51928, V009T12A064, 2015.

[56] R. Romano and E. A. Tannuri. Modeling, control and experimental validation of a novel actuator based on shape memory alloys. *Mechatronics*, 19(7):1169–1177, 2009.

[57] R. Saunders, D. Hartl, J. Herrington, L. Hodge, and J. Mabe. Optimization of a composite morphing wing with shape memory alloy torsional actuators. In *Smart Materials, Adaptive Structures and Intelligent Systems*, volume 46155, page V002T02A014. American Society of Mechanical Engineers, 2014.

[58] R. N. Saunders, D. J. Hartl, J. G. Boyd, and D. C. Lagoudas. Modeling and development of a twisting wing using inductively heated shape memory alloy actuators. In *Active and Passive Smart Structures and Integrated Systems 2015*, volume 9431, pages 263 – 270. SPIE, 2015.

[59] M. Selig. *Summary of Low Speed Airfoil Data*. Number v. 3 in Summary of Low Speed Airfoil Data. SoarTech Publications, 1997.

[60] R. E. Silverman and E. A. Peraza Hernandez. Designing lightweight tensegrity-based structures and materials of tailorable thermal expansion. In *International Design Engineering Technical Conferences and Computers and Information in Engineering Conference*, volume 59230, page V05AT07A032. American Society of Mechanical Engineers, 2019.

[61] R. Skelton, F. Fraternali, G. Carpentieri, and A. Micheletti. Minimum mass design of tensegrity bridges with parametric architecture and multiscale complexity. *Mechanics Research Communications*, 58:124–132, 2014.

[62] R. E. Skelton and M. C. de Oliveira. *Tensegrity Systems*, volume 1. Springer, 2009.

[63] G. Song, N. Ma, and H.-N. Li. Applications of shape memory alloys in civil structures. *Engineering structures*, 28(9):1266–1274, 2006.

[64] T. Tadaki, K. Otsuka, and K. Shimizu. Shape memory alloys. *Annual Review of Materials Science*, 18(1):25–45, 1988.

[65] Tensegrity Wing Senior Design Students. Tensegrity wing project, 2019. `http://projects.eng.uci.edu/projects/2018-2019/tensegrity-wing`. Last Accessed 09/27/2020.

[66] A. Thomas. *Aircraft Drag Reduction Technology*, pages 6–2. Advisory Group for Aerospace Research and Development, Lockheed-Georgia CO Marietta Flight Sciences Division, 1985.

[67] S. Vasista, L. Tong, and K. Wong. Realization of morphing wings: a multidisciplinary challenge. *Journal of Aircraft*, 49(1):11–28, 2012.

[68] R. Vos, Z. Gürdal, and M. Abdalla. Mechanism for warp-controlled twist of a morphing wing. *Journal of Aircraft*, 47(2):450–457, 2010.

[69] W. Wang, S. Caro, F. Bennis, and O. R. Salinas Mejia. A simplified morphing blade for horizontal axis wind turbines. *Journal of Solar Energy Engineering*, 136(1):011018–1 – 011018–8, 2014.

[70] W. Wang, S. Caro, F. Bennis, R. Soto, and B. Crawford. Multi-objective robust optimization using a postoptimality sensitivity analysis technique: application to a wind turbine design. *Journal of Mechanical Design*, 137(1):011403–1 – 011403–11, 2015.

[71] C. Warsop and W. Crowther. NATO AVT-239 task group: Flight demonstration of fluidic flight controls on the MAGMA subscale demonstrator aircraft. In *AIAA Scitech 2019 Forum*, page 0282, 2019.

[72] Y.-W. Leung and Y. Wang. An orthogonal genetic algorithm with quantization for global numerical optimization. *IEEE Transactions on Evolutionary Computation*, 5(1):41–53, 2001.

[73] Z.-W. Zhu, Z.-B. Gou, J. Xu, and H.-L. Wang. Research on nonlinear dynamic characteristics of semi-active suspension system with sma spring. In *2008 International Conference on Intelligent Computation Technology and Automation (ICICTA)*, volume 1, pages 688–692. IEEE, 2008.

# Appendix A

# List of Symbols

| | |
|---|---|
| $A_f$ | Austenite finish transformation temperature |
| $A_s$ | Austenite start transformation temperature |
| $c$ | Chord length |
| $C_D$ | Drag coefficient |
| $c_l$ | Sectional lift coefficient |
| $C_L$ | Lift coefficient |
| $c_p$ | Pressure coefficient |
| $d_{act}$ | Diameter of actuator wires |
| $d_{pass}$ | Diameter of passive wires (longitudinal and stabilizer wires) |
| $l_r$ | Axial length of the rings |
| $\mathbf{m}_{ij}$ | $i \in \{0, \ldots, n_c - 1\}, j \in \{0, \ldots, n_w - 1\}$; wire end points located at the root side of the rings |
| $m_s$ | Structural mass |
| $M_f$ | Martensite finish transformation temperature |
| $M_s$ | Martensite start transformation temperature |
| $n_c$ | Number of cells |

| | |
|---|---|
| $\mathbf{n}_{ij}$ | $i \in \{0, \ldots, n_c - 1\}, j \in \{0, \ldots, n_w - 1\}$; wire end points located at the tip side of the rings |
| $n_w$ | Number of wire sets |
| $p$ | Air pressure |
| $p_\infty$ | Ambient pressure, assumed to be 101325 Pa |
| $\mathbf{p}_{ij}$ | $i \in \{0, \ldots, n_c - 1\}, j \in \{0, \ldots, n_w - 1\}$; wire end points located at the ribs |
| $q$ | Dynamic pressure, calculated at standard sea level condition |
| $r$ | Middle radius of the rings |
| $R$ | Radial distance between the wire end points and the center of the spar |
| $r_s$ | Spar radius |
| $s$ | Wing span |
| $t_r$ | Rib thickness |
| $t_s$ | Skin thickness |
| $v$ | Air velocity, assumed to be 20 m/s |
| $u_y$ | Displacement along the wing thickness direction |
| $x/c$ | $x$-location of point on the airfoil non-dimensionalized by chord length |
| $y/c$ | $y$-location of point on the airfoil non-dimensionalized by chord length |
| $\alpha$ | Angle of attack |
| $\Gamma$ | Ratio of cell length along the span direction between the tip cell and the root cell |
| $\delta$ | Flap deflection angle |
| $\eta$ | Twist angle per unit mass |
| $\varphi$ | Twist angle of an individual cell |
| $\Phi$ | Total twist angle |
| $\Phi_{ref}$ | Reference total twist angle |
| $\rho$ | Air density, assumed to be 1.225 kg/m$^3$ |
| $\sigma_{VM}$ | von Mises stress |